UXO TARGET DETECTION AND DISCRIMINATION WITH ELECTROMAGNETIC DIFFERENTIAL ILLUMINATION

UX1355 - FINAL REPORT

Lead Principle Investigator: Dr. Jack Foley

Shaw Environmental, Inc.
Sky Research, Inc.

June 2005

Contents

List of Figures

List of Tables

Chapter 1

Introduction

The research described in this report was conducted in support of SERDP SEED Broad Agency Announcement (BAA) dated November 14, 2001, Statement of Need UXSEED-03-01, "Innovative Approaches to Unexploded Ordnance (UXO) Cleanup." A SERDP SEED research and development project UX-1355 entitled "UXO Target Detection and Discrimination with Electromagnetic Differential Illumination" was proposed in response to the above BAA. The intent of the project was to address UXO detection in complex and hostile soil environments such as Kaho'olawe Island, Hawaii and the Waikoloa Manoeuver Area, Hawaii. Geophysical target signatures recorded from electromagnetic induction (EMI) sensors, such as the Geonics EM61, contain extreme levels of background noise caused in large part by magnetically permeable soils. The spatial variation of the soil effects is not separate and distinct from the signatures of buried UXO at a single frequency or time gate. This minimizes the effectiveness of spatial filtering for separating UXO signatures from soil effects. Existing fixed-geometry, transmitter / receiver coincident EMI systems have not produced data sufficient to reliably detect UXO in the presence of strong geologic effects.

At Kaho'olawe Island, the geologic influence on the data led to very poor detection results during controlled tests. Several contractors deployed various EMI sensor technologies and detected only approximately 50% of seeded targets (Cargile et al., 2004a). Compounding this problem is a lack of predictability of the undetected targets in terms of their target size and depth Cespedes et al. (2001). In less hostile environments, undetected UXO typically fall below a line defined by target depth and target size. The recent Kaho'olawe test has shown that large shallow targets are not being selected as potential UXO due to site-specific environmental conditions.

A new strategy of data collection is required to isolate UXO target signatures from geologic effects. A technique to preferentially illuminate the targets relative to the soils is proposed. We take the approach that if the differences between UXO and geologic responses are not sufficiently evident in the EMI data as presently collected, technique needs to be developed whereby differences are induced through altering data collection procedures.

We propose an EMI survey methodology to exploit inherent differences in electromagnetic properties of conductive and permeable metal targets and the superparamagnetic geologic media through differential illumination. The details of this approach are provided below, but the general idea is straightforward: in the presence of large sources of geologic noise, differential measurements are required to isolate UXO. Each survey will acquire data that promise either to reduce the geologic noise or discriminate between geologic noise and local conductors such as UXO. We will develop optimal survey configurations and operation parameters to exploit electromagnetic variations in different material properties associated with UXO and volcanic soils.

The report is structured as follows. In the first section we review and extend a theory that predicts the response of a metal detector to a soil with given electromagnetic properties. We then use that theory to

predict the effect of different changes in transmitter/receiver on the EM response of both soils and metals. This leads us to concentrate on differential measurements that involve changing transmitter waveform characteristics (particularly the charge time). The third section describes the field data collection at Kaho'olawe Island and Waikoloa, Hawaii and includes a preliminary review of the data. The next section considers the impact of micro-topography and sensor height and tilt on the measured EMI response. The last section provides a detailed analysis of the data and a discussion of the feasibility and effectiveness of the differential illumination technique.

The results described in this report have been the subject of three different conference presentations. Much of the material in Chapters 2 and 3 were presented at the European Union in Humanitarian Demining (EUDEM) conference in Brussels by Billings et al. (2003). Chapter 5 formed the basis of the paper by Walker et al. (2005) and Chapter 6 is largely reproduced from Pasion et al. (2005). These last two papers were presented at the Symposium on the Application of Geophysics to Engineering and Environmental Problems (SAGEEP) conference in Atlanta in 2005.

Chapter 2

The effect of soil on a metal detector

2.1 Physical parameters affecting a metal detector

There are three main physical phenomena that occur when a metal detector passes over the ground:

1. *Instantaneous magnetization* which represents an instantaneous alignment of magnetic domains within the ground with the applied field and is a function of susceptibility χ_i, (the i-subscript refers to instantaneous);

2. *Eddy currents* which are set up on the surface when the field changes and gradually diffuse and decay with time. Their strength and speed of propagation depend on the susceptibility and conductivity, σ, of the ground;

3. *Magnetic viscosity* which is caused by a time-delay in the alignment of certain magnetic domains; It is a function of the frequency dependent susceptibility $\chi_v(\omega)$, with the v-subscript referring to viscosity. In this report, we use the terms magnetic viscosity, frequency dependant susceptibility and viscous remanent magnetism (VRM) interchangeably.

2.1.1 Instantaneous magnetization

Instantaneous magnetization represents an effectively instantaneous change in the direction and strength of magnetization on application of an external field, H. This magnetization typically occurs through movement of domain-walls in multi-domain ferrimagnetic grains within the soil. The strength of the instantaneous magnetization, M_i, is related to the susceptibility of the medium, $M_i = \chi_i H$. Now, because the acquisition and loss of the magnetization is instantaneous, the response measured by the metal detector will be in-phase with the primary field. This effect is evident in the in-phase response of the Geophex GEM-3 frequency domain sensor, for instance. In this report, we concentrate on pulse-induction detectors where the measurements are taken during the off-time so that instantaneous magnetization will have no direct effect on the metal detector response.

2.1.2 Eddy currents

When the primary magnetic field changes, eddy currents are set up on the surface to oppose that change. The evolution of the eddy currents will depend on the distribution of conductivity in the soil. However, a good first-order estimate of the eddy current response can be obtained from the transient response of a circular loop (radius a carrying a current I) over a conductive and permeable half-space. This situation has been well studied in the geophysical community by Nabighian (1979). The eddy-current response consists

of two stages. At the earliest times the eddy currents are distributed on the surface of the half-space and the induction coil response is flat. This corresponds to the so called inductive limit. At late time, the current starts to move downwards and spreads out, with the induction coil response at the center of the loop decaying as

$$\frac{\partial H_z}{\partial t} = \frac{I\sigma^{3/2}\mu_o^{3/2}(1+\chi_i)^{3/2}a^2}{20\sqrt{\pi}}\frac{1}{t^{5/2}} \tag{2.1}$$

where μ_o is the permeability of free space. This late time response is referred to as the ground effect. The most significant factor to observe in this equation is the $t^{-5/2}$ decay of the eddy currents at late time.

2.1.3 Magnetic viscosity

Magnetic viscosity occurs in superparamagnetic and single-domain grains of ferrimagnetic material. Applied fields cause a change in the direction of magnetization in a domain once it overcomes an energy barrier, which depends on both the shape (anisotropy) and volume of the domain. According to the Néel theory (Néel, 1949) for non-interacting single-domain grains, the probability of such a transition is approximately equal to the exponential of the ratio of anisotropy energy E to thermal energy kT where k is Boltzmann's constant and T is the temperature. This reversal, or switching time, is referred to as the Néel relaxation time, which Néel estimated to be

$$\tau = \tau_o \exp(\frac{-E}{kT}) \tag{2.2}$$

where $\tau_o \approx 10^{-9}$ is the damping or excitation time.

In a material such as a soil, there are a wide range of domain sizes and shapes, so that there are a wide range of relaxation times. If a magnetic field is suddenly applied or removed from such a material, some grains will rotate almost immediately, others will take longer to do so, and even after a considerable period of time there will still be some changing direction.

Consider the situation where a small DC field, H, has been applied to a system from time $t = -\infty$. As an effectively infinite time has elapsed, all grains exhibiting viscosity will be aligned with the applied field and the viscous magnetization will be $M_v = H\chi_o$, where χ_o is the *equilibrium* susceptibility. If the field is instantly switched off at $t = 0$, the magnetization will decay as

$$M_v(t) = H\chi_o F(t) \tag{2.3}$$

where $F(t)$ is the so-called *after-effect function* with the properties that $F(0) = 1$ and $F(t \to \infty) = 0$. For a system with a single relaxation time, the after-effect function is given by

$$F(t) = \exp(-t/\tau) \tag{2.4}$$

When the relaxation times are distributed with the weight function $f(\tau)$ the after-effect function becomes

$$F(t) = \int_0^\infty f(\tau)\exp(-t/\tau)\mathrm{d}\tau \tag{2.5}$$

Thus, it is evident that the distribution of the relaxation times will be critical in determining the behavior of the system. From Eq. (2.2) we may write that

$$\mathrm{d}E = -kT\mathrm{d}\tau/\tau \tag{2.6}$$

This equation implies that if there is a uniform distribution of energy barriers between finite limits, then the distribution function is

$$f(\tau) = \frac{1}{\tau \log(\tau_2/\tau_1)} \text{ for } \tau_1 \leq \tau \leq \tau_2 \tag{2.7}$$

and zero everywhere else, where τ_1 is the lower and τ_2 is the upper time-constant in the system. The weight function in Eq. 2.7 has a log-uniform distribution of time constants ($f(\log\tau)\mathrm{d}(\log\tau) = \text{const}$). Substituting Eq. (2.7) into (2.5) and then into Eq. (2.3) implies that the magnetization at time t will be

$$M_v(t) = \frac{H\chi_o}{\log(\tau_2/\tau_1)} \int_{\tau_1}^{\tau_2} \frac{\exp(-t/\tau)}{\tau} \mathrm{d}\tau \tag{2.8}$$

This integral is elementary,

$$M_v(t) = \frac{H\chi_o}{\log(\tau_2/\tau_1)} \left[\mathrm{E}_1(\frac{t}{\tau_2}) - \mathrm{E}_1(\frac{t}{\tau_1}) \right] \tag{2.9}$$

where E_1 is the exponential integral. Assuming $\tau_2 >> \tau_1$, then within the range $1/\tau_2 << t << 1/\tau_1$, $\mathrm{E}_1(t/\tau_1) \approx 0$, $\mathrm{E}_1(t/\tau_2) \approx -\gamma - \log(t/\tau_2)$ and it follows that

$$M_v(t) \approx \frac{H\chi_o}{\log(\tau_2/\tau_1)} \left(-\gamma - \log t + \log \tau_2\right) \tag{2.10}$$

where $\gamma \approx 0.577$ is the Euler constant. The approximation expressed in this equation breaks down as t approaches either endpoint. The above equations show how the ferrite magnetization changes with time and, therefore, the relevance of the effect to H-field sensors. Metal detectors measure $\partial H/\partial t$ so that the sensor reading is proportional to the change in the ferrite magnetization over-time. Within the same range where the $\log t$ behavior is evident in the H-field,

$$\frac{\mathrm{d}M_v(t)}{\mathrm{d}t} \propto \frac{-H\chi_o}{\log(\tau_2/\tau_1)} \frac{1}{t} \tag{2.11}$$

The most important aspect of the above equation is that the magnetic viscosity response will decay as $1/t$ at late-times in contrast to the eddy current response which decays as $t^{-5/2}$. For time-domain systems this characteristic decay of $1/t$ has been observed in archaeological prospecting (Colani and Aitken, 1996), time domain electromagnetic (TEM) surveys carried out over Laetril soils for mineral exploration (Buselli, 1982), and in UXO surveys on Kaho‘olawe Island, Hawaii (Ware, 2001).

2.2 Frequency dependent susceptibility and magnetic viscosity

The fact that the acquisition and decay of magnetization are not instantaneous means that a frequency-dependent susceptibility, $\chi_v(\omega)$ is required to explain the behavior of a system exhibiting magnetic viscosity. Due to causality (Fannin and Charles, 1995) the frequency dependent susceptibility is the one-sided Fourier transform of the impulse response (equivalent to the derivative of the step-off after-effect function),

$$\frac{\chi_v(\omega)}{\chi_o} = -\int_0^\infty \frac{\mathrm{d}F(t)}{\mathrm{d}t} \exp(-i\omega t)\mathrm{d}t \tag{2.12}$$

An elementary Fourier integral can be used to show that for a single relaxation time, the complex susceptibility model is

$$\chi_v(\omega) = \frac{\chi_o}{1 + i\omega\tau} \tag{2.13}$$

If the relaxation times are distributed with the weight function $f(\tau)$ then the complex susceptibility model becomes

$$\chi_v(\omega) = \chi_o \int_0^\infty \frac{f(\tau)}{1 + i\omega\tau} \mathrm{d}\tau \tag{2.14}$$

Assuming a log-uniform distribution of time constants (Fannin and Charles, 1995) the complex susceptibility becomes

$$\chi_v(\omega) = \chi_o \left(1 - \frac{1}{\log(\tau_2/\tau_1)} \log\left[\frac{1 + i\omega\tau_2}{1 + i\omega\tau_1}\right]\right) \tag{2.15}$$

An example of the susceptibility predicted by this model is given in Figure (2.1). Within a certain range of frequencies determined by the end-member time constants, the in-phase susceptibility will vary linearly with the logarithm of the frequency while the quadrature susceptibility is constant with frequency. Furthermore, for $\tau_2 >> \tau_1$ the slope of the in-phase and value of the quadrature susceptibility are related by (Dabas et al., 1992),

$$\frac{\partial \mathrm{Re}[\chi_v(\omega)]}{\partial \log \omega} = \frac{2}{\pi} \mathrm{Im}[\chi_v(\omega)] = -\frac{\chi_o}{\log(\tau_2/\tau_1)} \tag{2.16}$$

Thus there is a direct relationship between the susceptibility difference with frequency and the magnitude of the magnetic viscosity response. In Figure (2.1) we also show the measurement frequencies of the Bartington MS2-B and MS2-D probes. Until very recently, this was one of the only instruments available for measuring the frequency dependence of susceptibility.

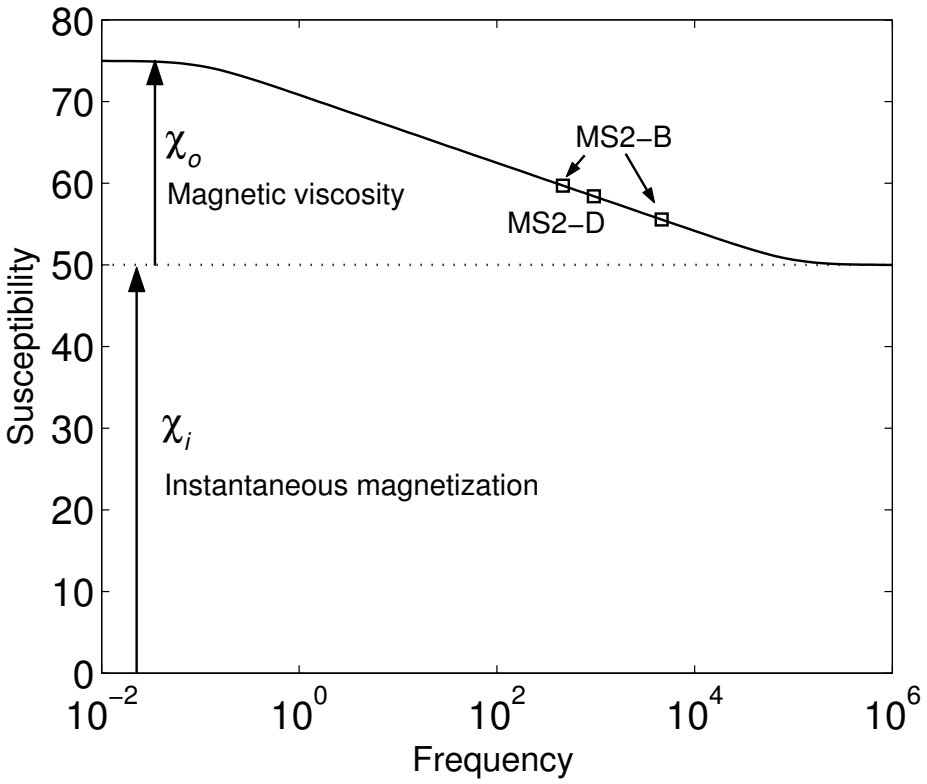

Figure 2.1: Schematic of the in-phase frequency dependent magnetic susceptibility showing the measurement points of the commonly used Bartington MS2-B and D probes.

2.3 Modeling the EM response under different scenarios

The geological response from an EM system results from both eddy currents induced in the Earth by the changing primary field, and the magnetic viscosity exhibited by magnetite and maghaemite. The eddy current response is usually referred to as the ground effect and exhibits a $t^{-5/2}$ decay in $\partial H/\partial t$. The amplitude of the ground effect depends on the conductivity and the area of the transmitter loop. With small loop systems the decay is usually so rapid that it has died out before the first time gate. However, with a large loop system in conductive terrain, the ground effect can cause a measurable response in the earlier time-channels.

We want to model the EM-response of a general conductive, permeable Earth that also exhibits viscous magnetization. To achieve this goal, we will consider the response at the center of a circular loop with radius a carrying a current of I amperes that sits on top of a half-space. We will assume that the transmitter has been on indefinitely and is rapidly shut off at time $t = 0$. We model the frequency domain response and then use digital filtering to predict the time domain response. From Ward and Hohmann (1987) the field at the center of the loop will be vertical,

$$H_z(\omega) = Ia \int_0^\infty \frac{2\lambda^2}{u_o(\lambda) + u_1(\lambda)/[1+\chi(\omega)]} \mathrm{J}_1(\lambda a)\mathrm{d}\lambda \tag{2.17}$$

where J_1 is a Bessel function and

$$u_o(\lambda) = \sqrt{\lambda^2 - k_o^2} \text{ and } u_1(\lambda) = \sqrt{\lambda^2 - k_1^2} \tag{2.18}$$

The wavenumbers k_o and k_1 are equal to

$$k_o^2 = \mu_o \epsilon \omega^2 \tag{2.19}$$

and

$$k_1^2 = \mu_o[1+\chi(\omega)]\epsilon\omega^2 - i\mu_o[1+\chi(\omega)]\sigma\omega \tag{2.20}$$

where σ is the conductivity of the half-space and ϵ is the permittivity of free space.

In Figure 2.2 we show the time-domain responses that occur for two different loop sizes ($a = 1$ and $a = 25$ m) and two different half-space conductivities ($\sigma = 0.01$ and $\sigma = 1$ S/m). The smaller conductivity is applicable to the soils on Kaho‘alawe Island, Hawaii, while the second represents a soil with a very high conductivity. We use the same susceptibility model as Pasion et al. (2002a) which was derived from soil measurements on Kaho‘alawe Island, Hawaii (Figure 2.3).

In general, the time-domain response consists of three stages. At the earliest times the eddy currents are distributed on the surface of the half-space and the $\partial H_z/\partial t$ response is flat. This corresponds to the so called inductive limit. At intermediate times, the current starts to move downwards and spreads out, with the $\partial H_z/\partial t$ response at the center of the loop decaying according to Equation 2.1 (that is at a rate proportional to $t^{-5/2}$). As mentioned previously, this intermediate time response is referred to as the ground effect (Ward and Hohmann, 1987). For large conductivities (Figure 2.2) the ground effect can retain sufficient amplitude at late enough times to interfere with the response from the metallic objects of interest. The third stage is the late-time response which is dominated by the magnetic viscosity and displays the characteristic $1/t$ decay.

In Figure 2.2 we also show the time domain responses that occur for (1) no magnetic viscosity ($\chi(\omega) = \chi_o$, the conductive response) and (2) no eddy currents ($\sigma = 0$, the magnetic response). Note that the oscillations at early time for the magnetic response are artifacts of the filter we use to convert to the time domain. The conductive response shows the classic ground effect decay of $t^{-5/2}$, while the magnetic response decays as $1/t$. When we add the two separate responses together the time-decay is almost exactly the same as the full modelling results which incorporated the eddy current plus magnetic viscosity response.

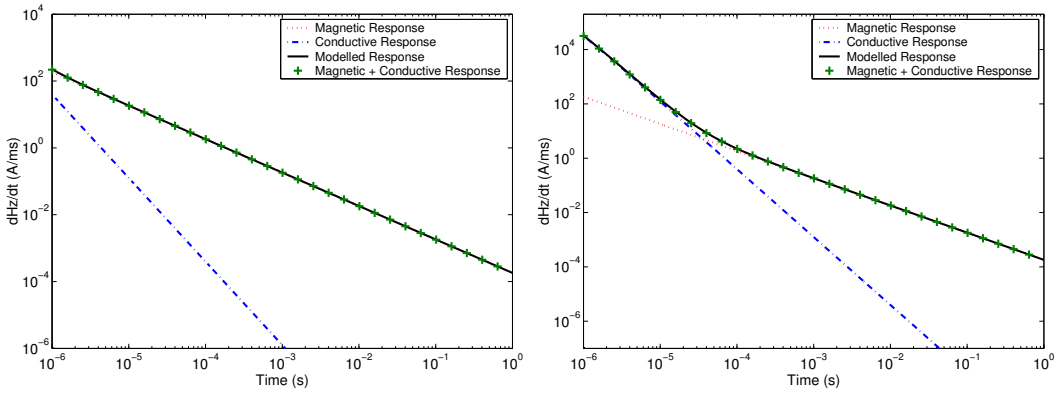

(a) $a = 1$ m; $\sigma = 0.01$ S/m (b) $a = 1$ m; $\sigma = 1$ S/m

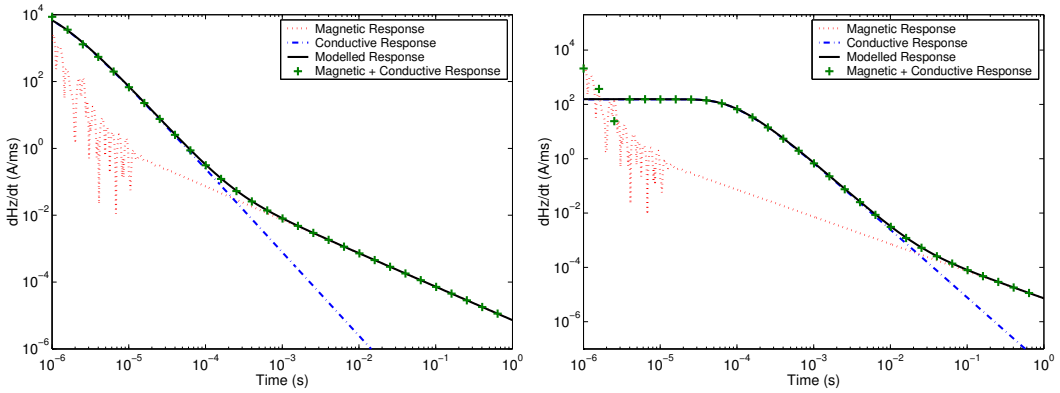

(c) $a = 25$ m; $\sigma = 0.01$ S/m (d) $a = 25$ m; $\sigma = 1$ S/m

Figure 2.2: Time-domain responses of half spaces exhibiting magnetic relaxation.

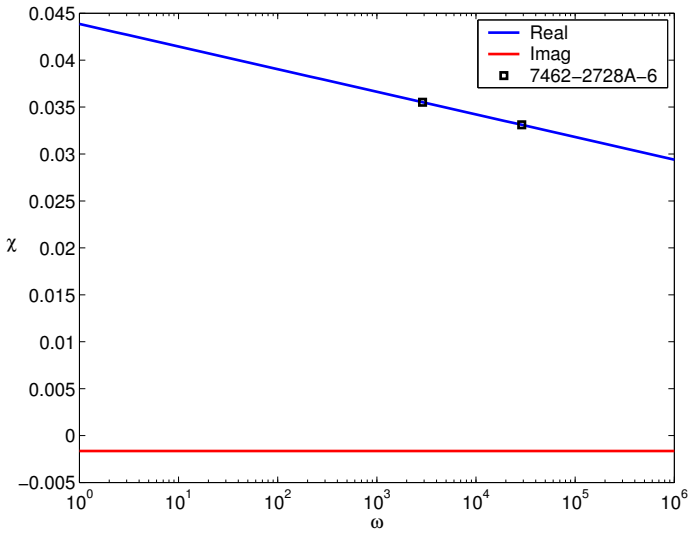

Figure 2.3: Susceptibility model based on frequency dependent susceptibility measurements of a Kaho'olawe, Hawaii soil sample.

There are two important implications of this result:

1. The eddy-currents do not interact with the magnetic relaxation of the ferrite;
2. The amplitude of the ferrite response will change with variations in ferrite concentration, but the decay will always be $1/t$ regardless of the spatial distribution of magnetic soil.

This last effect is in contrast to the response from the eddy-currents which depend strongly on geometry.

2.4 Example to motivate the need for differential measurements

To conclude this chapter we give an example of UXO detection in a magnetically hostile environment which motivates the need for differential measurements. Kaho'olawe is a single volcanic dome made of thin bedded pahoehoe (smooth, very fast moving lava) and 'a'a (rugged, slow moving lava) basalt (Stearns, 1940). The base rock is tholeiitic basalt, which is covered by a number of different soil types with variable geophysical characteristics (Parsons Engineering, 1998). Geonics EM63 time domain electromagnetic sensor data were collected on the island of Kaho'olawe, Hawaii as part of an ESTCP funded study to examine the effectiveness of electromagnetic sensors in highly magnetic environments (Putnam, 2001).

The Geonics EM63 time domain EM sensor has a 1 x 1m transmitter loop and a 40cm square receiver loop that measures the time derivative of the secondary field at geometrically spaced time gates. Figure 2.4 contains a plot of the sensor response at the first time gate (centered at $t = 0.180$ms) of the data collected over a pair of adjacent 30m square grids.

A zone of high susceptibility running from the south-west to the north-east corners of the grid is clearly seen in the data. In order to remove this long wavelength magnetic feature, we apply a 2-D median filter. The median filter successfully removed the long wavelength magnetic geology feature, but retains the many instances of smaller wavelength magnetic anomalies, of similar size to the anomalies of the buried metallic targets, in the survey grid (Figure 2.5).

In an attempt to reduce the number of magnetic geology anomalies, we fit each of the median filtered data set soundings with a magnetic soil model ($1/t$) and record the misfit value. This is equivalent to the χ^2 technique developed by Ware (2001). Figure 2.6 displays the image of the misfit over the grid.

Plotting the extent to which a soil model is unable to reproduce each sounding provided an image that suppressed much of the magnetic anomalies and retained, and in some cases strengthened, the anomalies of many of the buried metallic targets. However, several of the metallic targets anomalies (for example targets 9, 10, 14, and 20) are less evident when plotting the misfit values. This mixed result is not surprising when we look at the individual soundings of some of the targets (Figure 2.7).

The three worst fitting raw (i.e. non-median filtered) decays within a 1m x 1m square centered on targets 11, 14, 24, and 26 are plotted against the soil decay of a Geonics EM63. Target 26, a grid stake, has a very distinct anomaly in the misfit image since it clearly does not have a $1/t$ decay. Target 14, a 5 inch high explosive (HE) practice round (Figure 2.7(c)), is an example of the shortcomings of this decay comparison technique. Although target 14 has a clearly identifiable anomaly in the median filtered data set (Figure 2.5), its decay curves are nearly identical to the basalt decay and therefore has a very small misfit value.

The fact that a large UXO, such as a 5" HE round, can generate a time-decay virtually indistinguishable from soil, is cause for concern. Indeed, that is the very motivation for this study and provides strong incentive to look for differential measurement techniques that are able to stimulate a different response in the soil as compared to a compact metallic item.

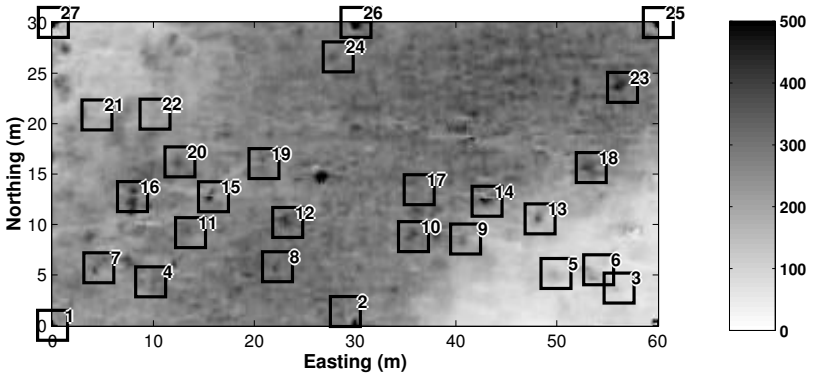

Figure 2.4: The first channel of Geonics EM63 data collected over a Kaho'olawe test grid.

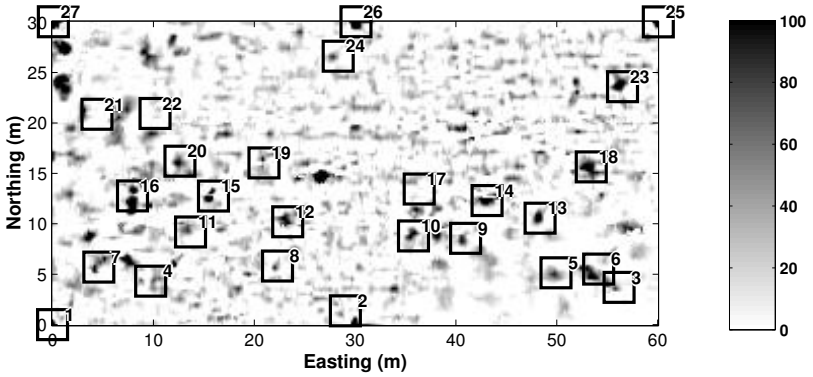

Figure 2.5: The first channel of median filtered Kaho'olawe data.

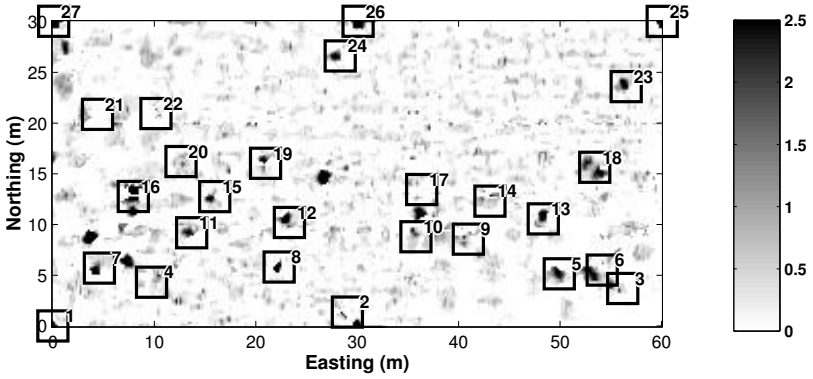

Figure 2.6: Misfit of each sounding when fit with the soil model

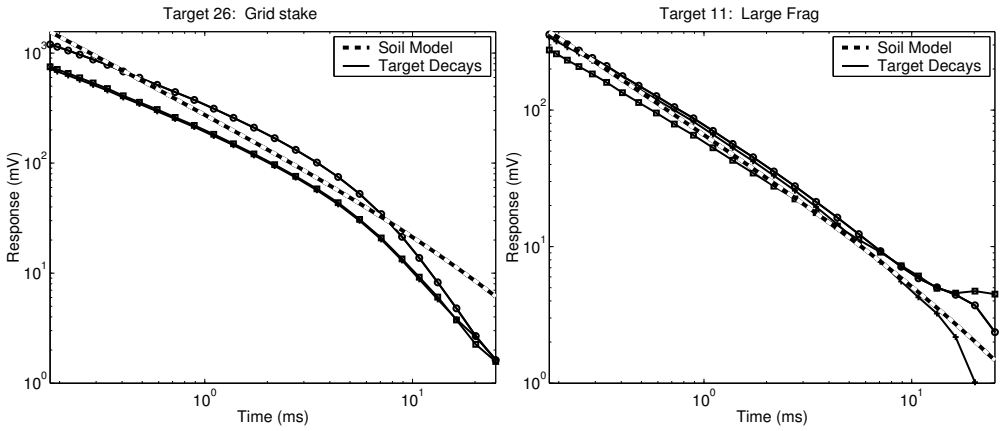

(a) Target 26

(b) Target 11

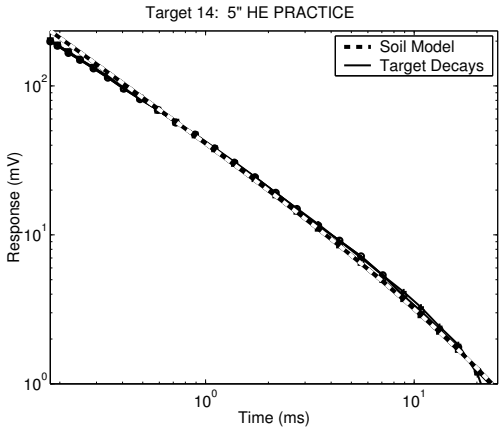

(c) Target 14

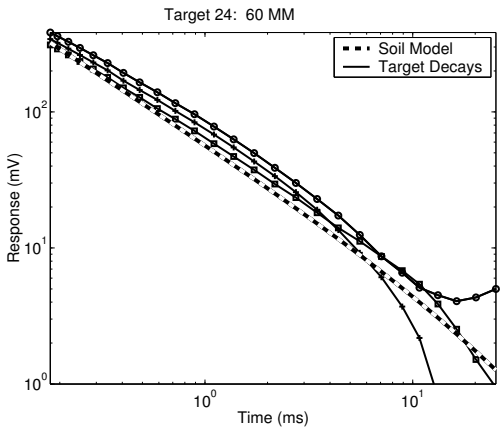

(d) Target 24

Figure 2.7: Comparison of the decay characteristic of Targets 11, 14, 24, and 26 of the Kaho'olawe test grid. A soil decay is plotted over the target decays for comparison.

Chapter 3

The concept of differential measurements

3.1 Introduction

Differential measurement is the process of acquiring successive geophysical data sets with different measurement parameters for each data set. If the changes in the response metal targets are more (or less) sensitive to changes in transmitter field than VRM soils, then, in principle, we can invoke special processing in the recorded data that exploit the differences in the recorded data.

Differential measurements can be made by modifying either the receiver or transmitter design of the sensor. Receiver modifications result in a different sampling of the secondary field created by the ground and any metallic targets. Possible modifications include the receiver loop size and position relative to the transmitter and target. Modifications to the transmitter result in changes to the primary field that will in turn have an impact on the secondary field measured by the receiver. Examples include the transmitter loop size and transmitter orientation, both of which modify the spatial characteristics of the primary field. To modify the temporal characteristics of the primary field, the transmitter waveform can be varied. This could be achieved, for instance, by changing the charge time or the shape of the waveform (e.g. from square-wave to triangular).

For this study we considered the following four differential measurements:

1. Receiver height;
2. Transmitter field direction;
3. Transmitter loop size; and
4. Transmitter waveform.

We now discuss the characteristics of each of these differential measurements and explain why we chose to focus on the transmitter waveform.

3.1.1 Differential measurements through receiver height variation

Since the voltage measured by a receiver loop is proportional to the change in the total flux of the magnetic field through the area of the loop, the loop acts as a spatially smoothing filter. Changing the loop height will sample the difference in spatial decay of the secondary field. A compact target (like a UXO) has a quicker spatial decay of the response than a subsurface that has laterally homogeneous electromagnetic material properties. As an example of the effect of receiver height variations we now model the response of a compact object (a sphere) and a two-layer earth, for the case of a vertical dipolar transmitter (a reasonable approximation to most transmitters).

The vertical component of the secondary field for a sphere with a radius a located directly beneath a vertically directed dipole m_r is

$$H_z = -\frac{m_r}{4\pi} e^{i\omega t} \sum_{n=1}^{\infty} S\left(ka\right) \frac{a^{2n+1}}{\left(rr_o\right)^{n+2}} n\left(n+1\right) P_n\left(\cos\theta\right) \tag{3.1}$$

where r_o is the distance from the dipole to the sphere and r is the distance from the observation point to the sphere center and

$$S\left(ka\right) = \frac{\left[\mu_o/2 - \left(n+1\right)\mu\right] I_{n+1/2}\left(ka\right) + \mu_o ka I'_{n+1/2}\left(ka\right)}{\left(\mu_o/2 + n\mu\right) I_{n+1/2}\left(ka\right) + \mu_o ka I'_{n+1/2}\left(ka\right)} \tag{3.2}$$

where $k = \sqrt{i\sigma\mu\omega}$, P_n are Legendre polynomials, and I is the modified Bessel function. The most significant term in this equation is the $n = 1$ term which shows that the field falls off as r^3 (for a fixed transmitter height).

To model the vertical field from a layered Earth we use Equation 3.5 below. We use the same earth model as Pasion et al. (2002b) which comprises a 1m thick magnetically viscous layer over a basement with no magnetic viscosity. The field from this layered earth, as illustrated in Figure 3.1, is considerably different than the r^3 falloff of the sphere. Differential height measurements will work quite well if the magnetic properties of the ground are relatively constant within the field of view of the transmitter, and if the ground surface is relatively flat. The EM data from Kaho'olawe Island that we discuss later in this report, show considerable variation in EM signal due to both micro-topography and rapid variations in the EM properties of the ground. Thus, we do not feel that a differential measurement process using receiver height variations will provide a general method to defeat problem soils.

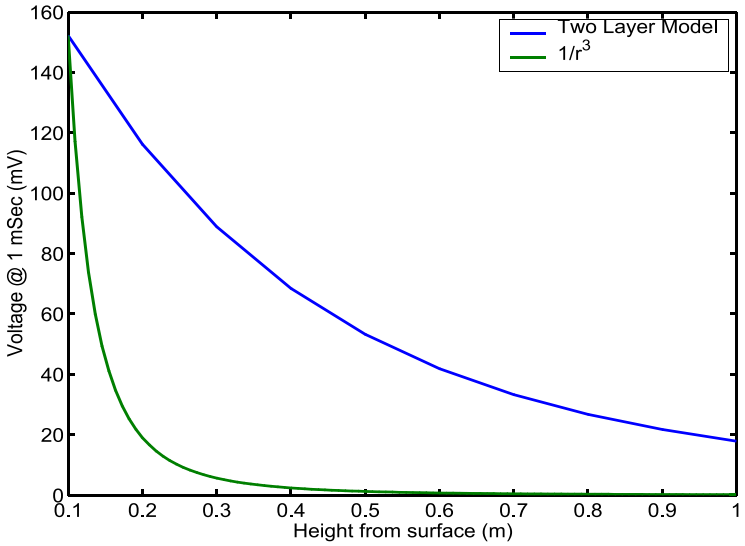

Figure 3.1: Decay in the secondary field with height for a homogeneous half-space and a sphere assuming a vertical dipolar transmitter field.

3.1.2 Differential measurements through varying the transmitter field direction

The primary field of a TEM sensor can be varied either spatially or temporally. A directional field would allow improved excitation of both the axial and transverse modes of a buried target, which would lead to

better target characterization by obtaining better estimates of the polarization tensor components. Improved detection in magnetic environments could be achieved by having control of the direction of the primary field. As mentioned earlier in this report, variations in transmitter fields were explored in detail by Pasion et al. (2002b).

As an example, consider a dipole transmitter illuminating a subsurface represented by a series of laterally homogeneous layers (which is an adequate assumption of geology in many cases). The three components of the H-field above the Earth model ($z < 0$) is:

$$H_x(x,y,z,\omega) = \frac{1}{4\pi}\frac{x}{r}\int_0^\infty \left(e^{-\lambda|z+h|} - \frac{P_{21}}{P_{11}}e^{-\lambda(z-h)}\right)\lambda^2 J_1(\lambda r)\,d\lambda \tag{3.3}$$

$$H_y(x,y,z,\omega) = \frac{1}{4\pi}\frac{y}{r}\int_0^\infty \left(e^{-\lambda|z+h|} - \frac{P_{21}}{P_{11}}e^{-\lambda(z-h)}\right)\lambda^2 J_1(\lambda r)\,d\lambda \tag{3.4}$$

$$H_z(x,y,z,\omega) = \frac{1}{4\pi}\int_0^\infty \left(e^{-\lambda|z+h|} + \frac{P_{21}}{P_{11}}e^{-\lambda(z-h)}\right)\lambda^2 J_0(\lambda r)\,d\lambda \tag{3.5}$$

for a z-directed magnetic dipole source at $(0,0,-h), h > 0$, and:

$$\begin{aligned} H_x(x,y,z,\omega) = &-\frac{1}{4\pi}\left(\frac{1}{r} - \frac{2x^3}{r^3}\right)\int_0^\infty \left(e^{-\lambda|z+h|} - \frac{P_{21}}{P_{11}}e^{-\lambda(z-h)}\right)\lambda J_1(\lambda r)\,d\lambda \\ &-\frac{1}{4\pi}\frac{x^2}{r^2}\int_0^\infty \left(e^{-\lambda|z+h|} - \frac{P_{21}}{P_{11}}e^{\lambda(z-h)}\right)\lambda^2 J_0(\lambda r)\,d\lambda \end{aligned} \tag{3.6}$$

$$\begin{aligned} H_y(x,y,z,\omega) = &\frac{1}{2\pi}\frac{xy}{r3}\int_0^\infty \left(e^{-\lambda|z+h|} - \frac{P_{21}}{P_{11}}e^{\lambda(z-h)}\right)\lambda J_1(\lambda r)\,d\lambda \\ &-\frac{1}{4\pi}\frac{xy}{r^2}\int_0^\infty \left(e^{-\lambda|z+h|} - \frac{P_{21}}{P_{11}}e^{\lambda(z-h)}\right)\lambda^2 J_0(\lambda r)\,d\lambda \end{aligned} \tag{3.7}$$

$$H_z(x,y,z,\omega) = \frac{1}{4\pi}\frac{x}{r}\int_0^\infty \left(e^{-\lambda|z+h|} + \frac{P_{21}}{P_{11}}e^{-\lambda(z-h)}\right)\lambda^2 J_1(\lambda r)\,d\lambda \tag{3.8}$$

for a x-directed magnetic dipole source at $(0,0,-h), h > 0$, where $u_o = \sqrt{\lambda^2 - k_o^2}$, k_o is the wave number of the air, and J_o and J_1 are the zeroth and first order Bessel functions, respectively. P_{21} and P_{11} are elements of the matrix $\mathbf{P}$:

$$\mathbf{P} = \mathbf{M}_1 \prod_{j=2}^{m} \mathbf{M}_j \tag{3.9}$$

where

$$\mathbf{M}_1 = \begin{bmatrix} \frac{1}{2}\left(1 + \frac{\mu_0 u_1}{\mu_1 u_0}\right) & \frac{1}{2}\left(1 - \frac{\mu_0 u_1}{\mu_1 u_0}\right) \\ \frac{1}{2}\left(1 - \frac{\mu_0 u_1}{\mu_1 u_0}\right) & \frac{1}{2}\left(1 + \frac{\mu_0 u_1}{\mu_1 u_0}\right) \end{bmatrix} \tag{3.10}$$

$$\mathbf{M}_j = \begin{bmatrix} \frac{1}{2}\left(1 + \frac{\mu_{j-1} u_j}{\mu_j u_{j-1}}\right) & \frac{1}{2}\left(1 - \frac{\mu_{j-1} u_j}{\mu_j u_{j-1}}\right) \\ \frac{1}{2}\left(1 - \frac{\mu_{j-1} u_j}{\mu_j u_{j-1}}\right) e^{-2u_{j-1}t_{j-1}} & \frac{1}{2}\left(1 + \frac{\mu_{j-1} u_j}{\mu_j u_{j-1}}\right) e^{-2u_{j-1}t_{j-1}} \end{bmatrix} \tag{3.11}$$

The thickness of the j^{th} layer is t_j, and μ_j is the magnetic permeability of the layer. A vertical dipole (or horizontal loop) transmitter produces an null half-space response in the horizontal component (Pasion

et al., 2002a). Conversely, a horizontal dipole (or vertical loop) transmitter will produce a null response in the vertical direction. Both of these geometries produce a response for compact targets. Therefore, by controlling the spatial characteristics of the transmitting field, the symmetry of the half-space could be exploited to null the geologic response. This indeed, is the key point.

This assumption of a half-space response will not apply if there is significant micro-topography or if soil properties change appreciably within the field of view of the detector. As we demonstrate in Chapter 5, these effects have a marked effect on the data collected at Kaho'olowe Island. Thus, this method has a similar disadvantage to differential measurements using receiver height, and would be unlikely to work under certain real-world conditions.

The null-coupling of the transmitter and receiver fields is only one mechanism for exploiting differential measurements based on transmitter field direction. We believe that a much more promising method could be developed around the characteristic that the form of the magnetic soil response is invariant to the spatial distribution of magnetic soil. Thus, for an ideal step-off transmitter, the soil response will be $1/t$ regardless of the direction of the transmitter field. In contrast, the UXO response will vary as axial and transverse modes of the targets are stimulated by different amounts as the transmitter field direction is varied. We believe that this effect could form the basis of a very promising tool for EM detection and discrimination in magnetic soil environments. There are several research projects funded by SERDP that are developing instrumentation with directional control of the primary field. However, at the time this study was conducted, no systems were available. Thus, we defer any further discussion of this differential measurement until the concluding chapter.

3.1.3 Differential measurements through varying the transmitter loop size

The loop size of a transmitter will also alter the primary field. We only briefly consider this effect here, as it does not result in a useful differential measurement (but was one of the ideas we had at the outset of the project). Let us consider a circular transmitter loop of radius a, carrying a current I, and at a height h above a 1-D layered earth. At an observation point z above the ground and a radial distance ρ from the axis of circular transmitter loop, the vertical component H_z and the radial component H_ρ of the H-field are

$$H_\rho(\omega) = \frac{Ia}{2}\int_0^\infty \left[e^{-u_o(z+h)} - \frac{P_{21}}{P_{11}}e^{u_o(z-h)}\right]\lambda J_1(\lambda a)\, J_1(\lambda\rho)\, d\lambda \tag{3.12}$$

$$H_z(\omega) = \frac{Ia}{2}\int_0^\infty \left[e^{-u_o(z+h)} + \frac{P_{21}}{P_{11}}e^{u_o(z-h)}\right]\frac{\lambda^2}{u_o} J_1(\lambda a)\, J_o(\lambda\rho)\, d\lambda \tag{3.13}$$

We consider the vertical field at the center of the loop so that $\rho = 0$. For a non conductive, but susceptible, half-space and assuming a quasi-static situation, $u_o = u_1 = \lambda$. The field is then

$$H_z(\omega) = \frac{Ia}{2}\int_0^\infty \left[1 + \frac{\mu_1 - \mu_0}{\mu_1 + \mu_0}e^{-2u_o h}\right]\lambda J_1(\lambda a)\, d\lambda \tag{3.14}$$

By expanding the term in brackets we find:

$$\begin{aligned} H_z(\omega) &= \frac{Ia}{2}\left(\frac{\chi}{2+\chi}\right)\int_0^\infty e^{-2h\lambda}\lambda J_1(\lambda a)\, d\lambda + \frac{Ia}{2}\int_0^\infty \lambda J_1(\lambda a)\, d\lambda \\ &= \frac{Ia}{2}\left(\frac{\chi}{2+\chi}\right)\frac{a}{\left[a^2 + (2h)^2\right]^{3/2}} + \frac{Ia}{2}\left[\frac{1}{a^2}\right] \end{aligned} \tag{3.15}$$

To obtain the secondary field at the center of a loop on the ground ($h = 0$), we subtract the primary field (which is equivalent to the second term) and are left with

$$H_z^s(\omega) = \frac{I}{2a}\left(\frac{\chi}{2+\chi}\right) \tag{3.16}$$

Thus, for a fixed transmitter current, the secondary field from the ground will decrease as $1/a$.

For a sphere in the field of a circular loop, the response can be approximated by the expressions for a sphere in a uniform field provided that the radius of the sphere is much smaller than the loop radius, and provided that the sphere is not located near to the transmitter loop wire. Let us consider a sphere with a radius R located coaxial with the center of loop ($\rho = 0$). The primary field will be in the vertical direction only. The vertical component of the secondary field for a sphere with a radius R is:

$$\begin{aligned} H_z &= -\frac{3}{2}R^3 H_o S(\omega)\left(-\frac{1}{r^3}+\frac{3z^2}{r^5}\right) \\ &= -\frac{3}{2}R^3 H_o S(\omega)\left(\frac{2}{r^3}\right) \end{aligned} \tag{3.17}$$

where

$$S(\omega) = -\frac{2}{3}\frac{2\mu_1(\sinh\alpha - \alpha\cosh\alpha) + \mu_2\left(\sinh\alpha - \alpha\cosh\alpha + \alpha^2\sinh\alpha\right)}{2\mu_1(\sinh\alpha - \alpha\cosh\alpha) - 2\mu_2(\sinh\alpha - \alpha\cosh\alpha + \alpha^2\sinh\alpha)} \tag{3.18}$$

where

$$\alpha = \left(i\sigma_1\mu_1 - \epsilon_1\mu_1\omega^2\right)^{1/2} R \tag{3.19}$$

and H_o is the magnitude of applied uniform field, and the subscript 1 indicates properties applying to the sphere and the subscript 2 indicates properties of the surrounding medium, and r is the distance of the observation point from the sphere center. The primary field is due to a circular loop, where the sphere is coaxial to the loop, is

$$H_o = \frac{Ia^2}{2\left(z^2+a^2\right)^{3/2}} \tag{3.20}$$

where a is the radius of the loop. Note that we assume that the field at the center of loop is mainly uniform and in the z-direction. For a large loop $z \ll a$ and the primary field will be approximately $H_o = I/(2a)$. Therefore the half-space and sphere response at the center of a circular loop would scale with the loop radius as $1/a$ and any differential measurement based on varying a would not provide useful discriminatory information.

3.1.4 Differential measurements through varying the transmitter waveform

The last differential measurement we consider involves varying the transmitter waveforms. Candy (1996) describes a metal detector that utilizes different pulse lengths to differentiate the response of a metal target from the ferrite response. The transmitter waveform used in the Candy system is a linear on ramp (as opposed to a rectangular pulse). Metal and ferrite have different time decays for different ramp on-times Δt, with the ferrite response assumed to be

$$\frac{\mathrm{d}M(t)}{\mathrm{d}t} \propto \left[\log(1+\frac{\Delta t}{t}) - \frac{\Delta t}{t}\right] \tag{3.21}$$

Candy's system uses this equation to develop linear combinations of different integration windows that cause the ferrite response to sum to zero. This methodology has been applied in the development of the Minelabs F1A4 detector, which has been used successfully in the demining community. The detector's primary disadvantage for UXO applications is a relatively shallow depth of detection (compared to say, the Geonics EM-61). In addition, details of the integration windows and their linear summation are proprietary so that the metal detector output cannot be used in physics based models.

Of all the differential measurements, we believe that modifications to the transmitter waveform have the most promise. In the remainder of this chapter we review how the transmitter waveform alters the VRM response of soils and discuss possible mechanisms for differential measurements.

3.2 Effect of transmitter waveform

The effect of different transmitter waveforms can be modelled by considering how the transmitter characteristics change the distribution of relaxation times that are excited. We start by considering the effect of the transmitter waveform on a single relaxation time. Eqs. (2.3) and (2.4) give the change in magnetization following turn-off of a rectangular pulse that has been on indefinitely. Differentiating once will give the $\mathrm{d}M/\mathrm{d}t$ response to a step-off pulse, while differentiating twice will give the impulse response,

$$\frac{\mathrm{d}M_i(t)}{\mathrm{d}t} = -\frac{\chi_o \exp(-t/\tau)}{\tau^2} \tag{3.22}$$

For an arbitrary waveform, $g(t)$, that is assumed to turn-off at time $t = 0$ the change in ferrite magnetization is obtained by convolution with this impulse response,

$$\frac{\mathrm{d}M(t)}{\mathrm{d}t} = -\chi_o \int_{-\infty}^{0} g(t') \frac{\exp(-(t-t')/\tau)}{\tau^2} \mathrm{d}t' \tag{3.23}$$

For a rectangular pulse of amplitude H that turned on at $t = -\Delta t$ and then off at $t = 0$, this integral is elementary and

$$\frac{\mathrm{d}M(t)}{\mathrm{d}t} = H\chi_o \frac{[1 - \exp(-\Delta t/\tau)]}{\tau} \exp(-t/\tau) \tag{3.24}$$

For $\tau << \Delta t$, the response will be almost identical to the step-off case. However, as τ approaches Δt and then exceeds it, not enough time elapses for particles with that time-constant to significantly change orientation during the transmitter on-time. This will cause a reduction in the amplitude of the response.

Assuming a log-uniform distribution of time constants (Eq. 2.7), the overall system response is obtained by a weighted sum of the response from each time-constant,

$$\frac{\mathrm{d}M(t)}{\mathrm{d}t} = H\chi_o \int_{\tau_1}^{\tau_2} \frac{[1 - \exp(-\Delta t/\tau)] \exp(-t/\tau)}{\log(\tau_2/\tau_1)\tau^2} \mathrm{d}\tau \tag{3.25}$$

which can be shown to be

$$\frac{\mathrm{d}M(t)}{\mathrm{d}t} \approx \frac{H\chi_o}{\log(\tau_2/\tau_1)} \left[\frac{1}{t} - \frac{1}{t + \Delta t}\right] \tag{3.26}$$

where we have neglected the influence of the exponential as in deriving Eq. (2.11). At times $t << \Delta t$ the second term in this equation is very small and the response approaches $1/t$ (Figure 3.2). As t approaches Δt the second term becomes more and more important and the time-decay falls off faster than $1/t$. From Eq. (3.26) it is apparent that at very late times relative to Δt the time-decay will approach $1/t^2$.

The response of the magnetization to a rectangular pulse can be derived by following the same procedure outlined above. The resulting expression for the decay magnetization is

$$M(t) \approx \frac{H\chi_o}{\log(\tau_2/\tau_1)} \log\left(1 + \frac{\Delta t}{t}\right) \tag{3.27}$$

We note that Candy's expression in Eq. 3.21 results directly by starting with Eq. 3.23 and assuming $g(t) = t + \Delta t$ for $-\Delta t < t < 0$.

For this report, we will study the effectiveness of varying the transmitter waveform characteristics applied to an EM61-MK2 sensor and an EM63 time domain electromagnetic sensor. The waveforms that we will consider consists of an exponential current increase followed by a linear ramp off:

$$g(t) = \begin{cases} 1 - \exp\left[-\frac{(t+T_a+T_b)}{Tx}\right] & ,\text{if} -(T_a + T_b) < t < -T_b \\ -\dfrac{[1 - \exp(-T_a/T_x)]}{b} \;\; t & ,\text{if} -T_b \leq t < 0 \end{cases} \tag{3.28}$$

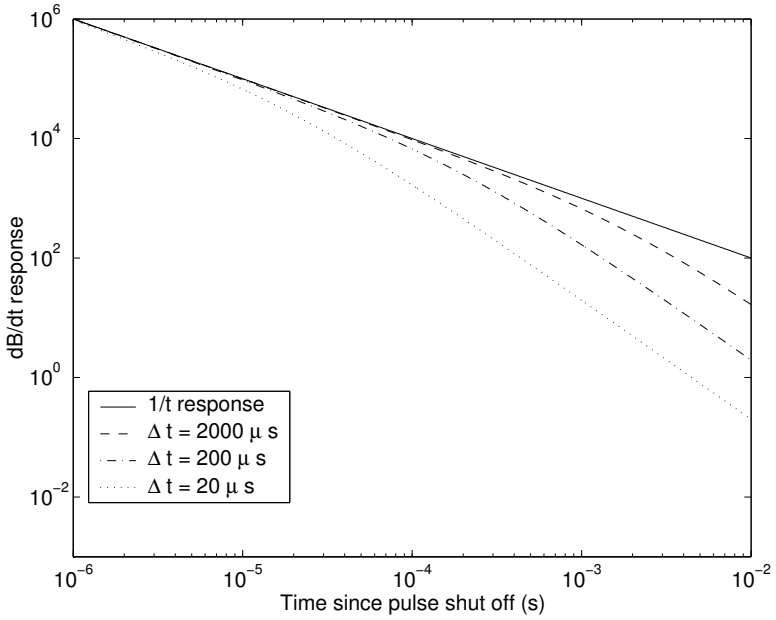

Figure 3.2: Effect of pulse length on the ferrite decay.

where T_a is the length of the exponential charge up, T_x is the time constant of the transmitter loop, and T_b is the length of the turn-off ramp. Specific details of the different transmitter waveform characteristics used in this study will be outlined in the following chapter. Following the same integration as in the previous examples,

$$\frac{dM\left(t\right)}{dt} \approx \frac{-\chi_o}{\ln\left(\tau_2/\tau_1\right)} \left[\frac{e^{\left(-\frac{t+T_a+T_b}{T_x}\right)}}{T_x} \left(Ei\left(\frac{t+T_b}{T_x}\right) - Ei\left(\frac{t+T_a+T_b}{T_x}\right)\right) + \frac{\alpha}{T_b} \ln\left(1+\frac{T_b}{t}\right) \right] \tag{3.29}$$

where Ei is the exponential integral and $\alpha = 1 - \exp\left(-T_a/T_x\right)$. We note that the expression (3.26) for a finite length pulse can be obtained by taking the limit as $T_b \rightarrow 0$ (i.e. ignoring the ramp-off part of the transmitter waveform) and $T_x \rightarrow 0$ (i.e. assuming an instantaneous current turn-on). Expression (3.21) for a ramp on current can be obtained from (3.29) by taking the limit as $T_b \rightarrow 0$ and assuming T_x is large enough relative to T_a and t such that the transmitter waveform is approximately a ramp on. In such a case, we can apply expansions $e^x \approx 1 + x$ and $Ei(x) \approx \gamma + \ln(x) + x$ to obtain (3.21).

For completeness we note that to obtain a closed form expression for an arbitrary waveform $g(t)$, and an arbitrary distribution of time constants, $f(\tau)$ we can form a weighted integration of Eq. (3.23) and find

$$\frac{\mathrm{d}M(t)}{\mathrm{d}t} = \chi_o \int_0^\infty f(\tau) \int_{-\infty}^0 g(t') \frac{\exp(-(t-t')/\tau)}{\tau^2} \mathrm{d}t' \mathrm{d}\tau \tag{3.30}$$

This expression is somewhat unwieldy to use so we note that if we again assume a log-uniform distribution of time-constants, then

$$\frac{\mathrm{d}M(t)}{\mathrm{d}t} = \frac{\chi_o}{\log(\tau_2/\tau_1)} \times \int_{-\infty}^0 g(t') \int_{\tau_1}^{\tau_2} \frac{\exp(-(t-t')/\tau)}{\tau^3} \mathrm{d}\tau \mathrm{d}t' \tag{3.31}$$

Now for times $1/\tau_2 << t << 1/\tau_1$,

$$\int_{\tau_1}^{\tau_2} \frac{\exp(-(t-t')/\tau)}{\tau^3} \mathrm{d}\tau \approx \frac{1}{(t-t')^2} \tag{3.32}$$

so that

$$\frac{\mathrm{d}M(t)}{\mathrm{d}t} \approx \frac{\chi_o}{\log(\tau_2/\tau_1)} \int_{-\infty}^{0} \frac{g(t')}{(t-t')^2} \mathrm{d}t' \tag{3.33}$$

We note that this expression can also be obtained by starting with the assumption that the step-off response is $1/t$ and then working backwards to include convolution with an arbitrary waveform (Das, pers. comm., 2003).

3.3 Theoretical results

We demonstrate the effect the length of the transmitter on-time has on the time domain response by modelling the response of four different targets: a complex susceptible halfspace, a 20cm diameter sphere of complex susceptible material, a 5cm diameter steel sphere, and a 5cm diameter aluminum sphere. The complex susceptibility of Figure 2.3 is assigned to the halfspace and complex sphere. Steel is modelled with a conductivity $\sigma = 3.54 \times 10^6 S/m$ and magnetic permeability of $\mu = 150\mu_o$. Aluminum is modelled with a conductivity $\sigma = 1 \times 10^7 S/m$ and $\mu = \mu_o$. For each model the primary current is generated by a circular, 1m diameter loop which carries a current of 1 amp. The measurement point is located at the center of the transmitter loop. The transmitter loop is placed on the halfspace surface for the simulated halfspace response, and is located at a distance of 15 cm directly over the complex susceptible sphere, and 10cm directly over the steel and aluminum sphere. The transmitter waveform consists of a single rectangular pulse.

Figure 3.3 demonstrates the effect of the different transmitter on-times on the $\partial H/\partial t$ response. We consider pulse lengths of 20 ms , 2000 μs, 200 μs, and 20 μs. The response of the aluminum sphere to a rectangular pulse of length 20 ms is similar to the response to a 2000 μs pulse length. This is because the time constant of the aluminum sphere ($\tau = \sigma\mu r^2/\pi^2 = 796\mu s$, where sphere radius $r = 2.5$cm) is shorter than the two longest pulse lengths of this simulation. The steel sphere has a time constant of $42.3ms$. To quantify the difference between the response of magnetic soils with the metal targets, a magnetic soil model, based on Eq. 3.26, is fit to the modelled response. The soil model is defined as

$$\frac{\partial H}{\partial t} = A\left(\frac{1}{t} - \frac{1}{t+\Delta t}\right) \tag{3.34}$$

and we determine the constant A that minimizes the misfit between the synthetically generated $\partial H/\partial t$ response and the data predicted by the magnetic soil model for the four different on-time lengths. The data predicted by the best fit magnetic soil model are plotted as solid lines. Not surprisingly the forward modelled responses of the susceptible halfspace and sphere are fit very well by the magnetic soil model, while the steel and aluminum spheres have a much poorer fit and, consequently, a much larger misfit value. Figure 3.4 demonstrates the ability to fit the responses with an H-field soil model response based on Eq. 3.27. The soil model is defined as

$$H\left(t\right) = A\log\left(1 + \frac{\Delta t}{t}\right). \tag{3.35}$$

We determine the constant A that minimizes the misfit between the simulated $H(t)$ response and the data predicted by the magnetic soil model. As with the $\partial H/\partial t$ example, the calculated misfits indicate that the forward modelled responses of the susceptible halfspace and sphere are fit very well by the magnetic soil model, while the steel and aluminum spheres have a much poorer fit.

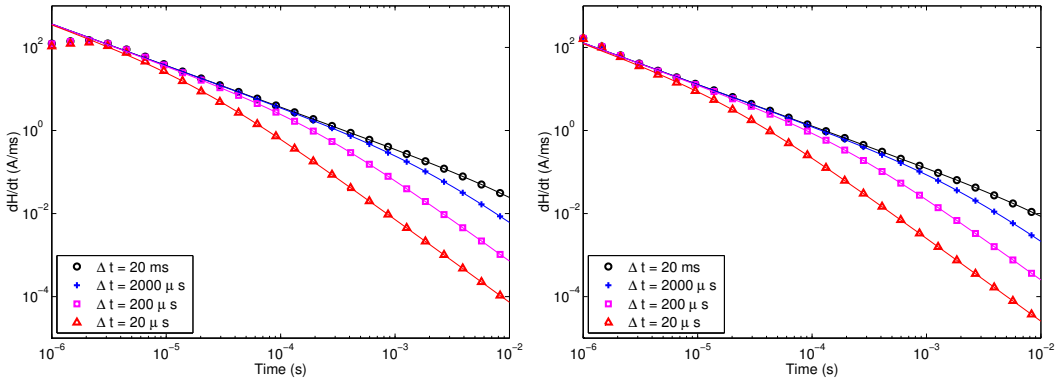

(a) Complex χ Halfspace - Misfit = 10.4

(b) Complex χ Sphere - Misfit = 0.722

(c) Steel Sphere - Misfit = 101.0

(d) Aluminum Sphere - Misfit = 439.5

Figure 3.3: $\partial H/\partial t$ responses for variable on-times. Solid lines represent the best fit magnetic viscous soil model.

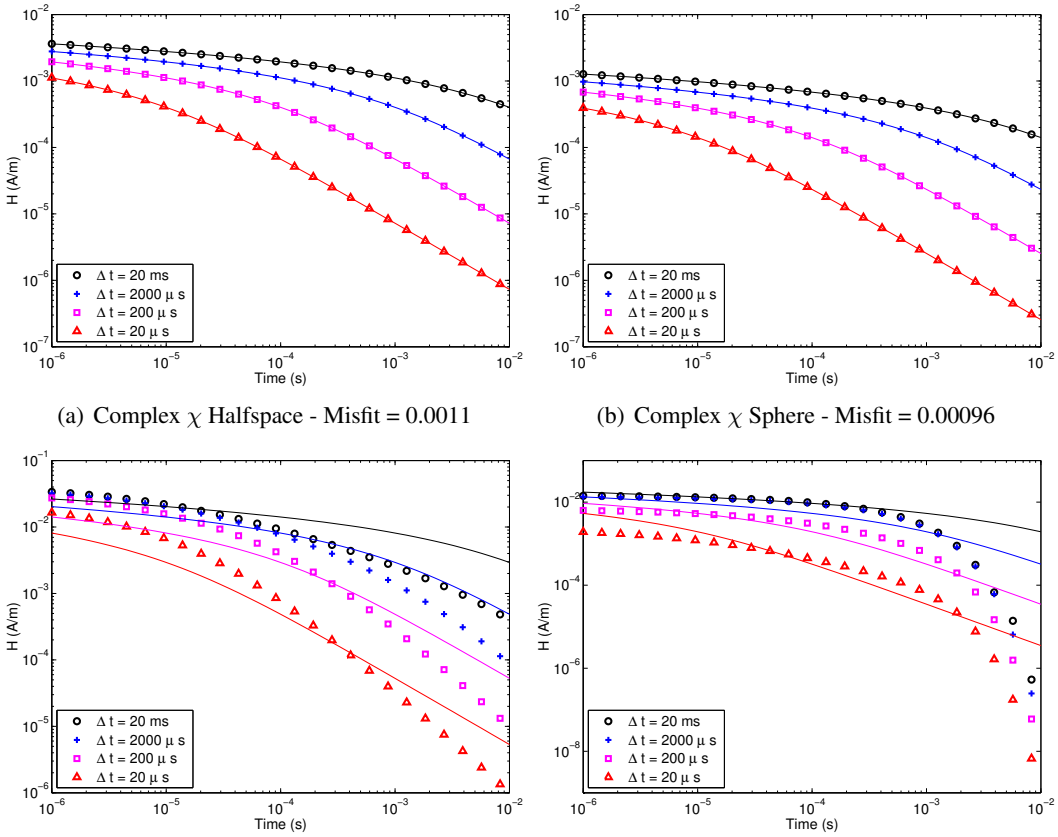

(a) Complex χ Halfspace - Misfit = 0.0011

(b) Complex χ Sphere - Misfit = 0.00096

(c) Steel Sphere - Misfit = 125.1

(d) Aluminum Sphere - Misfit = 878.5

Figure 3.4: $H(t)$ responses for variable on-times. Solid lines represent the best fit magnetic viscous soil model.

3.3.1 Discussion

The results in the last section are interesting, as they show that the form of the time-decay from magnetically viscous soil is independent of the spatial distribution of viscous material (the sphere and the half-space fit the same model equally well). This is a consequence of our assumption that the magnetic domains are non-interacting. We feel that is a valid assumption to make as the secondary fields generated from the viscous response are small relative to the primary field. This is somewhat equivalent to the situation in magnetostatics where the self-demagnetizing field is only significant when the susceptibility χ is large. Even for the soils in Kaho'alowe Island (which is considered highly magnetic), $\chi \sim 0.03$ so that self-demagnetization effects will be negligible.

In summary, we have shown that differential measurements based on varying the transmitter waveform are promising because the form of the time-domain response does not depend on the spatial distribution of the magnetic soil. This is in contrast to the other differential measurements proposed in this chapter (receiver height, transmitter field direction) as they make (or rely on) assumptions regarding the spatial distribution of the soil material. As our results from Kaho'olawe show, microtopography and small-variations in magnetic soil properties are significant and cannot be ignored in developing an effective method to defeat problem soils.

Chapter 4

Field studies on Kaho'olawe Island and the Waikoloa Maneuver Area

4.1 Introduction

For this study data collection efforts were undertaken at two sites in Hawaii. The first site was on the Former Navy Bombing Range on Kaho'olawe Island. Surveys were conducted on Grid 2E in Area A of the Demonstration Grid within the Navy QA range. A detailed description of Kaho'olawe and the Navy QA grid can be found in (Cargile et al., 2004b). The survey area was 30 x 30m. The grid is located on flat hard pan with minimal vegetation (pili grass). The only topography has been created by wind and rain erosion. Our visit to Kaho'olawe Island was motivated by the hostile soil environment on that island that had caused considerable difficulties to the Navy when they cleaned that site. According to Putnam (2001) almost 30% of anomalies that were excavated on the island were due to geology.

The second site was the former Waikoloa Maneuver Area on the Island of Hawaii. Surveys were conducted on the Waimea geophysical proveout (GPO) grid located near Waimea town. The GPO is located on rolling ranch land. There is a power substation adjacent to the ranch where the GPO is located but it did not adversely effect the data quality. The GPO contained three 30 x 30m grids, one was seeded (calibration grid), semi-seeded (blind grid) and one was un-seeded. Surveys were performed on the seeded and un-seeded grids at Waimea. There was also a GPO located near Waikoloa village, however this site was not surveyed in detail. The surface of the Waikoloa GPO was littered with cobble to boulder sized lava rocks that made surveying lines with a wheeled cart impossible. Static EM63 soundings were performed on the Waikoloa GPO in order to determine soil response.

Our visit to the Waikoloa Maneuver Area was motivated by the active munitions response efforts that are being conducted on that site. Verbal accounts from the site indicated that magnetic soils were causing problems to geophysical sensors. Thus, it offered an ideal opportunity to test the differential EM concept with the added advantage of possibly providing useful techniques for the ongoing munitions response actions.

In addition to detailed EMI surveys performed at each site a suite of geophysical and geological information was collected in support of two magnetic soil studies. The first study was the SERDP UX-1414:Improving Detection and Discrimination of UXO in Magnetic Environments project. The second study was an ERDC study being conducted by Ryan North. These studies involved the collection of ground magnetic data and Geonics EM38 data at each site. Surface samples for complex susceptibility and iron oxide analysis were collected. Bardington Susceptibility measurements were also taken at the soil sample locations. Four soil pits were dug (Kaho'olawe only) for analysis of soil horizons, sampling of different soil horizons and measurement of susceptibility using the Bardington. Oriented samples were also collected

from the surface for magnetic remanence measurements. The results from these additional surveys will be described in the annual and final reports for SERDP-UX1414.

4.2 Instrumentation

The objective of this study was to evaluate the effectiveness of illuminating a survey area with a number of different primary fields as a means to improve discrimination in magnetic environments. Since acquiring data using spatially variable fields was not possible, we explored varying the transmitter waveforms. In the previous chapter we showed the effect of changing the transmitter pulse length on the response of soils. The Geonics EM61MK2 and EM63 electromagnetic sensors were chosen for this project. Both sensors are pulse induction time domain electromagnetic sensors. The EM61MK2 was chosen for this project since it is one of the most common EM instruments used for UXO remediation projects. Although the EM63 serves mainly as a research instrument and not a production level sensor, it was selected due to its much longer measurement window and increased number of measurement channels. The EM63 would enable us to sample a larger portion of the decay curve and at a greater number of channels than the EM61.

The main TEM data collection platform was a modified Geonics EM61MK2 sensor. The design of the EM61 is such that a single electronics chip controls the transmitter waveform characteristics and the receiver times. Since it was not possible to transmit different charge-up times using a single chip, Geonics produced four chips, each with a different transmitter waveform and receiving times. The on-times of the chips were 10ms, 4ms, 2ms and 1ms. The 1ms chip, was not used in this study due to its inability to produce a stable signal. The different transmitter waveforms, with their specific on-times and measurement times are shown in Figure 4.1. The modified chips represent the largest possible range of on-times and measurement windows for the EM61MK2 sensor. The turn-on for each of the waveforms has the same exponential time constant of 3.46 ms and approximately the same linear ramp slope.

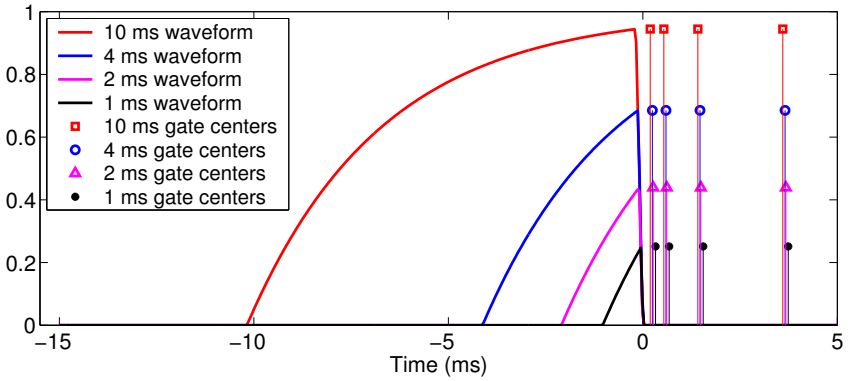

(a) Waveforms and measurement gate centers for the different chips.

Charge Time	Ramp Length	t1	t2	t3	t4
10	0.178	0.190	0.540	1.415	3.600
4	0.121	0.247	0.597	1.472	3.657
2	0.093	0.267	0.617	1.492	3.677
1	0.032	0.328	0.678	1.553	3.738

(b) Timing details for the different chips (all times in milliseconds)

Figure 4.1: Transmitter waveforms for the 4 Geonics EM61MKII.

The Geonics EM63 TEM sensor and Geonics PROTEM47 system were also brought to the site. Both systems are exponential on, ramp off time domain systems. The Geonics EM63 is a cart system that operates at two different repetition rates, resulting in two different on-times. The PROTEM47 was not designed for UXO detection, and involves laying a transmitter loop wire on the ground. The PROTEM47 was included in this study since it has greater transmitter waveform flexibility and largest time measurement window. We do not go into the details of the PROTEM47 system since, unfortunately, the system did not operate properly during our surveys, and did not produce any useable data.

4.3 Field Procedures

4.3.1 Positioning

Positioning for the surveys was provided by a Leica TPS1100 robotic total station (RTS). The RTS technology provides positional data superior to GPS and has the ability to provide high-accuracy data adjacent to wooded areas and within lightly wooded areas. The Leica TPS1100 is a motorized RTS that uses automatic target recognition to track the location of the prism and has a highly accurate distance/azimuth measurement system. This technology is ideally suited for UXO geophysical surveys, producing positional data with 3D accuracy of approximately 1cm at a 3-Hz rate.

The RTS base-station was set-up daily on one of the grid corners that had previously been established as local survey control at the various field sites. Positional accuracy was established by backsighting to a known point. When set-up on a known point was infeasible the RTS base-station location was determined using the resection method. This method triangulates between two known points to determine the position of the base station.

The positions were output from the RTS as a NMEA string and logged by the EM61 and EM63 data loggers in real-time.

4.3.2 Calibration

A standard calibration procedure was followed for daily calibration of instruments, drift correction and check of positional accuracy. In order to determine drift during the survey, static measurements were made in an area of low background response before and after a survey. These measurements were made on an elevated platform such that the coil was approximately 1.4m above the ground. The first measurement in this process determined the background response of the system. It was assumed that at this elevation the response from the ground was negligible. This measurement was referred to as the static measurement. The next step was the spike measurement during which a metallic object was placed at a repeatable location on the platform and the response was measured. Following the spike measurement another static measurement was made. By performing this set of measurements before and after a survey it was possible to determine the amount of drift that occurred during the survey and determine the correction that needed to be applied. When collecting EM63 data the system was zeroed on the platform prior to the first set of static/spike measurements. No zeroing was performed on the EM61.

In order to determine positional accuracy and to correct for slew errors, data were collected along a fixed calibration line with a metallic object placed at a precisely surveyed point on the line. The cart was pushed along the line and then pulled back along the same path. This slew test was performed before and after each survey. The data were used to checked for consistency (of response) and positional accuracy of the anomaly. By performing this set of measurements before and after a survey it was possible to determine if there was a lag or slew between the forward and reverse profiles. The measurements enabled us to apply a lag correction to the data, so that the positional and sensor data were on the same time base.

4.3.3 Data Collection

Survey procedures for the EM61 and EM63 were identical. Data were collected along parallel transects separated by 0.5m. Prior to data collection at each grid, the ends of the grid were marked with a measuring tape, and wooden stakes were placed at 2m intervals along the tape. Lengths of string were then run between the wooden stakes at each end of the grid. This lane marking, while time consuming, was done to ensure that subsequent passes over the grid traversed approximately the same path. Data were collected while walking slowly (approx. 2km/hour) to prevent sensor orientation and vibration issues. Traffic cones were placed at the start and end of the current line so the operator could easily keep track of which line to survey next.

At each of the sites one or more 30 x 30m grids were selected for surveying. The full grids were surveyed with the standard Geonics EM61 chip and with the EM63 using the medium repetition rate. After reviewing the data from these surveys a subset of the grid was selected for resurveying with all of the instruments.

In addition to the standard cart-type EMI systems the effect of variable waveforms using a fixed loop system was planned on Kaho'olawe. The system selected for the survey was the PROTEM-47. Two areas within Grid 2E were highlighted as having a high and low (relatively speaking) soil response. The plan within each area was to lay out a 10 x 10m transmitter loop and record data at various receiver locations within the loop while varying the transmitter repetition rate. We also planned to vary the size of the transmitter loop. These surveys were not carried out due to equipment problems.

4.3.4 Data Quality Control and Processing

Data were processed using the UXOLab package developed at the University of British Columbia. Data from calibration tests were used to determine the drift and lag correction needed for each survey. Quality control (QC) of the data consisted of examining the data for dropouts, noise spikes and navigational errors. If the data coverage and quality were acceptable the survey data were accepted. If the data failed QC it was recollected.

After the data passed initial QC full processing was performed. The processing steps included applying a lag correction and a drift correction using the calibration measurements.

4.4 Kaho'olawe Island

4.4.1 Field experiments

Grid 2E of the Navy QA grid was selected for surveying on Kaho'olawe. Figure 4.2 shows a plan of the survey area.

The decision to survey this grid was based on previously collected data (Ware, 2001), which showed a large variation in geologic response. Since two weeks of field work were scheduled for Kaho'olawe it was possible to collect all four configurations of the EM61 over the entire grid. EM63 data were collected using the medium repetition rate over two parts of Grid 2E for comparison purposes. Due to the large background geologic EM signal, micro-topographic variations produced significant effects in the data. The location of micro-topographic features are shown in Figure 4.3.

The microtopographic variations made it difficult to ensure that the positioning and quality of subsequent data-sets were adequate for the planned analysis. In order to collect highly repeatable data a 5x5m subset of the grid was selected for additional detailed surveying (magenta polygon in Figure 4.3). Wood planks were laid out along the wheel paths of the EM61 and EM63 to maintain consistent sensor positioning and orientation. Data were collected over the detailed grid with all four of the EM61 chips and both EM63 repetition rates.

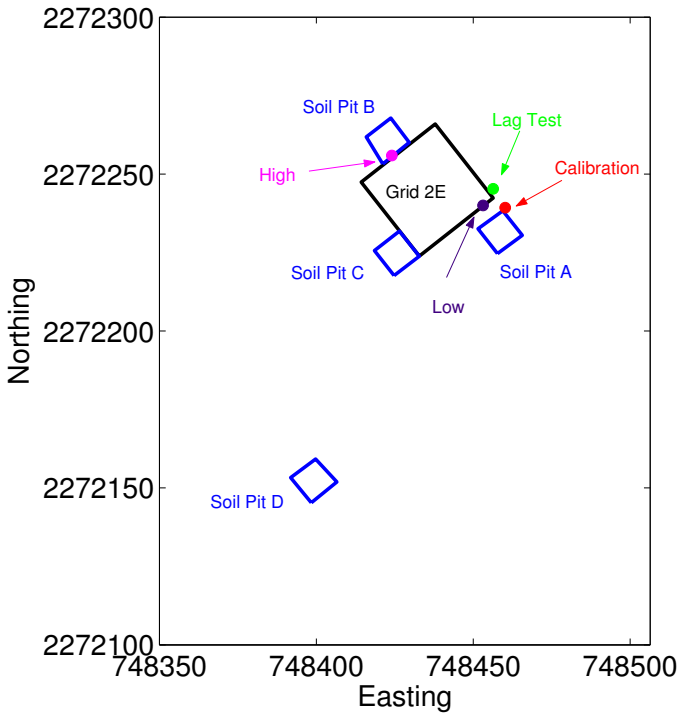

Figure 4.2: Overview of Grid 2E area. The black polygon shows the outline of grid 2E, the red dot is the location of the calibration measurements, the green dot is the location of the lag test, the cyan and purple dots are the locations of the high response and low response static measurements and the blue polygons represent the location of the four soil pits. The coordinates shown are UTM Zone 4, Nad 83 Hawaii.

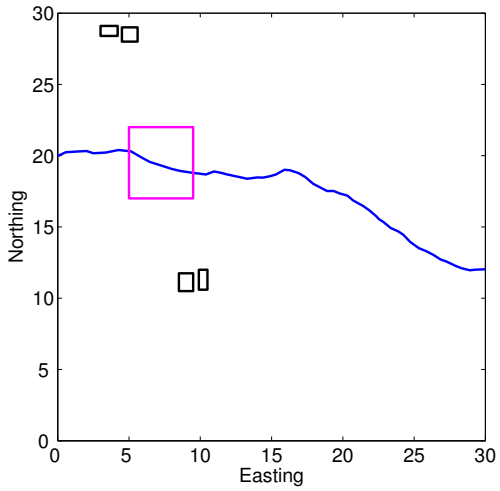

Figure 4.3: Topographic data from Grid 2E and location of surveys. The blue line represents the location of the rivulet running through the grid, the black polygons represent the location of a holes and the piles of dirt excavated from the hole and the magenta polygon indicates the location of the plank grid. The grid has been rotated and translated to local co-ordinates.

The UXO that were seeded in the QA grid were removed when the Navy left the Island. In order to simulate the response of buried metallic items on the grid a 90mm mortar and a large bolt (that was also used for the calibration tests) were placed at accurately surveyed positions within the detailed 5 x 5m grid (Table 4.1). Each detailed data set was collected with and without the objects.

Item	UTM Easting	UTM Northing	Local Easting	Local Northing
90mm Mortar	748427.53	2272243.44	7.90	18.67
Bolt	748425.35	2272242.38	5.53	19.18

Table 4.1: Locations of the 90mm mortar and the bolt used on the plank grid on Grid 2E.

4.4.2 Results

Grid 2E EM61 Data

Grid 2E was surveyed four times with different transmitter chips (standard EM61, 10ms, 4ms and 2ms). The gridded channel 1 response from the four surveys is shown in Figure 4.4.

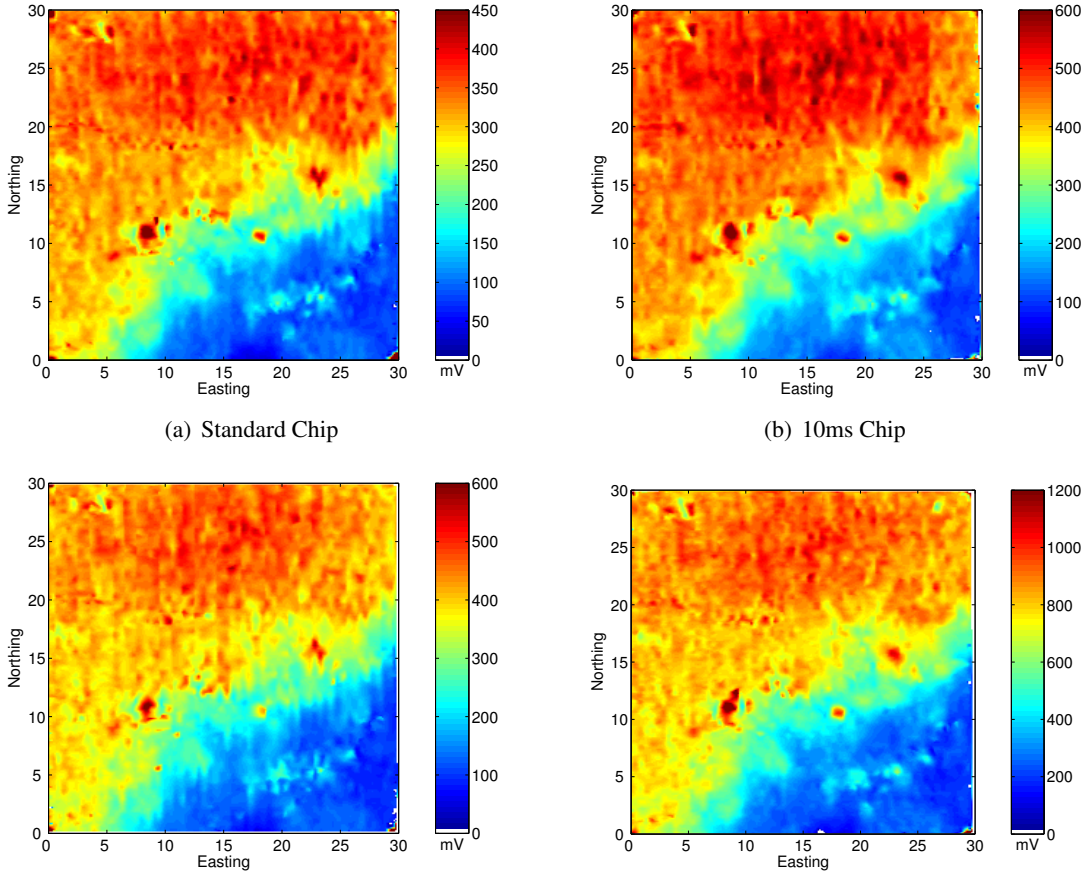

(a) Standard Chip

(b) 10ms Chip

(c) 4ms Chip

(d) 2ms Chip

Figure 4.4: Gridded images of channel 1 EM61 data collected on Navy QA Grid 2E using four different transmitter chips. Panel a) standard EM61 chip, b) 10ms chip, c) 4ms chip and d) 2ms chip. The grid has been rotated and translated to local co-ordinates.

The data from all four chips show the characteristic magnetic background response that was also evident in Ware (2001)'s EM-63 data. The large gradient across grid 2E is also clearly shown in the response from each chip. Some of the large amplitude small scale features are attributed to local small scale topographic variations (Figure 4.3).

The paired high and low responses at approximately 5m E, 27m N and 9m E, 11m N correspond to holes where emplaced UXO were removed from the grid. The linear feature on west side of grid 2E spanning from 0 to 15m E between 17 and 20m N correlates with a small (less than 10cm deep) rivulet that cross cuts the grid.

Grid 2E Plank Grid EM61 Data

The location of the grid is represented by the magenta polygon in Figure 4.3 and photographs of the grid are shown in Figure 4.5.

By collecting EM61 data on a smooth plank grid it was possible to eliminate any sudden changes of tilt. For the purpose of comparison, data were collected on the ground as well. Great care was taken to ensure that the paths of the two surveys were as similar as possible. Elevation data, both on the planks and on the ground, were collected in order to quantify coil height effects. Gridded images of the channel 1 EM61 data collected on the plank grid are shown in Figure 4.6.

Figure 4.5: Photographs of the detailed grid of planks established to investigate coil orientation within Grid 2E. The photo on the left shows the plank grid during surveying. The photo on the right shows a close up of the rivulet that runs through the grid.

Grid 2E EM63 Data

The EM63 system used on Kaho'olawe and at Waimea and Waikoloa was not in proper working order. When surveying using the medium repetition rate there were intermittent 50mV spikes. When surveying using the high repetition rate there were intermittent -3000mV spikes. Each of these spikes were three data points wide. When performing soundings, the data looked acceptable (ignoring the spikes), however when collecting data in survey mode the system exhibits an unexpected asymmetry. An example is shown in Figure 4.7. When the EM63 is pushed over the calibration bolt it produces an asymmetric anomaly (low then high), then as the EM63 is pulled back over the anomaly the response is asymmetric again (low then high). The position of the positive peak is dependent upon the direction the cart is moving. This type of anomaly should not be seen in a symmetric system like the EM63. It has been suggested that since the EM63 response is the difference of two coils there is likely a timing issue with one of the coils.

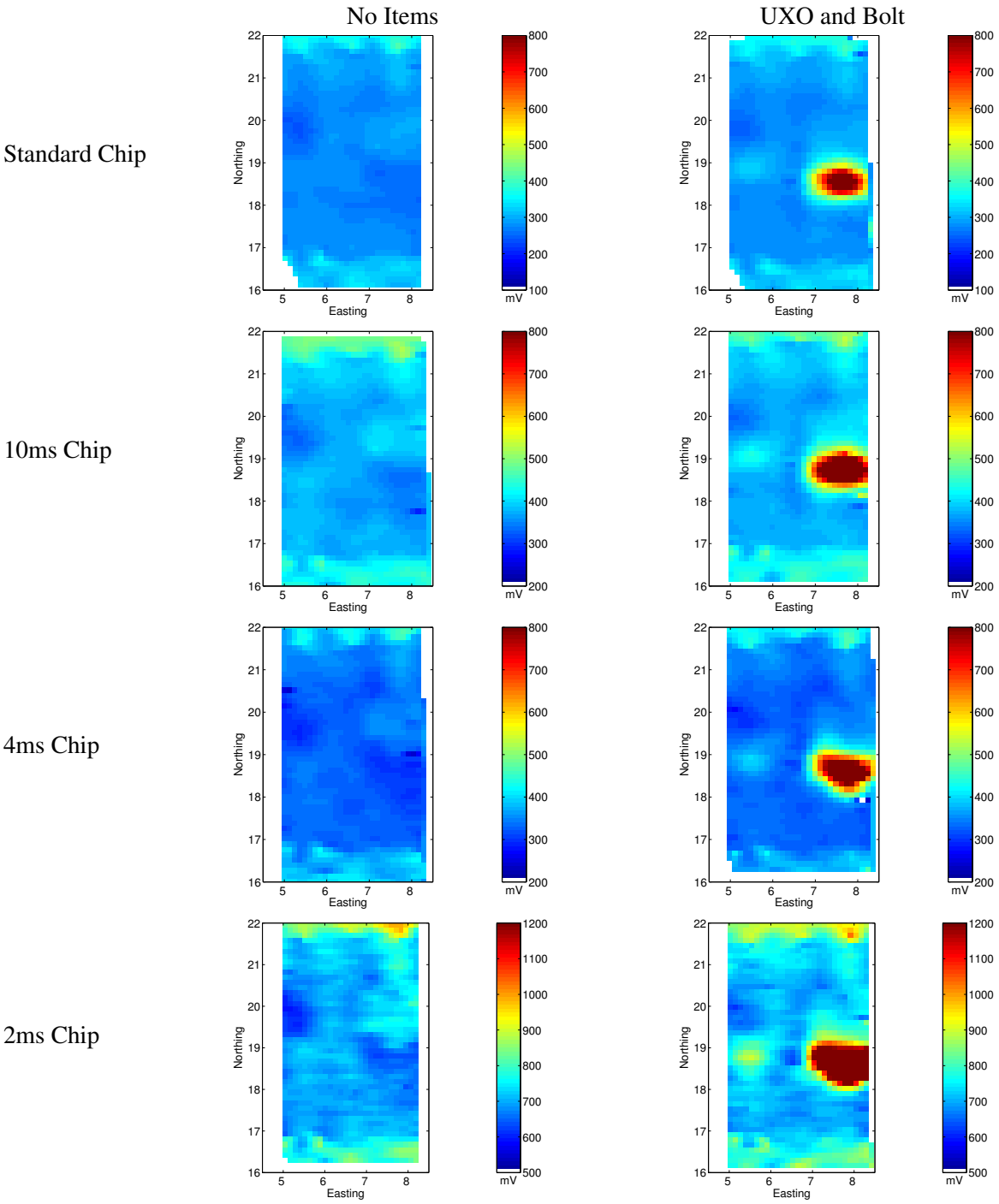

Figure 4.6: Gridded images of channel 1 EM61 data collected on plank grid. Panels on the left show data without any items on the grid and panels on the right show data with a bolt and a 90mm on the grid. The rows of panels (from top to bottom) show the Standard EM61 chip, the 10ms chip, 4ms chip and 2ms chip. The grid data has been rotated and translated to local co-ordinates.

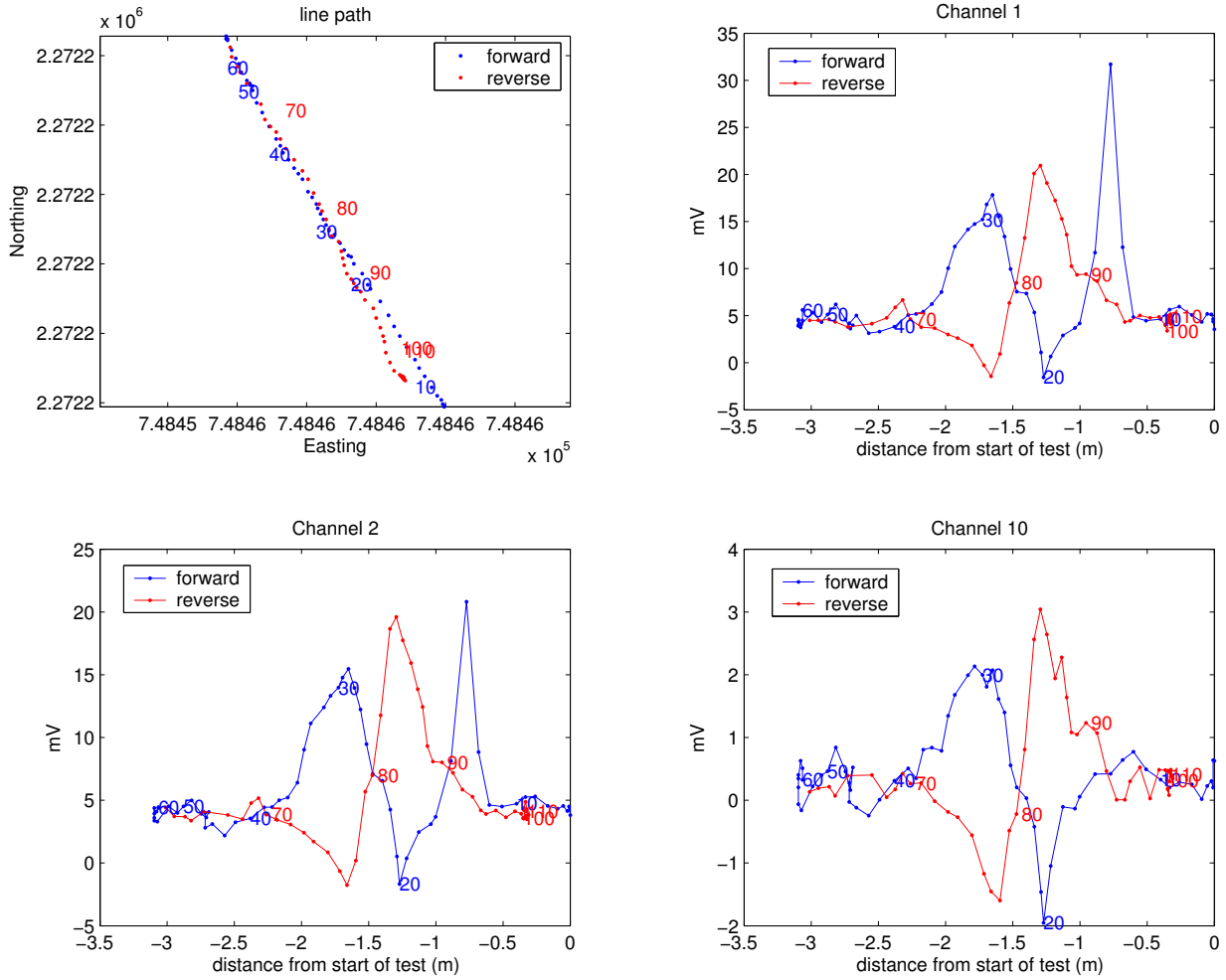

Figure 4.7: Lag test from Sept 28, 2004. EM63 data collected using the medium repetition rate.

While these problems make detailed analysis of the EM63 survey data impossible it is still possible to extract qualitative information from the data. Partial coverage of Grid 2E with the EM63 using the medium repetition rate (Figure 4.8) shows that the system is capable of reproducing the regional variation shown in the EM61 data. It is also possible to see some of the micro-topographic effects. The largest amplitude response (at approximately 8.5E, 11.3N) corresponds with the southern hole shown in Figure 4.3.

Grid 2E Plank Grid EM63 Data

EM63 data were collected over the plank grid using both the high and medium repetition rate, with and without the metallic items. The data are shown in Figure 4.9. The plank data exhibit the same asymmetrical anomalies as were observed in the lag test. The 90mm projectile response in the medium repetition rate data shows this quite well. The item was visible on three adjacent lines. The largest response occurs on the line at approximately 7.8 E which was surveyed from north to south. The two adjacent lines were surveyed south to north. The shape of the anomaly is the result of the erroneous asymmetry in the EM63 measurements.

Beyond the asymmetric nature of the anomalies we can also see that at the medium repetition rate the response from both the bolt and the 90mm projectile are visible in the gridded data. When using the high repetition rate only the UXO is visible. The bolt is not detectable. This is not surprising since the response of the bolt was not detectable during the high repetition rate calibration tests.

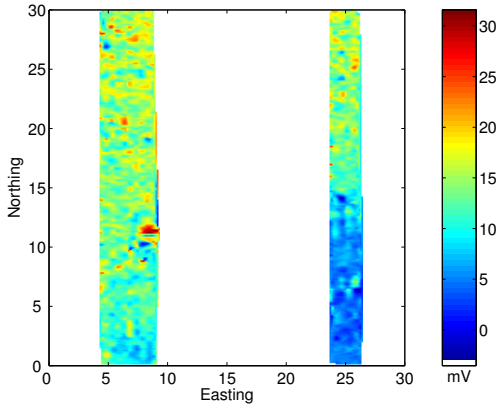

Figure 4.8: Gridded images of channel 1 EM63 data with medium repetition rate collected on part of Navy QA Grid 2E. The grid has been rotated and translated to local co-ordinates.

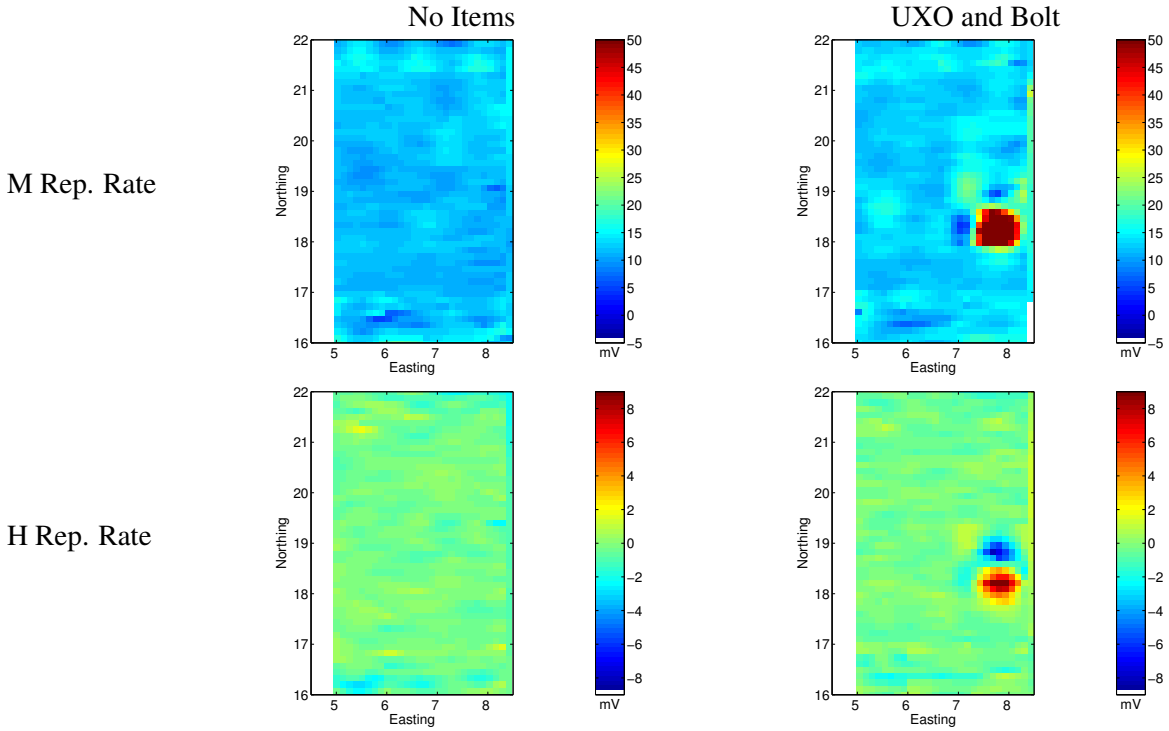

Figure 4.9: Gridded images of channel 1 EM63 data collected on plank grid. Panels on the left show data without any items on the grid and panels on the right show data with a bolt and a 90mm on the grid. The top row of panels show data from the medium repetition rate and the bottom row shows data from the high repetition rate. The grid data has been rotated and translated to local co-ordinates such that 0,0 is the southwest corner of grid 2E.

4.5 Waikoloa

4.5.1 Field experiments

The Waimea GPO was selected as the focus on the Island of Hawaii. This site was selected based on information from American Technology Inc. (ATI) who are performing munitions response operations on the former Waikoloa Maneuver Area. The terrain at Waimea is rolling ranch land that accommodated surveying with a wheeled cart. The other possible site on the Big Island was the Waikoloa GPO; however it is littered with cobble to boulder sized lava rocks that make surveying with a wheeled cart impossible. Since only a single week of field work was planned on the Island of Hawaii only data using the standard EM61 chip and the medium repetition rate of the EM63 were collected over both the seeded and unseeded grids at Waimea. After analyzing the two 30×30m data-sets an 8×30m subset of the seeded grid was selected for additional detailed surveying. Since the background geologic EM signal, and therefore micro-topographic effects, at Waimea were less significant than those observed at Kaho'olawe it was acceptable to lay out string at 1m intervals to maintain adequate positioning. The detailed area of the seeded grid was surveyed with all four of the EM61 chips and both EM63 repetition rates.

An overview of the Waimea GPO area is shown in Figure 4.10.The location of topographic features of interest in the seeded and unseeded grids are shown in Figure 4.11.

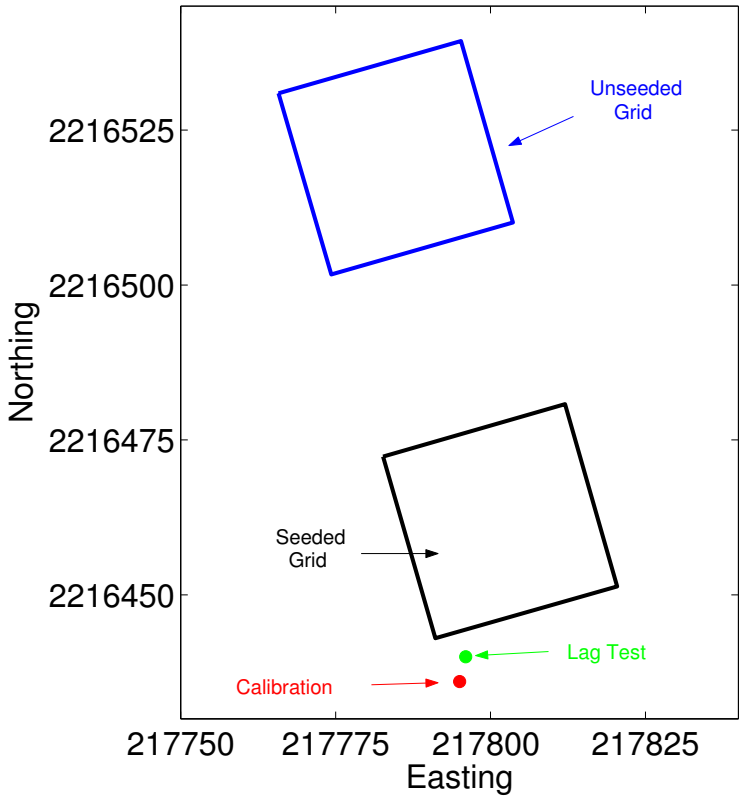

Figure 4.10: Overview of Waimea GPO area. The black polygon shows the outline of the seeded grid, the blue polygon shows the outline of the unseeded grid, the red dot is the location of the calibration measurements, the green dot is the location of the lag test. The coordinates shown are UTM Zone 5, Nad 83 Hawaii.

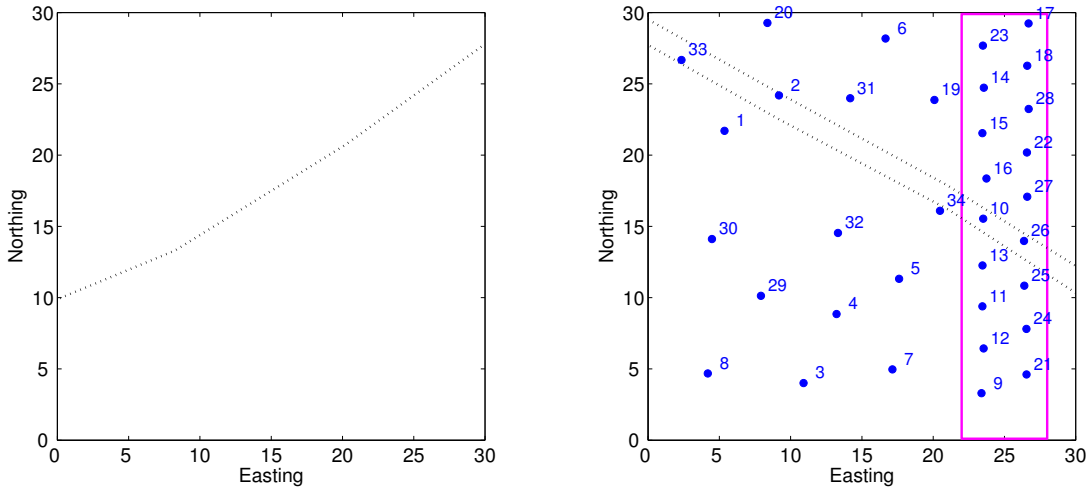

(a) Unseeded Grid

(b) Seeded Grid

Figure 4.11: Features of interest on the unseeded and seeded grids at the Waimea GPO. Panel a) unseeded grid and b) seeded grid. The dashed black lines on each panel represent depressions due to old trails or pathways. The magenta polygon represents the detailed grid and the blue dots represent the location of UXO in the seeded grid. Each grid has been rotated and translated to local co-ordinates such that the southwest corner is located at (0,0).

In general the topographic variation at Waimea is gradual. The depressions associated with the old road and trail shown in Figure 4.11 are visible only due to a lack of grass. The ground truth for the seeded grid was provided by ATI. The description and location of the emplaced UXO at Waimea seeded grid are displayed in Table 4.2.

Due to the rough topography at the Waikoloa GPO EM63 data were collected as a series of static soundings. A total of 36 soundings were collected on the unseeded grid. The sounding were collected at surface sample locations. An overview of the Waikoloa GPO area is shown in Figure 4.12. Since only static sounding data was collected at Waikoloa no lag test was performed.

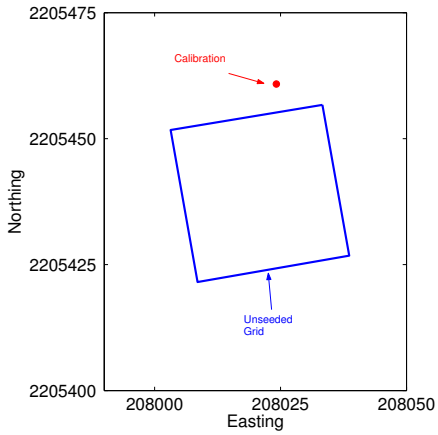

Figure 4.12: Overview of Waikoloa GPO area. The blue polygon shows the outline of the unseeded grid and the red dot is the location of the calibration measurements. The coordinates shown are UTM Zone 5, Nad 83 Hawaii.

Label	Easting	Northing	Local X	Local Y	Item Description	Depth	Inclination
1	217791.15	2216466.06	5.36	21.7	4.2” mortar	0.96	0
2	217794.14	2216469.5	9.18	24.19	105mm HEAT	0.8	0
3	217801.36	2216450.58	10.91	4.01	75mm proj	0.58	15
4	217802.25	2216455.87	13.22	8.85	75mm proj	0.67	6
5	217805.79	2216459.45	17.61	11.32	75mm proj	0.34	3
6	217800.23	2216475.4	16.66	28.18	75mm proj	0.69	-5
7	217807.09	2216453.22	17.14	4.97	2.36” rocket	0.29	30
8	217794.72	2216449.37	4.19	4.68	2.36” rocket	0.56	2
9	217813.55	2216453.34	23.39	3.3	37mm	0.02	0
10	217810.3	2216465.14	23.51	15.54	37mm	0.29	0
11	217811.93	2216459.21	23.45	9.39	37mm	0.18	0
12	217812.83	2216456.4	23.54	6.44	37mm	0.1	0
13	217811.15	2216461.97	23.46	12.26	37mm	0.38	0
14	217807.8	2216473.98	23.55	24.73	37mm	0.1	0
15	217808.58	2216470.89	23.45	21.54	37mm	0.22	0
16	217809.74	2216467.91	23.74	18.36	37mm	0.35	0
17	217809.58	2216479.18	26.69	29.24	smoke grenade	0.28	0
18	217810.31	2216476.3	26.6	26.27	smoke grenade	0.21	0
19	217804.71	2216472.2	20.09	23.87	rifle grenade	0.37	0
20	217791.96	2216474.16	8.37	29.27	rifle grenade	0.25	0
21	217816.23	2216455.47	26.55	4.61	hand grenade (MKII)	0.04	0
22	217811.97	2216470.44	26.58	20.18	hand grenade (MKII)	0.45	0
23	217806.93	2216476.8	23.49	27.68	grenade fuze	0.04	not est.
24	217815.34	2216458.54	26.54	7.81	hand grenade (MKII)	0.13	0
25	217814.36	2216461.41	26.39	10.84	hand grenade (MKII)	0.29	0
26	217813.48	2216464.43	26.37	13.98	hand grenade (MKII)	0.17	0
27	217812.84	2216467.47	26.6	17.08	hand grenade (MKII)	0.37	0
28	217811.24	2216473.42	26.7	23.24	M48 fuze	0.13	not est.
29	217796.8	2216455.64	7.92	10.13	81mm	0.64	10
30	217792.4	2216458.52	4.48	14.11	81mm	0.79	0
31	217799	2216470.69	14.18	23.99	81mm	0.7	0
32	217800.78	2216461.37	13.32	14.54	60mm	0.55	75
33	217786.88	2216470	2.34	26.67	60mm	0.5	0
34	217807.23	2216464.83	20.48	16.09	60mm	0.39	0

Table 4.2: Locations of emplaced UXO from the seeded grid at the Waimea GPO.

4.5.2 Results

Waimea GPO EM61 Data

Data collected using the standard EM61 chip at Waimea are shown in Figure 4.13. The gridded images show that the magnetic soil response at Waimea is smaller than the effect observed at Kaho’olawe. The background variation at Waimea is on the order of 20mV. Since the amplitude of the large scale variations in the data are small it is reasonable that small scale variations will also have small amplitudes. While the Waimea data lacks the high amplitude small scale responses observed at Kaho’olawe, there are some interesting features. Figure 4.11 identified two paths crossing the grids. The path on the seeded grid is the

result of vehicle traffic across the field and the path on the unseeded grid is likely a foot or animal path. Each of these features show up in the gridded data in Figure 4.13 as weak 5-10mV linear features. There are also areas (i.e. the seeded grid within 13 to 17E and 0 to 15N) that contain irregular responses with amplitudes on the order of 5mV.

The responses of the emplaced UXO are clearly shown in the data from the seeded grid. However it is interesting to note the presence of at least five UXO-like anomalies in the unseeded grid. ATI informed us that the area was surface cleared prior to establishing the GPO, however it is possible that there are metallic items within the unseeded grids at Waimea and Waikoloa.

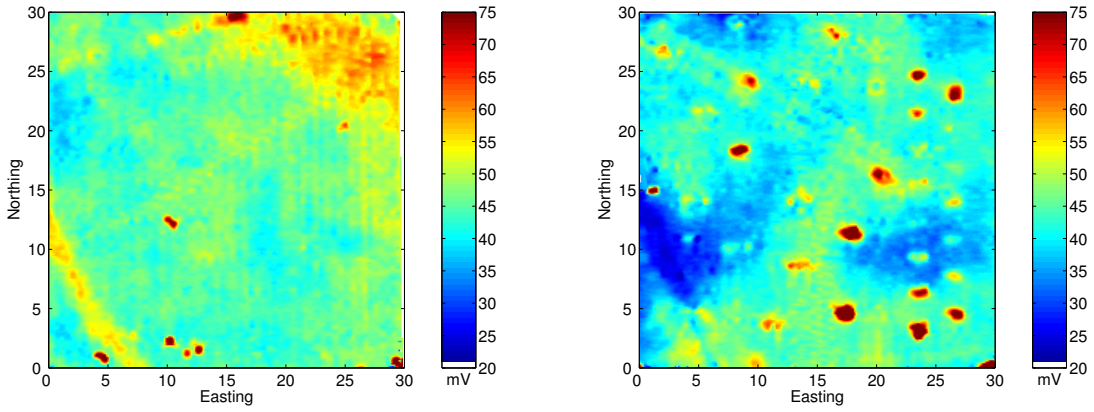

(a) Unseeded Grid (b) Seeded Grid

Figure 4.13: Gridded images of channel 1 EM61 data collected on Waimea GPO using standard EM61 chip. Panel a) unseeded grid and b) seeded grid. The grids have been rotated and translated to local co-ordinates.

Waimea GPO Detailed Grid EM61 Data

The final two lanes at the east edge of the Waimea GPO seeded grid were selected for detailed surveying with the four EM61 chips. This area was selected because it contained a number of UXO and was relatively flat. The decreased background variation attributed to magnetic soil response at Waimea made it acceptable to do away with the plank grid and the detailed surveys were carried out on the ground. The data from the four surveys are shown in Figure 4.14.

Even with minimal processing (lag and drift correction) it is possible to identify at least ten possible UXO targets in each of the data sets. Each of the data sets also display a background soil variation with a low across the grid at approximately 10m N and another low in the NE corner. The data from the 2ms chip contains more noise than the other chips, however it is still possible to identify most of the features visible in the three other data sets.

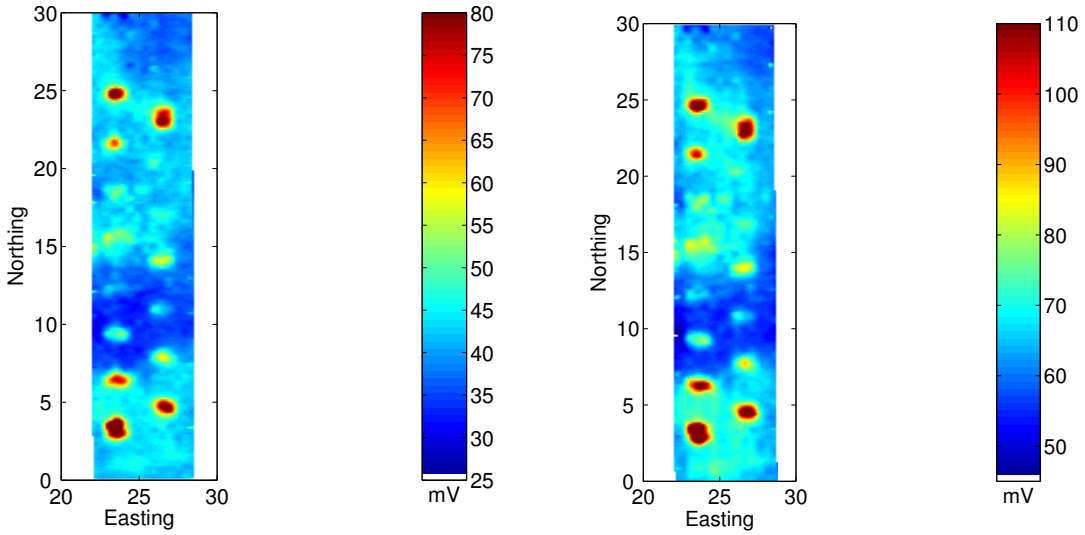

(a) Standard Chip

(b) 10ms Chip

(c) 4ms Chip

(d) 2ms Chip

Figure 4.14: Gridded images of channel 1 EM61 data collected on a section of the Waimea seeded grid using four different transmitter chips. Panel a) standard EM61 chip, b) 10ms chip, c) 4ms chip and d) 2ms chip. The grid has been rotated and translated to local co-ordinates.

Waimea GPO EM63 Data

Medium repetition rate EM63 data was collected over both the unseeded and seeded grids at Waimea. A Gridded image of the first channel data is shown in Figure 4.15. The EM63 data collected at Waimea exhibited the same problems that were observed at Kaho'olawe. The lower amplitude background variations at Waimea resulted in the absence of any regional qualitative information in the data. The gridded data from the unseeded grid is almost completely devoid of large amplitude responses. The dynamic range of the image in Figure 4.15(a) is only 10mV and the instrument noise is dominating most of the gridded data. The few responses that are visible in the southwest corner are associated with the UXO-like items visible in the EM61 data from Figure 4.13(a). Responses from the corner posts of the grid are also visible in the data. The seeded grid data contains more information. The large asymmetric anomalies in Figure 4.15(b) correspond

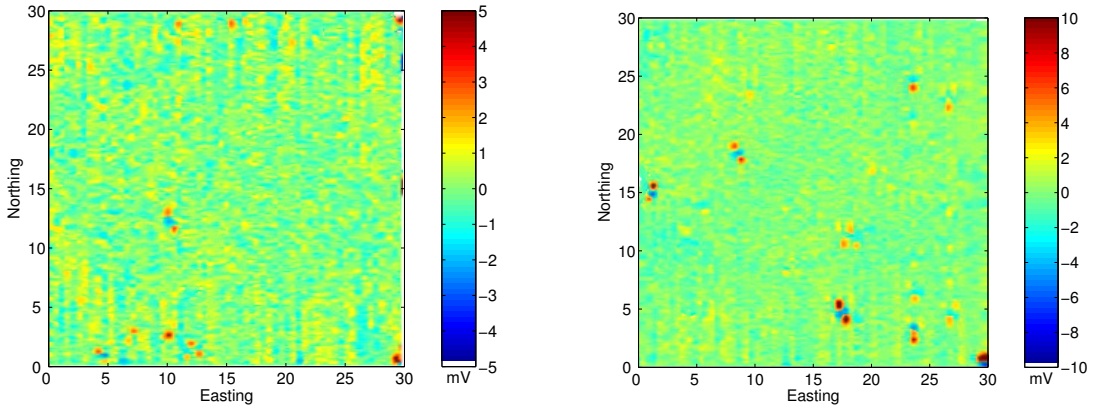

(a) Unseeded Grid (b) Seeded Grid

Figure 4.15: Gridded images of channel 1 EM63 data collected on Waimea GPO using the medium repetition rate. Panel a) unseeded grid and b) seeded grid. The grids have been rotated and translated to local co-ordinates.

to the large amplitude UXO responses from the EM61 data shown in Figure 4.13(b). While the responses in the data suggest the presence of possible UXO targets the data errors preclude its use for any qualitative analysis.

Waimea GPO Detailed Grid EM63 Data

EM63 data collected over the detailed grid at Waimea are shown in Figure 4.16. The results from medium repetition rate over the detailed seeded grid are identical to those described in the previous section and the high repetition rate data contains even less information. The data is much noisier and only two of the responses (3 N,24 E and 25 N,24 E) visible in the medium repetition rate data are detected. Again these results are comparable to the performance of this particular EM63 system on Kaho'olawe.

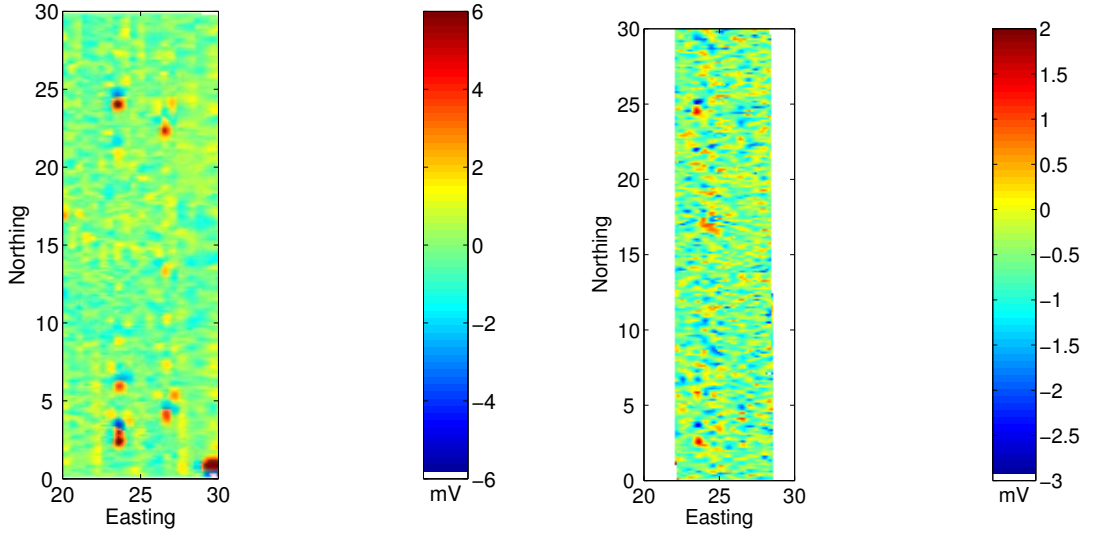

(a) Medium Repetition Rate (b) High repetition rate

Figure 4.16: Gridded images of channel 1 EM63 data collected on a section of the Waimea seeded grid using two different repetition rates. Panel a) medium repetition rate and b) high repetition rate. The grid has been rotated and translated to local co-ordinates.

Waikoloa GPO EM63 Data

The EM63 survey at the Waikoloa GPO consists of 36 static soundings within the unseeded grid. Each of the soundings is located at a pseudo-random location within a 5 x 5m grid cell. These locations were selected for a surface soil sampling program in order to get an unbiased sample of the soil variability across the grid. Since the EM63 data collected at Waikoloa were individual soundings they were not effected by the asymmetries seen in the dynamic survey data from Kaho'olawe and Waimea. The sounding data from each of the locations are plotted in Figure 4.17.

The data shows that the soil response (as detected by the EM63) is not significant. The maximum response is approximately 5mV in the first channel and it does not vary a great deal over the grid. The decay curve does not appear to follow the expected $1/t$ decay, however it is important to note that the amplitude of the measured data is only slightly larger than the noise in the data. The low amplitude response and lack of variation in the data are reinforced by the gridded images of the first and fifth time channels shown in Figure 4.18.

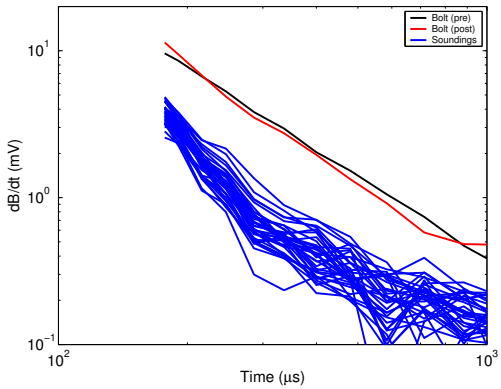

Figure 4.17: Decay curves from soundings at the Waikoloa GPO. The two black curves are from the calibration bolt and the other red curves are from the soundings within the grid. The data were collected with the medium repetition rate.

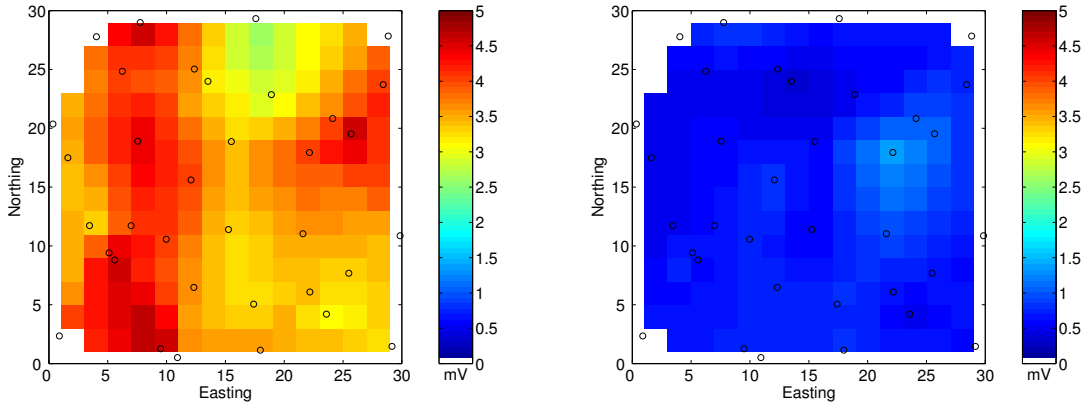

(a) Channel 1: 177 μs

(b) Channel 5: 286 μs

Figure 4.18: Gridded images of EM63 sounding data collected on the unseeded grid at the Waikoloa GPO. Panel a) Channel 1 and b) Channel 5. The data were collected with the medium repetition rate. The grid has been rotated and translated to local co-ordinates.

4.6 Discussion

In summary, EM-61MKII surveys with 4 different transmitter characteristics were collected at both Kaho'olawe Island and the Waikoloa Manoeuver Area. At Kaho'olawe the response from the soil was very large and spatially variable and was compounded by the effects of micro-topography on the measured data. This led us to collect data on planks so that consecutive surveys could be meaningfully compared. The soil response at the Waikoloa Manoeuver Area was significantly smaller than at Kaho'olawe, which allowed the EM-61 data to be collected without resorting to planks.

The EM63 instrument functioned correctly when stationary, which allowed us to collect soundings at a number of points. However, the EM63 instrument did not operate properly when in dynamic mode. Upon conclusion of our data collection, the binary instrument data files collected in dynamic mode were sent to Geonics Ltd. for analysis. Geonics Ltd. were unable to determine the source of the dynamic mode collection problems. No usable data were collected with the PROTEM47. Our intention was to test this instrument prior to data collection. Unfortunately, delays at the Canadian/U.S.A. border prevented us from verifying that the instrument was operational.

In the next chapter, we analyze in more detail the small scale variations evident in the data collected on Kaho'olawe Island. Then in the following chapter, we analyze the data collected with the different EM-61 chips in more detail.

Chapter 5

Challenges encountered in collecting TEM data in magnetic soil environments

In this chapter, we analyze the data collected on Kaho'olawe Island in more detail to demonstrate some of the practical challenges involved with data collection in hostile soil environments. In particular we demonstrate that short wavelength variations in the TEM response are due to micro-topographic variations and coil orientation effects. These effects are significant and can potentially mask UXO and/or result in significant numbers of false positive.

As discussed in Chapter 4, EM61 data were collected over Grid 2E. The gridded image of the response from the first time channel (Figure 5.1)clearly illustrates the large scale (low spatial frequency) variation across the grid. There is a low response area in the southeast corner and a higher response area in the

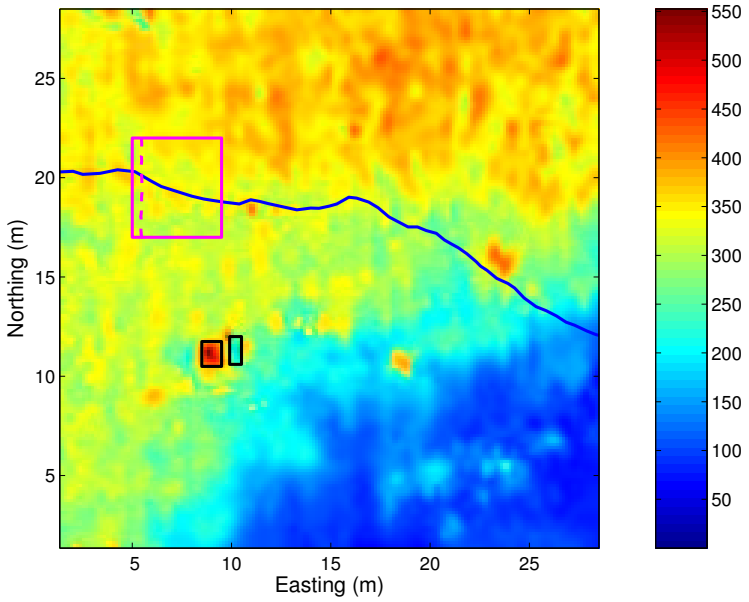

Figure 5.1: Gridded channel 1 EM61 data collected over Grid 2E at the Navy QA Range, Kaho'olawe. Colorbar scale is in mV. The blue line represents the location of the rivulet running through the grid, the black polygons represent the location of a hole and the pile of dirt excavated from the hole, the magenta polygon indicates the location of the plank grid and the dashed magenta line indicates the line of data used for detailed analysis.

north and northwest area of the grid (note that the data have been rotated and translated such that all lines run north-south and the southwest corner of the grid lies at coordinate 0,0). The measurements in the high response area are approximately 300mV greater than the values in the low response area. These data also show evidence of small scale (high spatial frequency) variations in the response (note that all of the QA rounds were removed by the Navy, and therefore there are no known UXO in the Grid 2E).

The two dimensional power spectrum of the data (Figure 5.2) shows that, while the majority of the power is centered at small wave numbers (low frequency), there is significant power at large wave numbers (high frequency). During data collection and quality control it was noticed that some of the high frequency effects correlated well with localized micro-topographic features. The annotations on Figure 5.1 indicate the locations of the more prominent features. The blue line shows the path of a small (approx. 10cm deep) rivulet that crosses the grid. The two black polygons indicate the location of a hole (right polygon) where a QA round was excavated and the pile of soil (left polygon) excavated from the hole. The hole is approximately 19cm deep and the pile is approximately 22cm tall. Photographs of the hole and pile are shown in Figure 5.3. The responses attributed to these features were on the order of 175 mV.

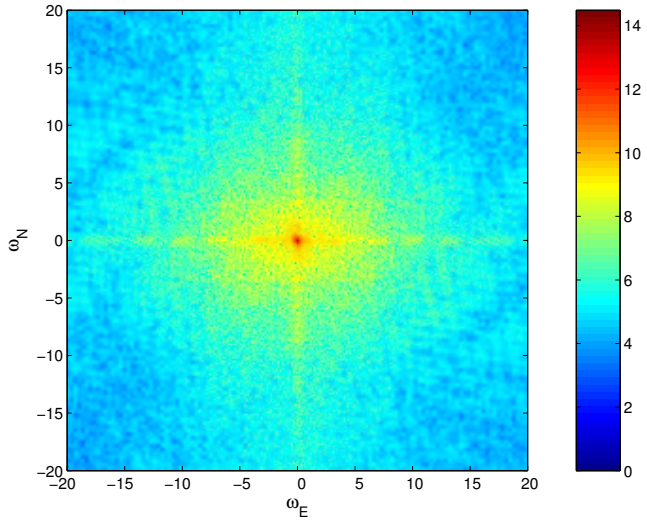

Figure 5.2: Power spectrum of the EM61 data collected over Grid 2E. Colourbar scale is in ln(Power).

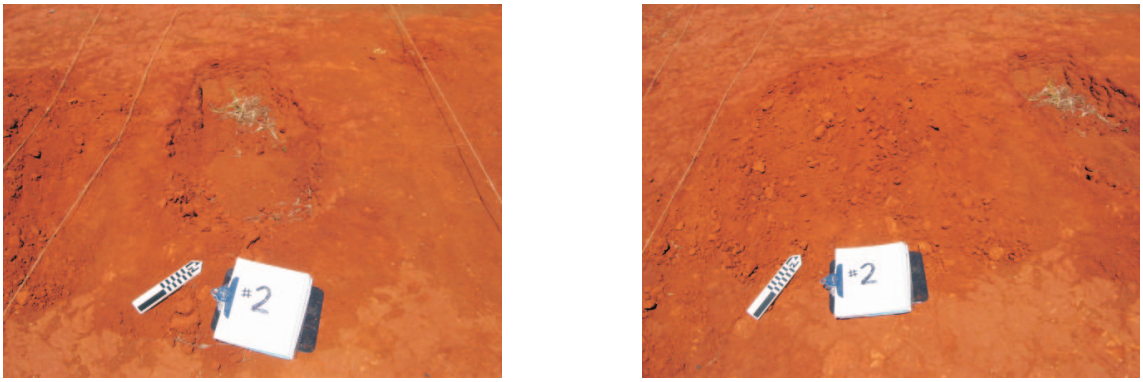

Figure 5.3: Photographs of representative micro-topographic features on Grid 2E. The photo on the left shows a 1.5m by 1.5m, 19cm deep hole and the photo on the right shows a 1m by 1.25m, 22cm tall pile of soil excavated from the hole.

A series of tests were devised to investigate the relationship between micro-topography and coil orientation and to determine the effects on TEM data. Both a coil tilt test and a coil height test were performed in the high response area in order to quantify the effects that may occur during surveying. During the tilt test, data were collected with the coil at a fixed tilt angle as shown in the left panel of Figure 5.4. This was repeated for seven orientations ranging from horizontal to almost vertical (front edge of coil on the ground). The results from the tilt test are shown in the right panel of Figure 5.4. During the height test data were collected with the coil at a fixed height above the ground as shown in the left panel of Figure 5.5.

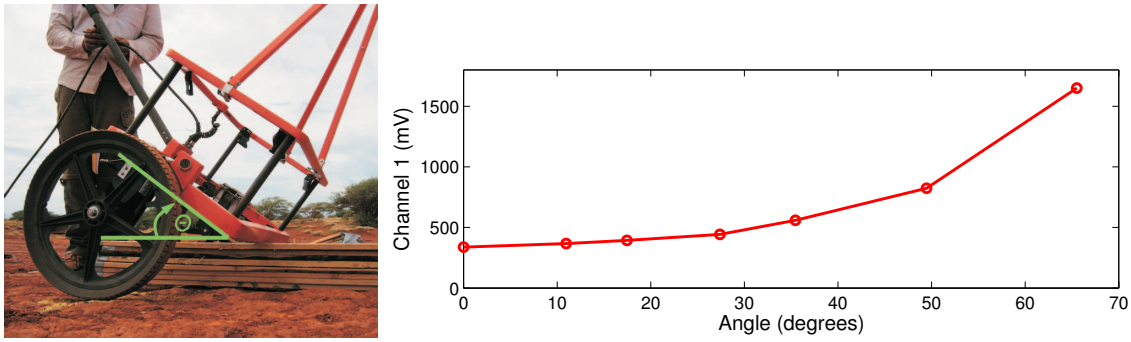

Figure 5.4: Photograph and results from the tilt test. The photo on the left shows the method used for the tilt test, with the tilt angle indicated by θ. The plot on the right shows the results from the tilt test.

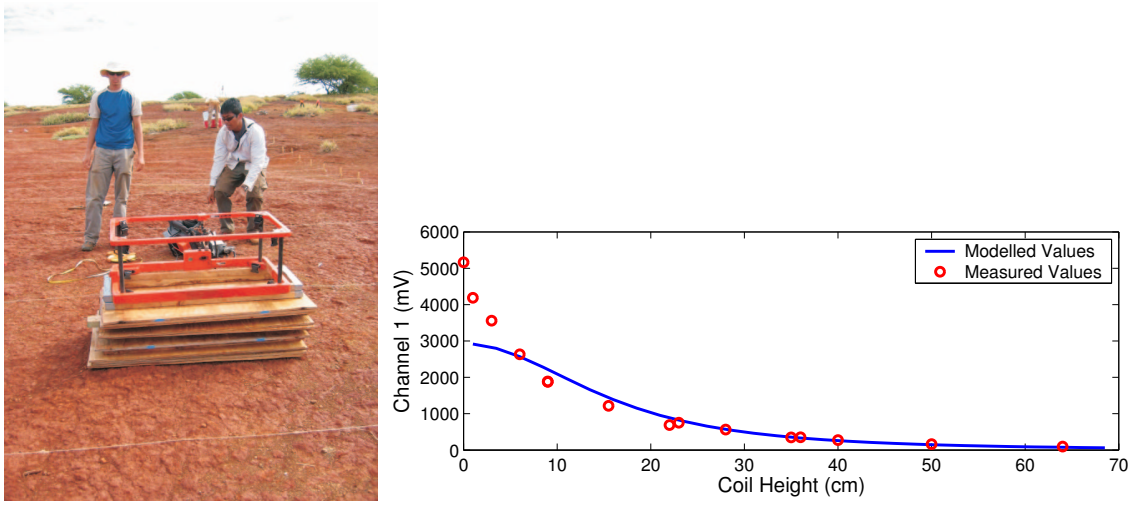

Figure 5.5: Photograph and results from the height test. The photo on the left shows the height test, with the height of the coil indicated by h. The plot on the right shows the results from the height test. The red circles represent values measured during the test and the blue line represents the modelled values.

This was repeated for eleven heights ranging from 0 to 64cm. The results from the height test are plotted with modelling results in the right panel of Figure 5.5. In order to model the height test measurements we calculated the frequency domain field at the center of a loop located at a given height h above a half-space with a frequency dependent susceptibility χ defined as

$$\chi = \chi_o \left[1 - \frac{1}{\ln\left(\tau_2/\tau_1\right)} \ln\left(\frac{i\omega\tau_2 + 1}{i\omega\tau_1 + 1} \right) \right] \tag{5.1}$$

where ω is the frequency, χ_o is the static ($\omega = 0$) susceptibility and τ_1 and τ_2 are the two time constants that

determine the limits of the uniform distribution of time constants. For our modelling we used $\chi_o = 0.1$ SI, $\tau_1 = 10^{-6}$ s, $\tau_2 = 10^6$ s and a half-space conductivity of $\sigma = 10^{-3}$ S/m. The field was evaluated over a range of frequencies and transformed to the time domain using the Fourier transformations of the frequency response for a causal step turn-off (Newman et al., 1986). The curve in Figure 5.5 shows that the modelled response diverges from the measured response when the height is less than 10cm. This discrepancy may be due to the fact that the response of the coil is being approximated using the field at the center of the loop as opposed to explicitly integrating the field around the path of loop.

The results from both tests illustrate that in magnetic soil environments even small changes in coil orientation and the distance between the coil and the surface can result in significant amplitude variations. The tilt test showed that as the tilt angle of instrument increases, which effectively decreases the distance between the effective area of the coil and the ground, the amplitude of the TEM response increases. By tilting the coil 10 degrees forward the amplitude increased by approximately 29mV. The height test showed that very small variations in the height of the coil can result in large changes in amplitude. For example, when the coil was positioned at 36cm instead of the normal survey height of 40cm, the amplitude increased by approximately 77mV. During production UXO EMI surveys tilt variations on the order of 10 degrees and height variations on the order of 4cm are commonplace. Therefore, it is likely that micro-topographic effects will be a source of high frequency response/noise in EMI data collected in magnetic soil environments.

5.1 Analysis of micro-topographic effects

In order to investigate these effects further, we created a platform to collect data free from coil orientation errors within the high response area. We laid out a grid of planks along the tracks where the tires of the EM61 would traverse. The location of the grid is represented by the magenta polygon in Figure 5.1 and photographs of the grid are shown in Figure 4.5. By collecting EM61 data on a smooth plank grid it was possible to eliminate any sudden changes of tilt. For the purpose of comparison, data were collected on the ground as well. Great care was taken to ensure that the paths of the two surveys were as similar as possible. Elevation data, both on the planks and on the ground, were collected in order to quantify coil height effects.

The analysis concentrated on a single line of data from the plank grid shown as a dashed line in Figure 5.1. Profiles of the data collected on the planks and on the ground are shown in Figure 5.6. The data collected on the ground contain high frequency, large amplitude responses which are completely absent from the plank data. For the majority of the line the plank data is smoothly varying and has a lower amplitude than the ground data. At the north end of the line (approximately 21.5m N) the plank data goes through a rapid 55mV increase in amplitude. After this point the amplitude and shape of the plank data is similar to that of the ground data. This change occurred as the EM61 rolled off the end of the plank grid and experienced a decrease in coil height from approximately 42 to 40cm and likely tilted forward. Based on the results of the height and tilt tests these changes in coil orientation can easily account for a 55mV increase in amplitude.

The elevation difference between the ground and planks plotted in Figure 5.7 shows a strong correlation between the smooth variations in the plank data and the coil height. The 50mV decrease in amplitude in the plank data located at the center of the line correlates well with the 10cm deep rivulet. This is expected since the distance between the coil and the ground gradually increases and then decreases as the EM61 traverses the rivulet. There is also a distinct feature in the data collected without that planks at this point. The channel 1 response goes through a very sharp high-low-high change with an amplitude of approximately 60mV. Since the rivulet is not perpendicular to the line a possible cause of this response is the EM61 wheels getting stuck in the rivulet one after the other. As surveying took place the left wheel would have gone into the rivulet first bringing the coil closer to ground and likely tilting it as well. This would have caused an increase in amplitude. Then the wheel would have come out of the rivulet and left the coil straddling the rivulet, increasing the coil height and causing a decrease in amplitude. Then the right wheel would have

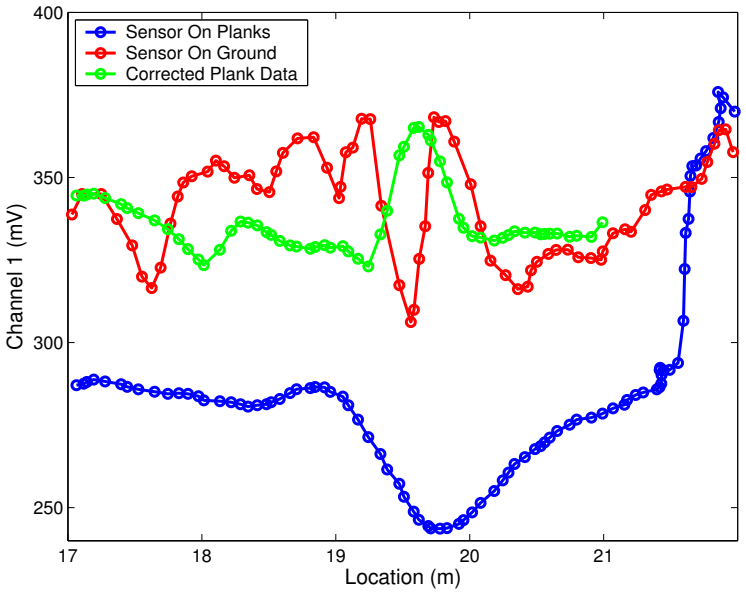

Figure 5.6: Data collected along Line 2 of the plank grid (shown as a magenta dashed line in Figure 5.1). The blue line with circles is the data collected on the planks, red line with circles is the data collected on the ground and the green line with circles is the height corrected plank data. The rivulet is located at approximately 19.8m N and the end of the planks is located at approximately 21.5m N.

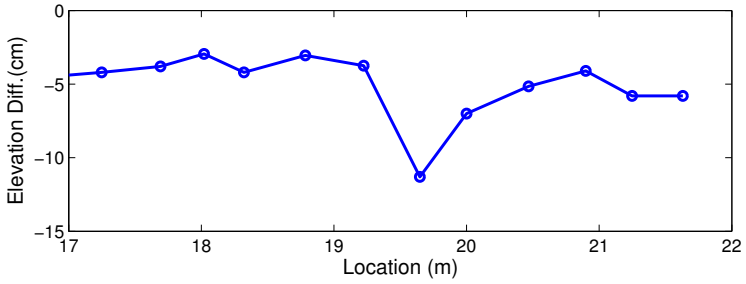

Figure 5.7: Measured elevation difference between the ground and the planks.

gone into the rivulet causing a second increase in amplitude. While both datasets contain coil orientation effects in the vicinity of the rivulet, the fact that coil orientation was not measured during the surveys means its only possible to correct for the height variations in the plank data.

The modelling results from the height test were used to calculate a correction factor to apply to the plank data in order to effectively lower the coil to the same level as the ground data. At each measurement location along the line the half space response, d, was calculated for the nominal coil height, $h_{nom} = 40$cm, and for the actual height, h_{true}, of the coil during the survey. The correction factor, δd, was calculated as

$$\delta d = d(h_{nom}) - d(h_{true}), \tag{5.2}$$

and was added to each measurement from the plank data. The corrected plank data plotted in Figure 5.6 is similar in amplitude to the ground data. The corrected plank data contains more high frequency variation than the plank data however the variation does not appear to be as extreme as in the ground data. The anomaly observed about the rivulet in the height corrected data is most likely an artifact of the correction procedure. The correction procedure uses a halfspace whereas the true earth has a variable topography. As such the decrease in signal will be over-estimated. We can consider the correction being applied above a narrow channel. The height correction for an observation directly over the channel is independent of the width of the channel, however the actual disturbance in the EM signal caused by the channel will approach zero as the width of the channel goes to zero. Therefore, we should expect an overcorrection that correlates with the topography, similar to what we see in the corrected plank data.

5.2 Discussion

EMI data collected in hostile soil environments will exhibit considerable high frequency spatial variations that may be incorrectly interpreted as potential UXO. These high frequency variations can arise from spatial variability of soils but also from micro-topography. The micro-topography creates two problems in the data. The first is a variation in the sensor-ground geometry that can considerably modify the soil response. The second is through its effect on the sensor orientation. This second problem could potentially be minimized by collection of sensor orientation data. However, even with this orientation information the first problem will remain. In fact, we believe that direct correction for the micro-topography will be infeasible (except in the simplest of scenarios).

As we touched upon in Chapter 3, the micro-topography and any small scale changes in soil properties will create problems for any differential measurement that makes assumptions about the spatial distributions of soil properties (e.g. differential measurements between receivers at different heights). This is a compelling reason to aim to exploit differential measurements that are independent of the spatial distribution of the soil. The next chapter aims to achieve this by developing and exploiting soil models for transmitters with different charge times.

Chapter 6

Detailed analysis of differential illumination measurements

6.1 Introduction

In this chapter, we study the effectiveness of varying the transmitter waveform characteristics applied to an EM61-MK2 sensor. This study is motivated by several practical and theoretical reasons. Although the Minelabs F14A sensor is effective in detecting small targets in a VRM soil setting, it has problems seeing larger deep targets. In addition, it is difficult to perform advanced processing, in particular inversion, on Minelabs F14A data due to proprietary on-board data processing. Decay curve comparisons using a Geonics EM63 sensor may be possible in principle, but is difficult to use in many realistic field settings due to its large weight on a wheeled cart platform. The EM61-MK2 is the most common EM tool used in current munitions response. It has a greater depth of investigation than the Minelabs F14A, and is a much lighter, field ready alternative to the EM63. In addition, our analysis in Chapter 2 showed that the time-decay of certain UXO's can be indistinguishable from magnetic soil. Although the EM61-MK2 only has four channels, the addition of multiple pulse widths provides additional data that will enhance the differences between a metal target decay and a soil decay. We study soil and metal TEM responses and show how these responses differ as a function of the transmitter waveform. We investigate how size variations in the buried metal targets affect the effectiveness of the differential illumination technique.

6.2 The TEM Response of VRM soils and Metallic Objects

Our analysis in Chapter 2 showed that rate of change of the secondary magnetic field due to a VRM soil with a collection of grains with time constants distributed log-uniformally between τ_1 and τ_2 is

$$\frac{\partial M}{\partial t} \propto \frac{-H\chi_o}{\log\left(\tau_2/\tau_1\right)}\frac{1}{t} \tag{6.1}$$

The theory of the TEM response of metal targets is well understood. Similar to the response of VRM soils, the response of a compact metal target can be expressed as a function of time constants. Kaufman (1994) derived a general form for the field caused by currents induced in a confined conductor. By assuming quasi-static fields, the secondary field produced by currents in a confined conductor can be written as

$$H_{\hat{\mathbf{l}}}\left(t,p\right) = \left(\mathbf{H}^P \cdot \hat{\mathbf{l}}\right) \sum_{n=1}^{\infty} d_{n\hat{\mathbf{l}}}\left(p\right) \exp\left(\frac{-t}{\tau_n}\right) \tag{6.2}$$

where $H_{\hat{1}}(t,p)$ is the secondary field in the $\hat{1}$ direction, observed at a point p, and at a time t following the termination of the primary field. The coefficients $d_{n\hat{1}}(p)$ depend on the target location, size and shape, and upon the geometry of the primary field. The time constants τ_n are also dependent on the permeability, size and shape of the target, but not the target location and geometry of the primary field. The largest time constant, τ_1, determines the onset of the late time, exponential stage of the decay and is referred to as the diffusion time constant of the conductor. The form of the time constant is $\tau_1 = L^2\mu\sigma/\pi^2$ where L is a target diameter, μ is the target's magnetic permeability, and σ is the target conductivity. Prior to the late time stage, the cumulative effect of the summed exponentials produces a power law decay. The power law behavior has been verified experimentally and theoretically. Measurements have shown that a combination of a power law and exponential, $V(t) = kt^{-\beta}exp(-t/\tau)$, can be used to model the decay observed within the time range of the Geonics EM63 sensor (Pasion and Oldenburg, 2001). The power law exponent β is a function of the shape of the target, and we have observed β values ranging from 1/2 to 3/2 for metallic targets.

Equation 6.2 for the response of a metallic object assumes a step-off transmitter field. For an arbitrary waveform $g(t)$ that turns off at time $t = 0$, the measured response is obtained by convolution of the waveform with the impulse response

$$\frac{\partial H(t)}{\partial t} = \int_{-\infty}^{0} g(t') \frac{\partial H^I(t-t')}{\partial t} dt' \tag{6.3}$$

where $\partial H^I(t)/\partial t$ is the time derivative of the impulse response. Recall that in Chapter 3 we derived the response of VRM soil to an arbitrary waveform and a general expression was presented in Equation 3.30. The particular characteristics of the four EM-61 waveforms we studied in this project are given in Figure 4.1.

Figure 6.1 illustrates how the transmitter waveforms described in Figure 4.1 alters the $V(t) = 1/t$ step-off soil response and the $V(t) = kt^{-\beta}exp(-t/\tau)$ step-off metallic target response. For this example, the metallic response is calculated using time constants of $\tau = 0.1$, 1, and 10ms, and a power law with $\beta = 1/2$. In evaluating (6.3) we differentiate $V(t)$ to get the impulse response. In order to compare the changing decay characteristics due to the different waveforms, the metal and soil responses are normalized to unity at 1ms.

Figure 6.1 indicates that a target's time constant size, relative to the transmitter on-time, controls how the target decay varies with the length of transmitter on-times. Targets with small time constants are less sensitive to changes in transmitter on-time. The target with $\tau = 0.1$ms has the same decay for each waveform since the transmitter on-times for each waveform is greater than 0.1ms. Targets with larger time constants demonstrate increased sensitivity to the changes in on-time. The response of VRM soil response is also sensitive to the changes in transmitter on-time since the VRM soil response is due to a collection of magnetic grains with a log-uniform distribution of time constants.

The smaller change of the TEM response for short time constant targets illuminated by different on-times compared to the larger changes in the soil response, suggests that variable waveform instrument responses could be effective for detecting small targets in a magnetic soil background. However, time constants for steel targets are large relative to the transmitter on-times that we are considering. For example, due to the large magnetic permeability of steel ($> 200\mu_o$), a steel sphere with a diameter of 5cm has a time constant of 40ms.

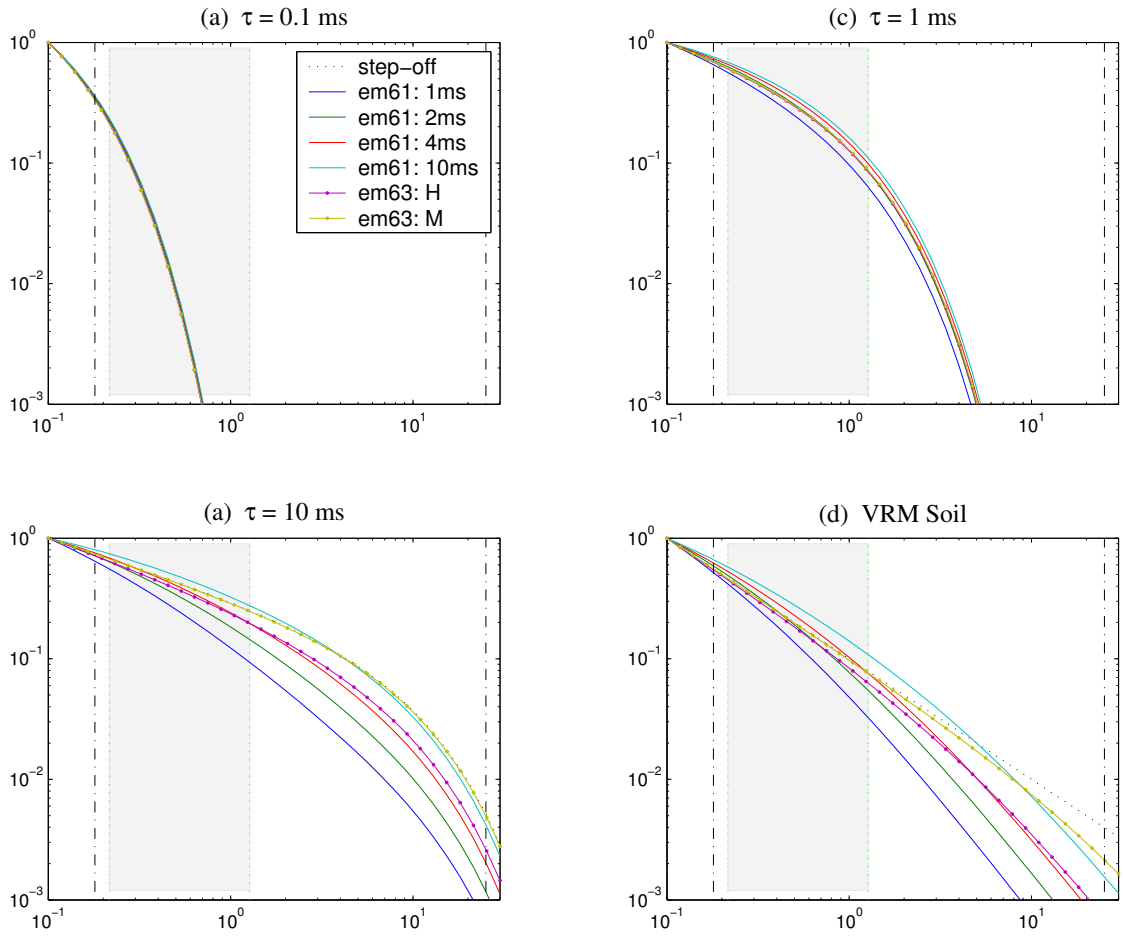

Figure 6.1: The effect of different waveforms on different time constant targets. The grey area represents the measurement range of the standard EM61Mk2 TEM sensor.

6.3 Soil Compensation Processing Applied to Variable Transmitter Waveform TEM Data

6.3.1 Soil Model Fitting

Fitting measured data to a soil model is a simple way of determining which soundings are background responses and which soundings have a contribution from the presence of a metal body. If the observed sounding can be well fit with the response of the soil, then the measured response is likely from the background soil only. If we assume that the magnitude of the soil and metal target responses are independent, we can write the measured sounding from a particular chip as $V(t) = \alpha S(t) + T(t)$, where $V(t)$ is the observed decay, $S(t)$ is the characteristic soil response, and $T(t)$ is the response due to a metal target. The coefficient α is included because any observed soil response will be a multiplicative factor of $S(t)$. Since the coefficient α is a function of the soil characteristics, it is independent of the sensor characteristics (i.e. it will be the same for all chips).

There are two potential problems in fitting a soil model and analyzing a data misfit. Firstly, if the background soil response $\alpha S(t)$ is large relative to the target response, then there is a potential of obtaining a good fit to the data. In order to avoid this problem, an estimated soil response is subtracted from the data prior to fitting. A second potential problem would be if the decay of $T(t)$ is similar to the soil decay. We noted earlier that the variable waveform has the potential to alleviate this problem, but this would not be possible here due to the transmitter waveforms used in this study and the size of targets that can be detected by our sensor. However, the hope is that sampling 4 points of the decay curve will be sufficient in observing differences in soil and metal decays.

The fitting of the soil model represents the simplest of inverse problems: determine a single parameter by fitting multiple data. We define data vector where the TEM decays are normalized by the first time channel:

$$\mathbf{d} = \left[\tilde{V}^i(t_j)\right], \tag{6.4}$$

where $\tilde{V}^i(t_j) = Vi(t_j)/Vi(t_1)$ for time channels $j = 1..4$, and $i = 1, 2, 3$ representing data from the 2, 4, and 10ms waveforms. We fit the data vector with a normalized soil model, with elements $\tilde{S}^i(t_j)$, multiplied by a parameter β. A coefficient β is determined by dividing the data vector by the soil model element by element, and then taking the median of the quotients. To quantify the fit we use a least squares measure of the misfit

$$\text{misfit} = \frac{1}{4N}\sum_{i=1}^{N}\sum_{j=1}^{4}\left[\tilde{V}^i(t_j) - \beta\tilde{S}^i(t_j)\right]^2 \tag{6.5}$$

where $N = 3$ if we use all of the three different chips for fitting.

6.3.2 Differential Analysis

As we saw in Figure 6.1, short time constant targets have a small change in response with different on-times, while the large time constant targets and VRM soil have a large change in response with different on-times. Soil fitting does not attempt to take advantage of this differential effect. Soil fitting uses measurements from additional waveforms only as extra data when calculating the misfit to the characteristic VRM response. An example of a procedure that uses the differential effect for reducing soil anomalies is:

1. Measure the TEM response from one waveform.

2. Assume the measured response is from soil, then use the measured response to predict the response from a waveform with a different on-time.

3. Compare the predicted response with the observed response. If the observed response matches well with the predicted response, then the sounding is likely from soil.

The success of this procedure depends entirely on the time constant of the target. Short time constant targets would have the largest misfit between the observed data (which would have a small differential effect) and the predicted data (which would model the data as having the large differential effect of soil). However, relative to our measurement times, most targets of interest would have a large time constant that would make the differential effect minimal.

This technique is difficult to implement with our equipment due to the sensitivity of the signal to the relative position between sensor and the ground and our need to perform different surveys for each different waveform. It is impossible to ensure perfectly repeatable sensor position and orientation. The changes in sensor position and orientation would produce changes in data amplitude, and compromise our ability to model the data. However, we should point out that we are, at this point, only conducting a feasibility study whereby the differential measurements are collected on consecutive passes. Ideally, the data would all be collected in a single pass by varying the transmitter characteristics on neighboring measurements.

6.3.3 Kaho'olawe Island Navy QA Grid Data

In the last chapter we demonstrated that small sensor movements produced large changes in the measured voltage in the hostile soil environment of Kaho'olawe Island. In order to compare relative differences in signal due to transmitter waveform changes, we needed to minimize changes in sensor location and orientation when repeating measurements with different chips. For single soundings, marks were painted on the ground for accurate placement of the sensor. To replicate a multiple line grid survey, we placed wooden planks on the ground to provide an easily repeatable wheel path for the EM61MK2 cart (Figure 4.5). The planks also minimized sensor orientation changes due to topographic variations.

Differences in line paths over successive surveys were within a few centimeters. The data from the different chips surveys were linearly interpolated to the same station locations.

Two sets of data were acquired at the Navy QA grid on Kaho'olawe. The first set was collected along the planks with each of the 10, 4, and 2ms chips (Figures 6.2(a)-(c)).

This background measurement show the large background signal due to the soil and the large variations in signal simply due to the topography within the survey area. The surveys were then repeated with a small nut (Figure 6.3(a)) placed on the surface at $(X, Y) = (0.56, 2.32)$m and a 90mm projectile (Figure 6.3(b)) placed on the surface at $(X, Y) = (2.92, 1.81)$m (Figures 6.2(d)-(f)). Since the 90 mm target was placed on the surface, its anomaly dominates the gridded data.

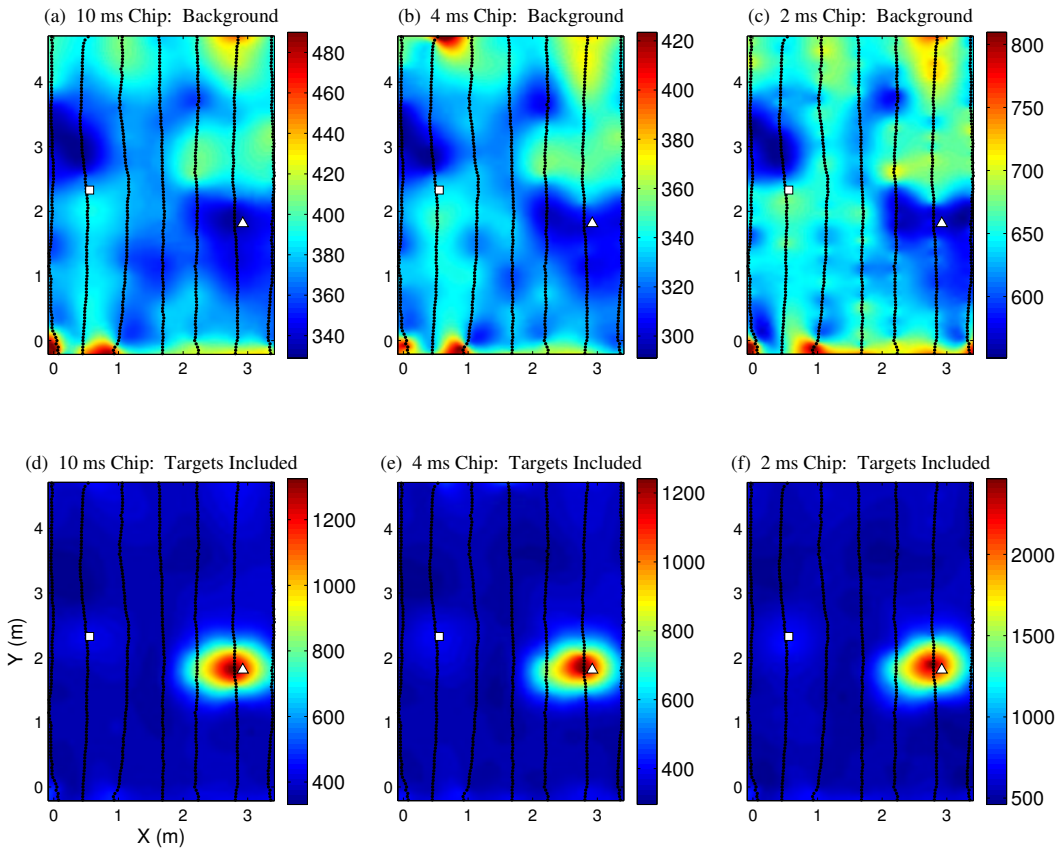

Figure 6.2: The first channel of TEM data interpolated to common locations. The steel nut and 90mm projectile locations are indicated by the '□' and '△' symbols, respectively.

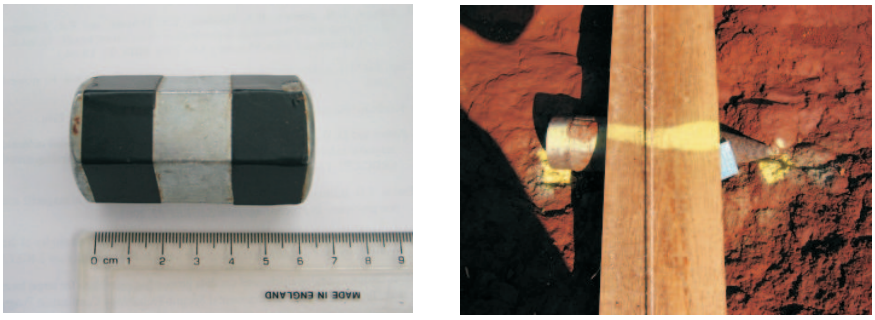

(a) Photo of steel nut (b) Photo of 90 mm UXO

Figure 6.3: Targets measured in plank survey. (a) Photo of the steel nut placed on the surface. (b) Photo of the 90mm projectile placed on the surface.

Soil Fitting Results

Figures 6.4 to 6.6 plots the soil modelling misfit on the data with, and without, metal targets placed on the surface.

We compare fitting results using (1) data from the 10ms chip only, (2) data from the 10ms and the 4ms chip, and (3) data from the 10 ms, 4ms, and 2ms chips to fit the soil model. Regardless of how many chips we use in the fitting, the misfit provides a clear indicator of the presence of metal targets. Although we would expect that using data from all the chips would best detect the metal targets, the higher noise levels of the 2ms chip degrades the performance when using all the chips.

Figure 6.5 compares the characteristic soil model with soundings recorded with and without a metal target present, at the location of the bolt and the location of the 90mm.

The observed soundings of the background soil (Figure 6.5(a) and (b)) fits the 10ms and 4ms data quite well, but the noise level of the 2ms data makes it difficult to fit. The inability to fit the observed decay with a soil model is clear when a metal target is present.

An indication of potential advantages of using soil model fitting rather than raw data for detection can be obtained by looking at line profiles. Figure 6.6 compares the misfit calculated along the second line of data ($X \approx 0.5$).

The red lines indicate data with the bolt present and the blue lines are fit without the bolt. Panel (a) contains the raw data. The large jump in amplitude at the beginning and end of each line is due to the EM61MK2 cart rolling onto and off of the planks. The dip in amplitude at approximately $Y = 3$m is due to a small rivulet. Panels (b) to (c) plot the misfit along the line. The steel bolt appears clearly, even when including the noisy 2ms data in the fitting procedure. The misfit plots are insensitive to the changes in the raw data due to topography. Figure 6.7 plots the data from the 4ms chip and the misfit using the 10ms and 4ms data. The misfit is shown on a scale similar to figure 6.6. The large variation due to topography is not reflected in the misfit plot. This emphasizes the utility of the misfit as a means of reducing the amount of geologic anomalies chosen as potential targets.

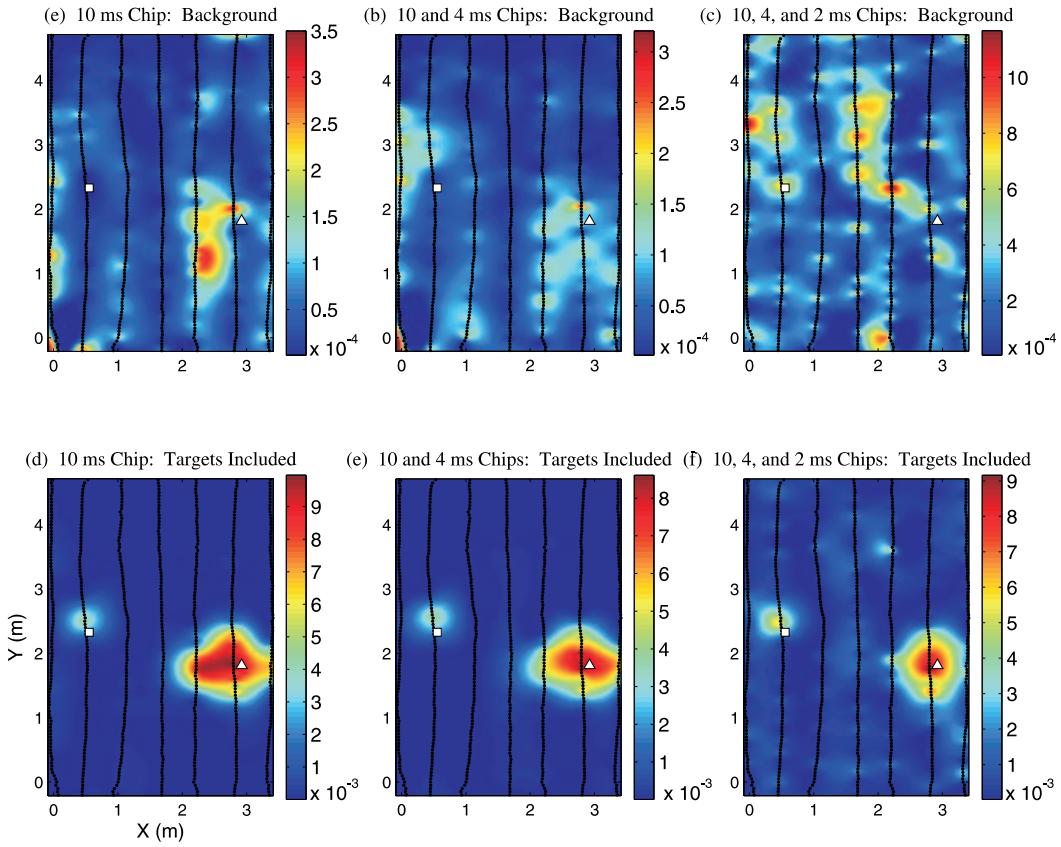

Figure 6.4: Misfit comparison.

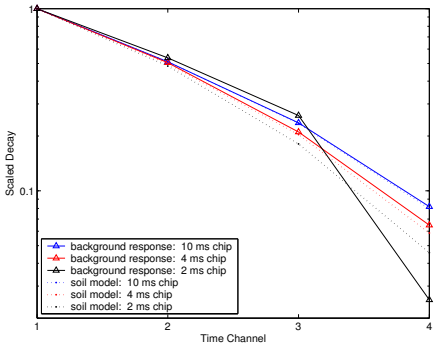

(a) Soil decay at the nut location

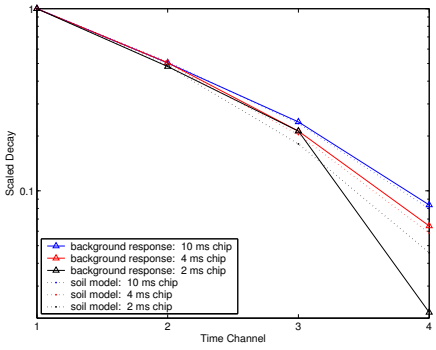

(b) Soil decay at the 90mm location

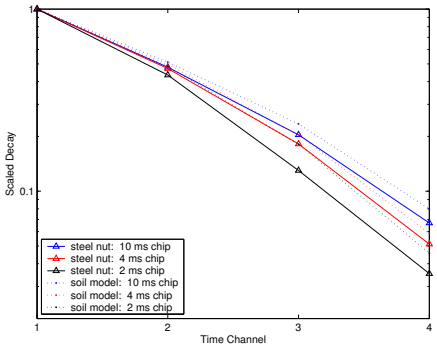

(c) Soil and nut decay comparison

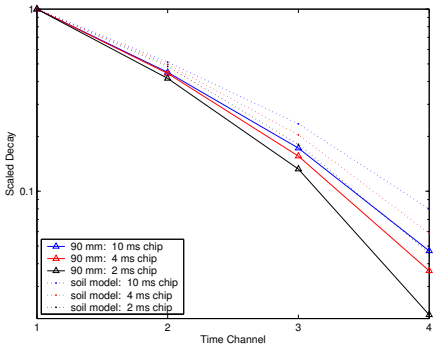

(d) Soil and 90mm decay comparison

Figure 6.5: Decay comparisons.

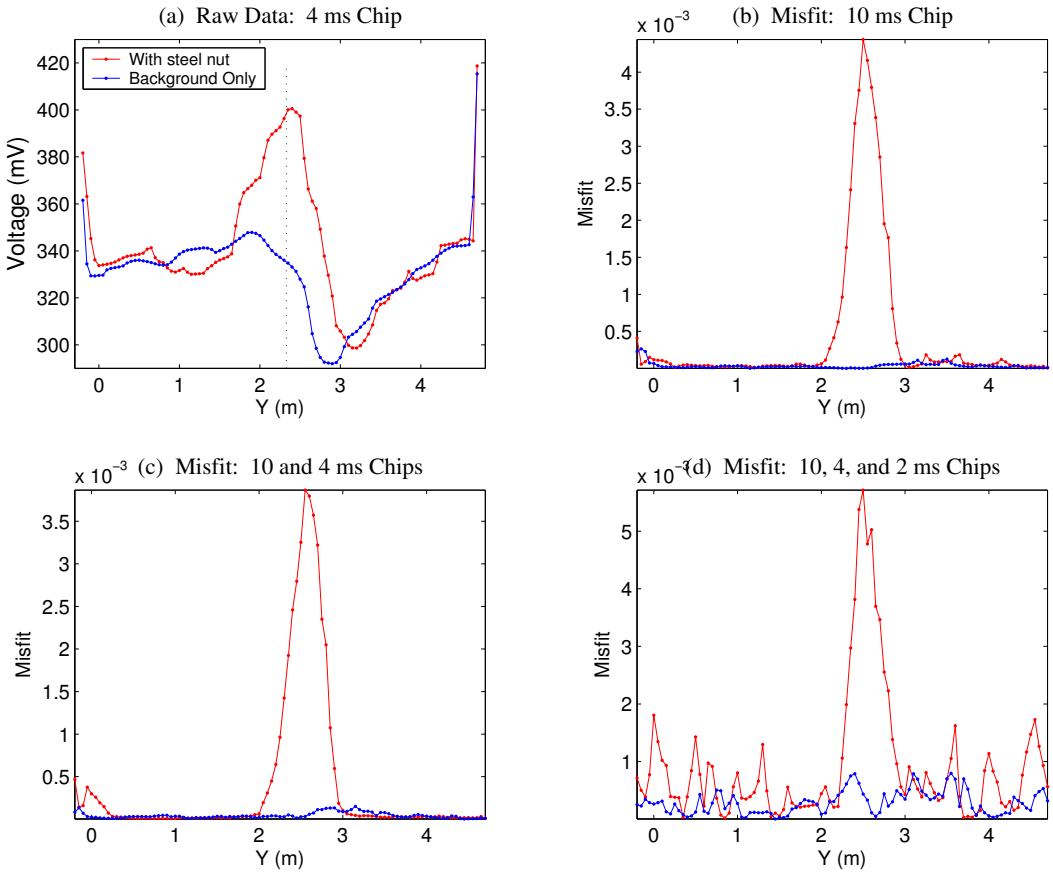

Figure 6.6: Line 2 misfit comparison.

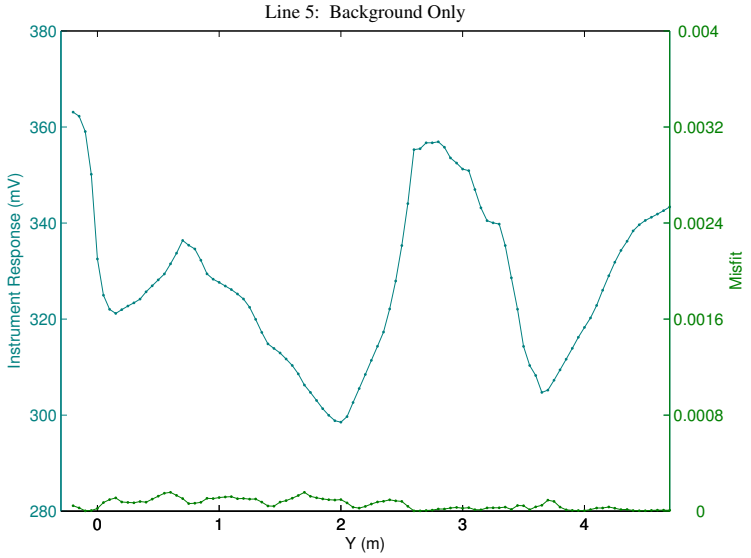

Figure 6.7: Line 5 signal/misfit comparison.

Differential Analysis Results

The procedure outlined in Section 6.3.2 was applied to data collected on the planks. The data collected with the 10ms chip was used to predict the data from the 4 and 2 ms chips. Figures 6.8 and 6.9 compare the observed data (left column), predicted data (middle column), and residual (right column) for data collected with the 4ms over the planks with no targets emplaced. The residual is defined as

$$R\left(t_j\right) = \log\left(V^{obs}\left(t_j\right)\right) - \log\left(V^{pred}\left(t_j\right)\right) \tag{6.6}$$

where $j = 1..4$ represents the time channel. The 4ms and 2ms data predicted from the 10ms data closely matches the measured data when there is only soil response (no metal targets). The observed 2ms data are much noisier than the predicted 2ms data since the 10ms chip is less noisy than the 2ms chip.

The comparison of the predicted and observed data when metal targets are emplaced is shown in Figures 6.10 and 6.11. The 4 and 2ms data are again accurately predicted by the 10ms chip data, indicating that there is little observed differential effect. Figures 6.12 and 6.13 clearly demonstrates this by comparing the predicted and observed data along the lines containing the emplaced bolt and UXO.

The observed and predicted decays directly over the bolt and UXO (Figure 6.14) are nearly the same, indicated that the soil and targets had the same change in response to the different waveforms.

The difference between predicted and observed data is quantified by a misfit function:

$$\text{misfit} = \frac{1}{4}\sum_{j=1}^{4}\left[\log\left(V^{obs}\left(t_j\right)\right) - \log\left(V^{pred}\left(t_j\right)\right)\right]^2 \tag{6.7}$$

The logarithm of the data in used order to account for the (potentially) large change in magnitude in a single decay. Figure 6.15 plots the misfit for the 4ms and 2ms chip data both with and without the emplaced targets. The nut does not produce an anomaly in the gridded misfit, and the UXO does not produce a distinct anomaly in the gridded misfit. We conclude that there is minimal differential effect recorded in the data.

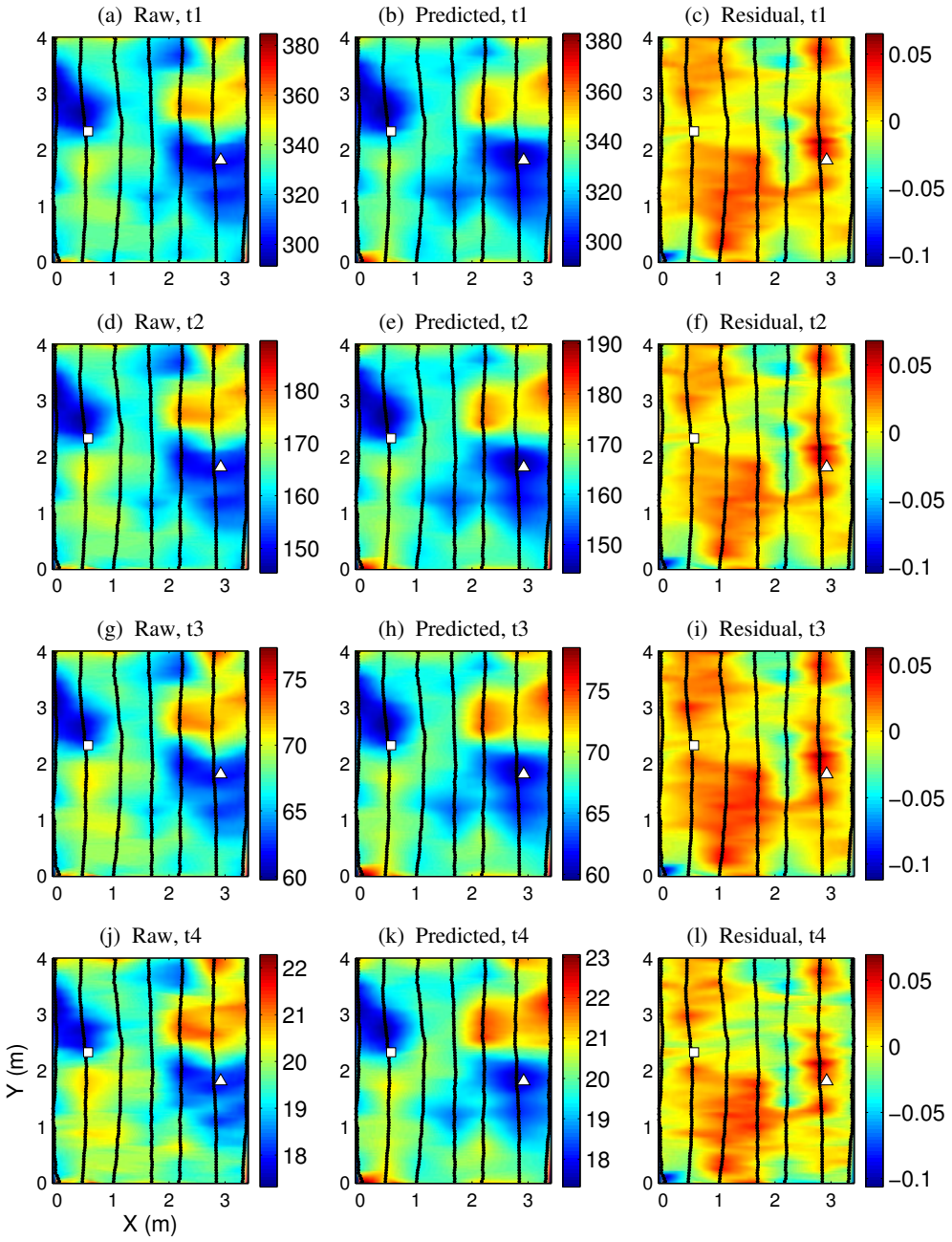

Figure 6.8: Comparison of 4ms chip raw data and the 4ms data predicted from the 10ms chip data. The bolt and UXO are not present for this data.

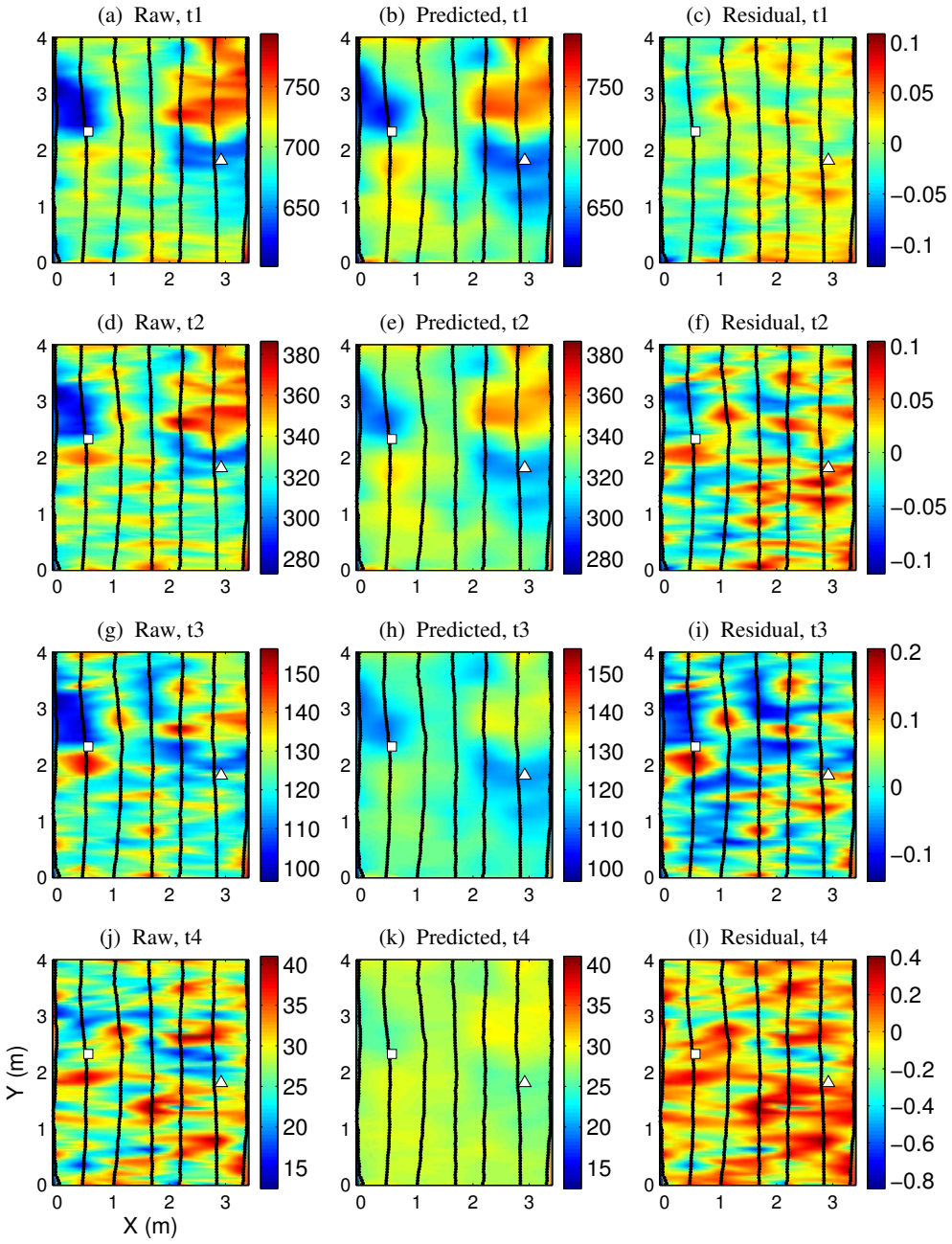

Figure 6.9: Comparison of 2ms chip raw data and the 2ms data predicted from the 10ms chip data. The bolt and UXO are not present for this data.

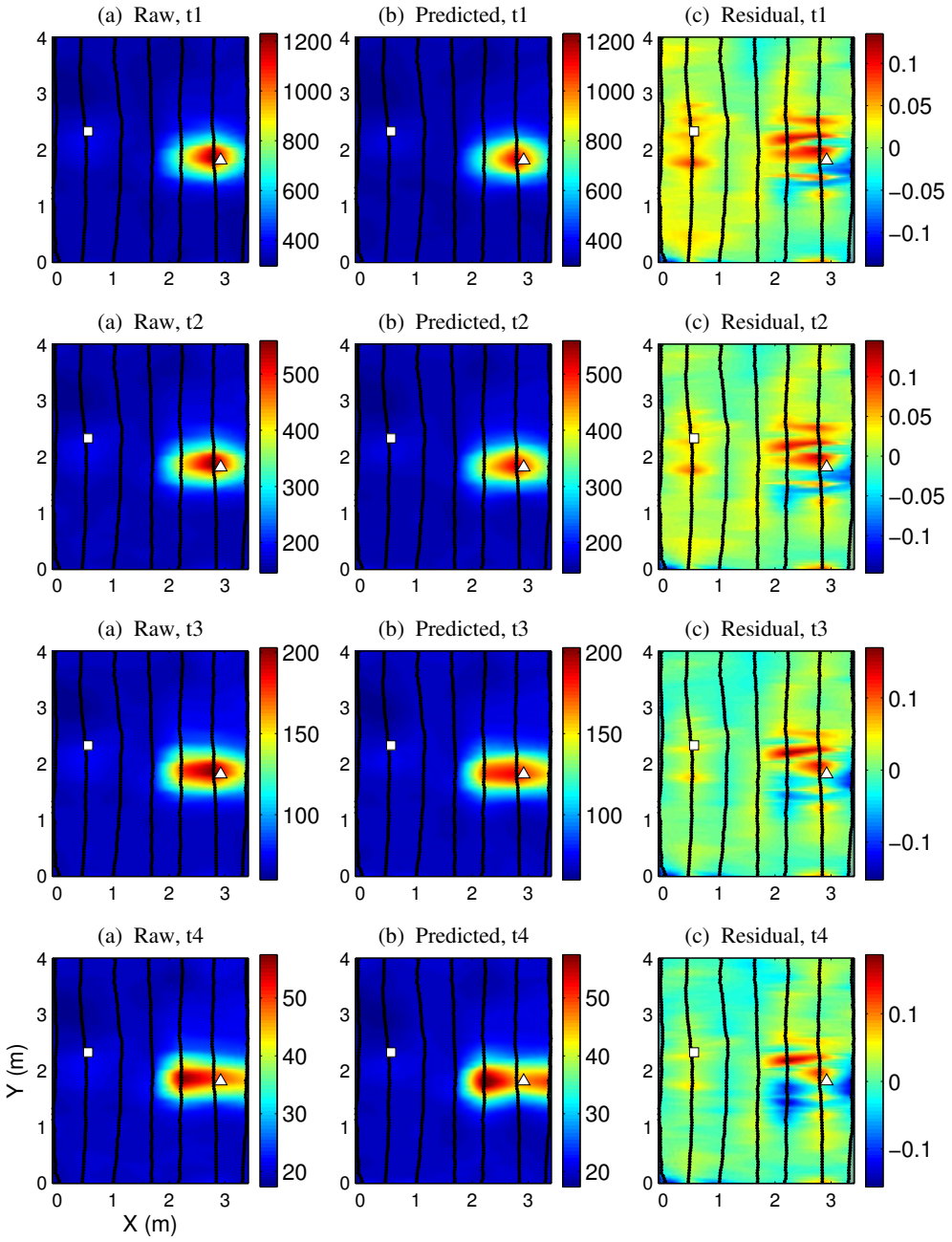

Figure 6.10: Comparison of 4ms chip raw data and the 4ms data predicted from the 10ms chip data. The bolt and UXO are present for this data.

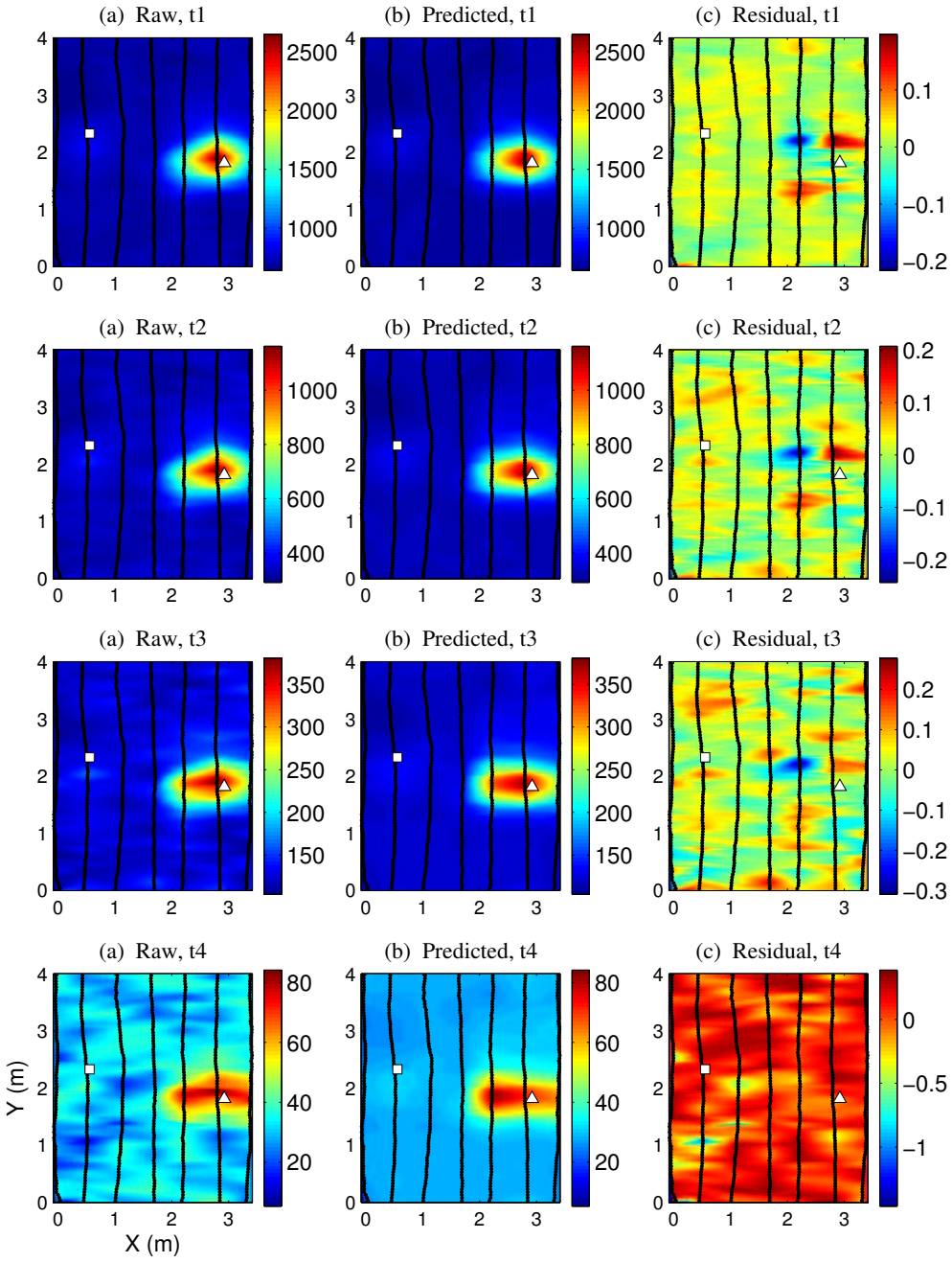

Figure 6.11: Comparison of 2ms chip raw data and the 2ms data predicted from the 10ms chip data. The bolt and UXO are present for this data.

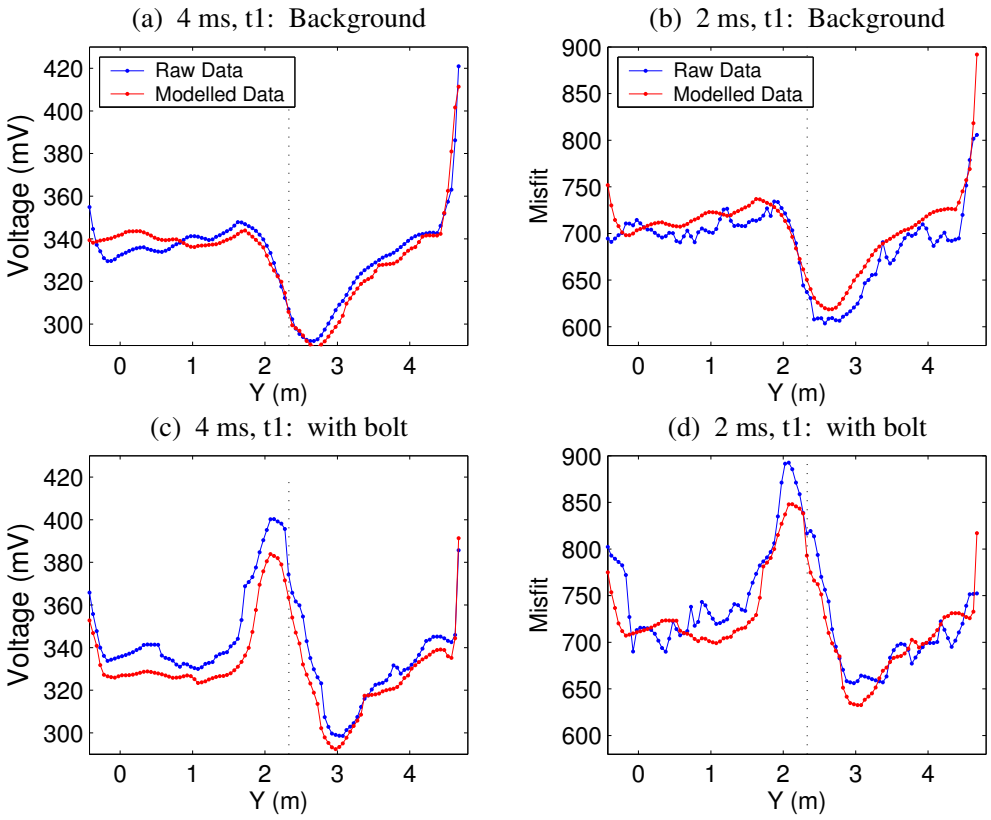

Figure 6.12: Comparison of 4ms chip raw data and the 4ms data predicted from the 10ms chip data. The bolt and UXO are not present for this data.

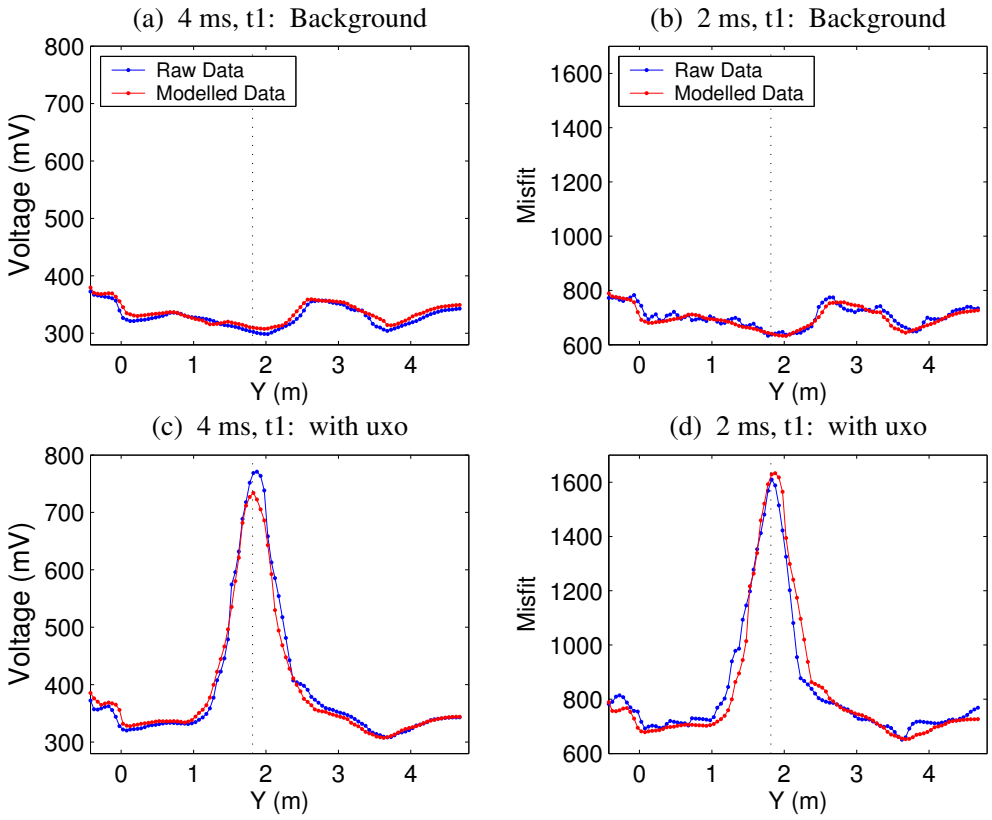

Figure 6.13: Comparison of 4ms chip raw data and the 4ms data predicted from the 10ms chip data. The bolt and UXO are present for this data.

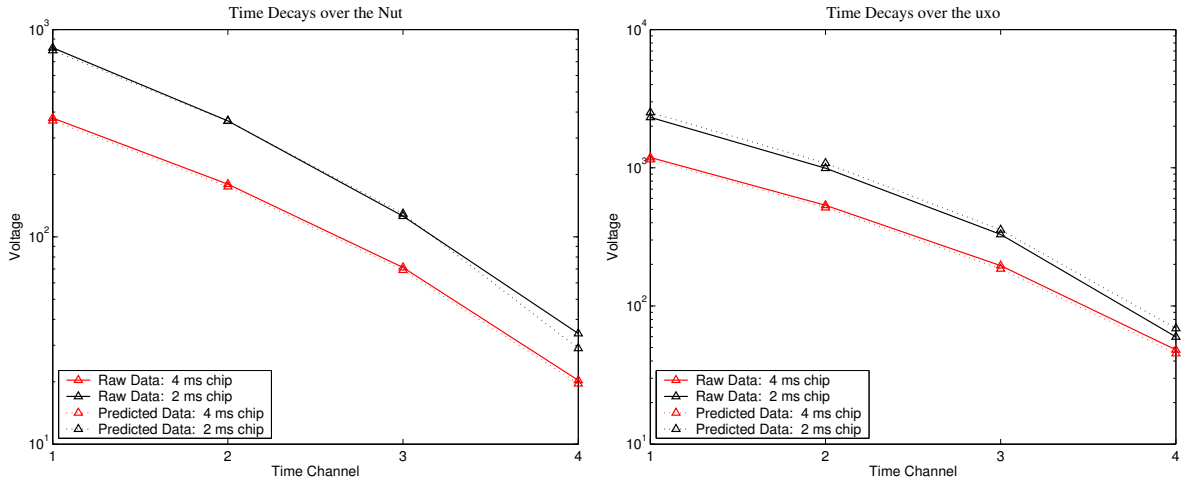

(a) Soil decay at the nut location

(b) Soil decay at the 90 mm location

Figure 6.14: Decay comparisons.

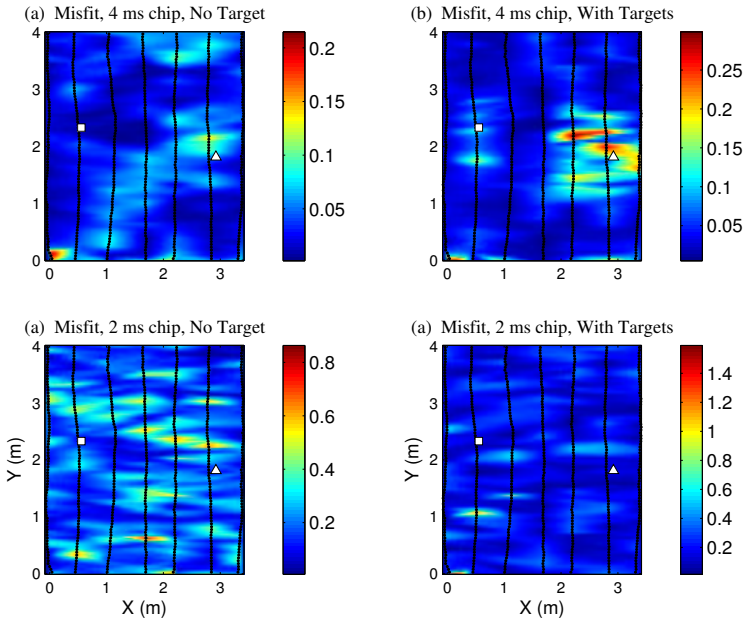

Figure 6.15: Comparison of misfits when applying the differential.

6.3.4 Waimea Geophysical Proveout at the Former Waikaloa Maneuver Area

Modified EM61MK2 data were collected at the Waimea GPO. The site has a much smaller background magnetic geologic response than Kaho'olawe. Figure 6.16 compares decays measured on the Waimea GPO, with a decay measured in the area of the Navy QA with the highest background magnetic response and with a decay measured in the areas with the lowest response.

The small wavelength data anomalies and noise due to sensor orientation and position changes will be smaller in magnitude compared to Kaho'olawe.

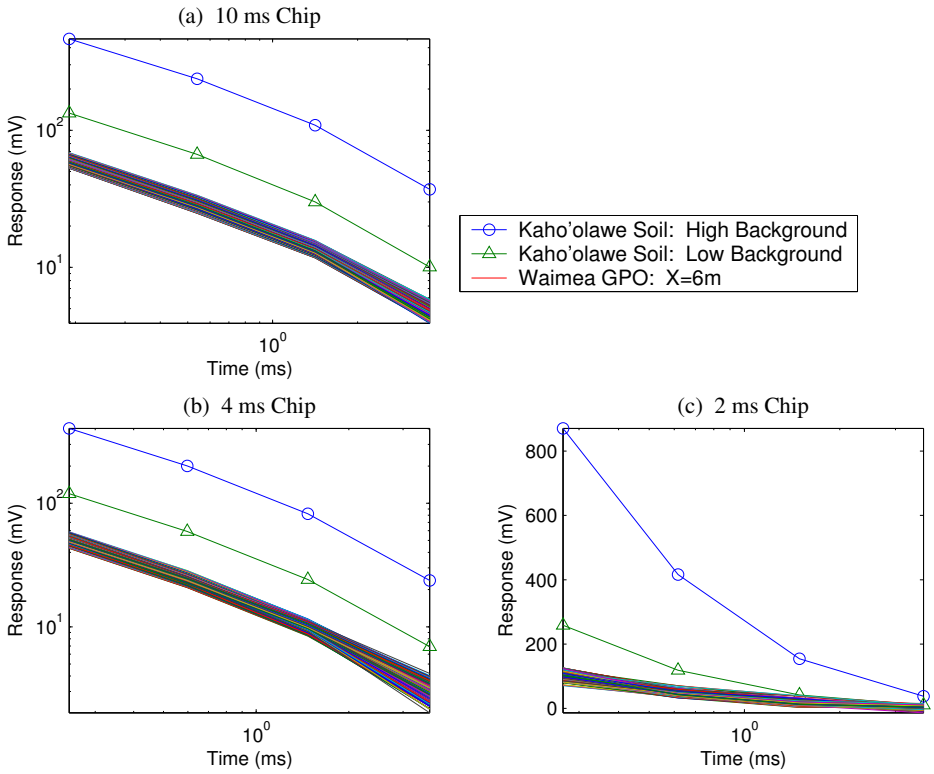

Figure 6.16: Comparison of background soil signal strengths at Kaho'olawe and Waimea.

We will focus on modified EM61MK2 data collected on a 30 x 6.5m section of the Waimea GPO. Within this area there are 18 emplaced UXO targets. Data for the 10, 4, and 2ms chips are plotted in Figures 6.17 through 6.19.

Unlike the Kaho'olawe plank data, the Waimea data were collected on a large enough survey area such that we can apply a 2D median filter to remove the long wavelength background signal. Figure 6.20 demonstrates the effect of a median filter with a 5m square window on the first time channel of the 10ms chip data.

The middle panel contains the median values which show that the background response ranges from 52 to 70mV in the first time channel of the 10ms chip data (compared to greater than 300mV measured on Kaho'olawe). The detrended data for each of the chips are plotted in Figures 6.21 through 6.23; Once data above the noise are identified, the usual course of action is to use a target picking algorithm to determine the presence of anomalies. The selected anomalies can then be inverted for model parameters to determine the identification of the target. For this example, we proceed in the same manner as the Kaho'olawe plank data and compare the data above the noise to a soil model (Figures 6.27 through 6.29). By plotting the misfit to a soil model nearly all the non-UXO related anomalies have been eliminated. The misfit calculated from the

10ms chip was able to produce a misfit at all but three of the UXO. Due to noise, the processed 2ms chip data was not as effective in detecting the emplaced targets.

Let us label the left row of targets 1 through 9, with label numbers increasing with y. If we look at the four emplaced targets at the top of the row, we notice that targets 6, 7, and 8 produce distinct anomalies in the detrended data, while target 9 produces a very weak anomaly. When proceeding with the soil fitting analysis and grid the misfit, target 9 does not produce an anomaly and target 6 produces a weak, incoherent response. To see why this is let us look at the soundings over targets 6 through 9 (Figure 6.30. The soundings measured by both the 10ms and 4ms chips indicate that the decay of targets 7 and 8 is slower than the background soil response, and therefore produces a significant misfit to the soil model. Target 9 does not produce an appreciable misfit since its response is nearly identical to the background when measured by the 10ms chip, and the response is in the noise of the data when measured by the 4ms chip. Target 6, which had an appreciable anomaly in the detrended data, has only a weak anomaly in the soil misfit map because its decay nearly matches the decay of the soil. If we decided to reduce the number of picks in the detrended data set by selecting targets based on the misfit map we would possibly have omitted target 6, which would have produced a false negative result.

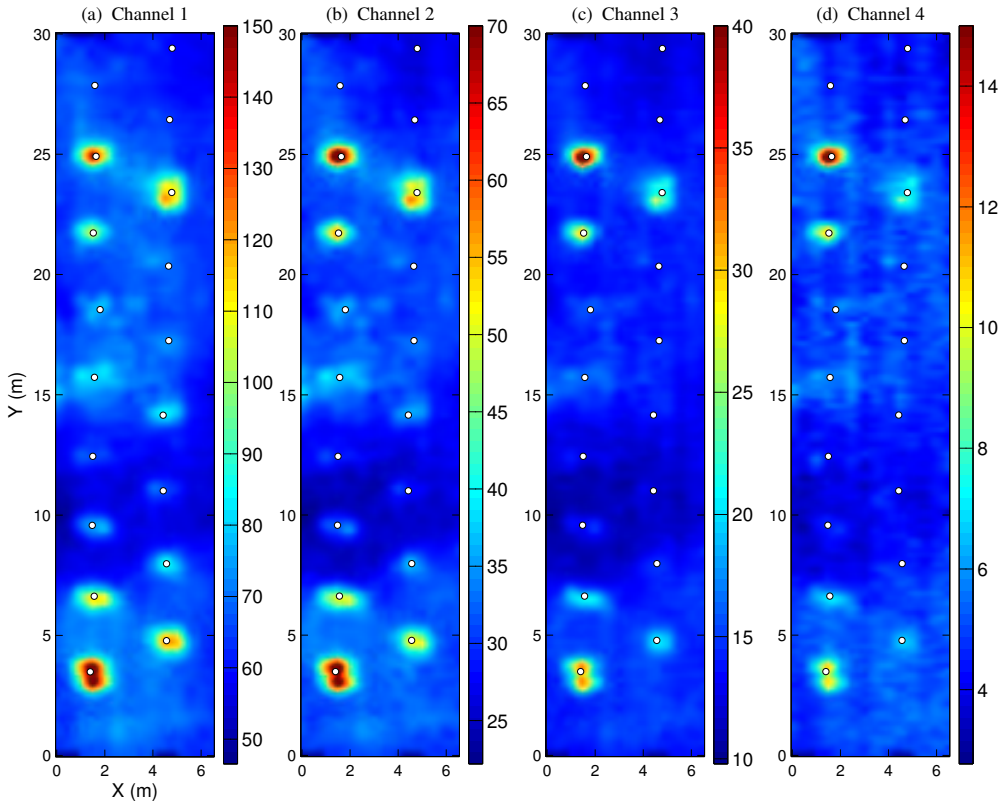

Figure 6.17: Waimea raw data 10ms. White circles indicate emplaced items.

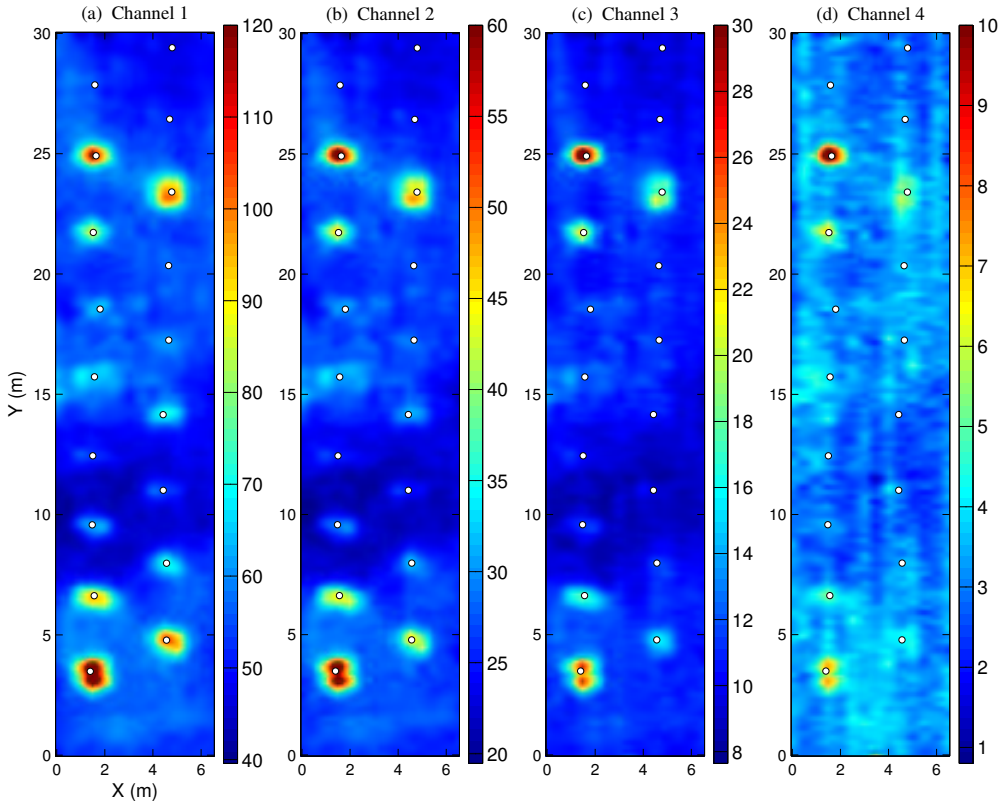

Figure 6.18: Waimea raw data 4ms. White circles indicate emplaced items.

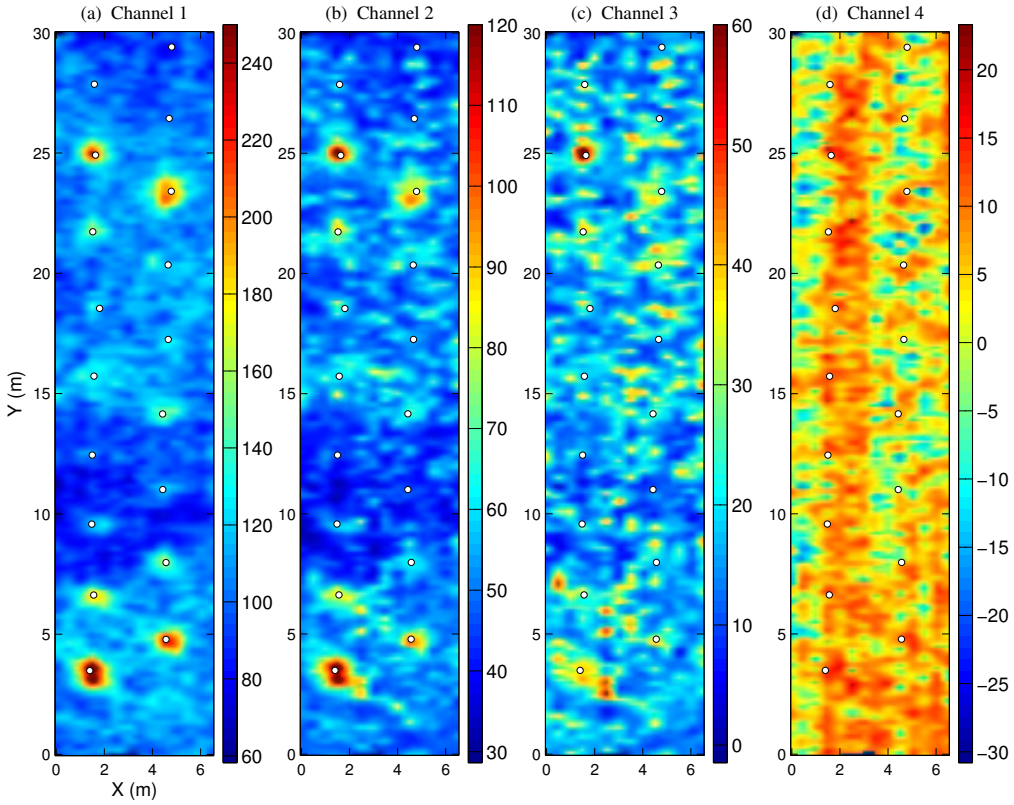

Figure 6.19: Waimea raw data 2ms. White circles indicate emplaced items.

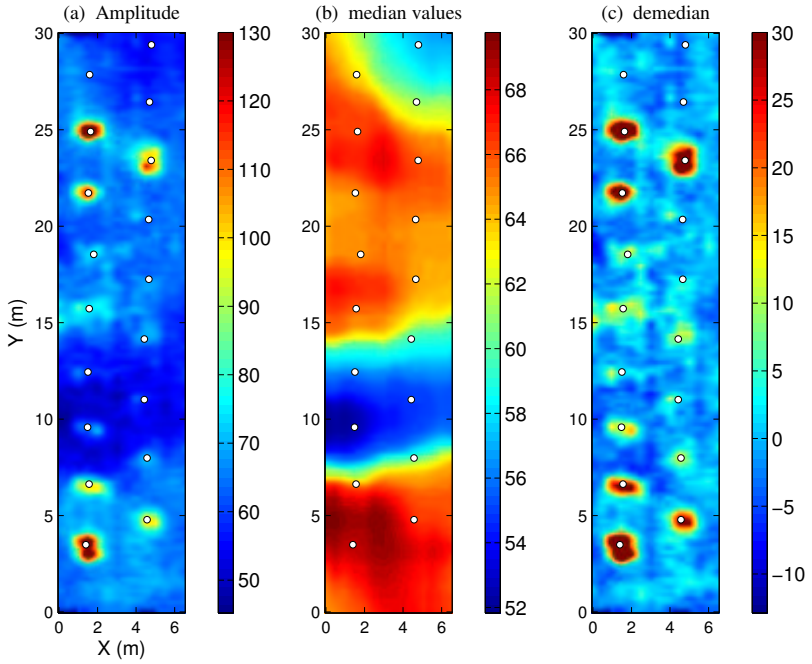

Figure 6.20: Waimea detrending example on the 10ms chip data.

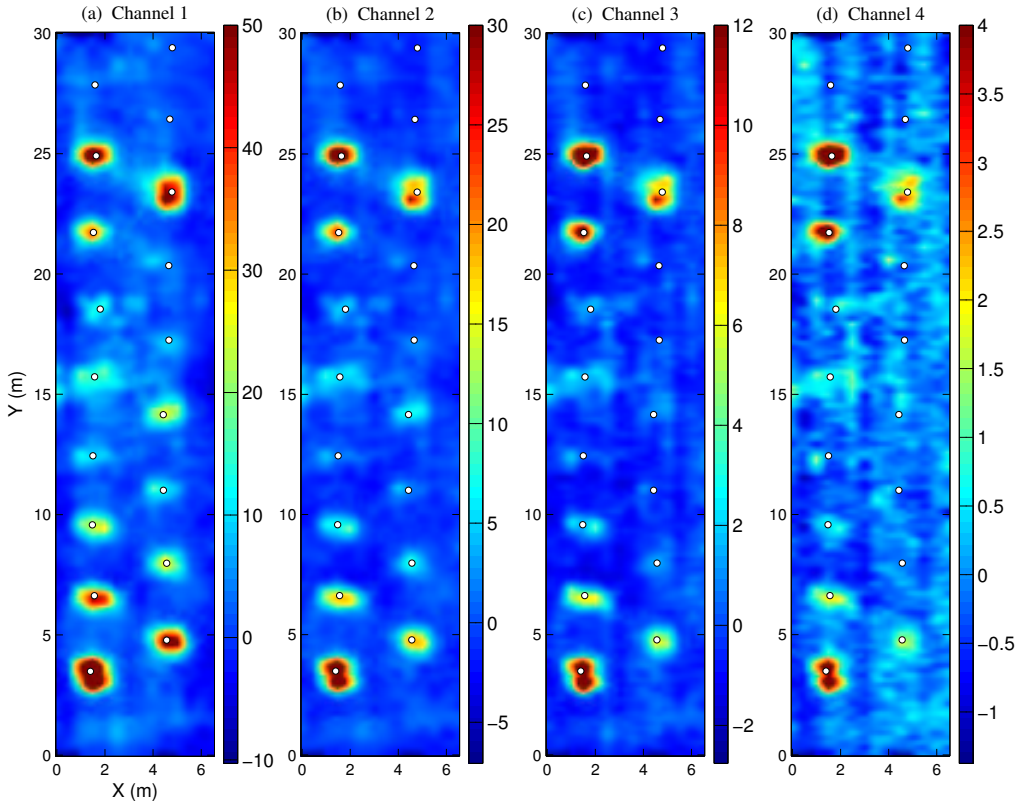

Figure 6.21: Detrended Waimea, 10ms.

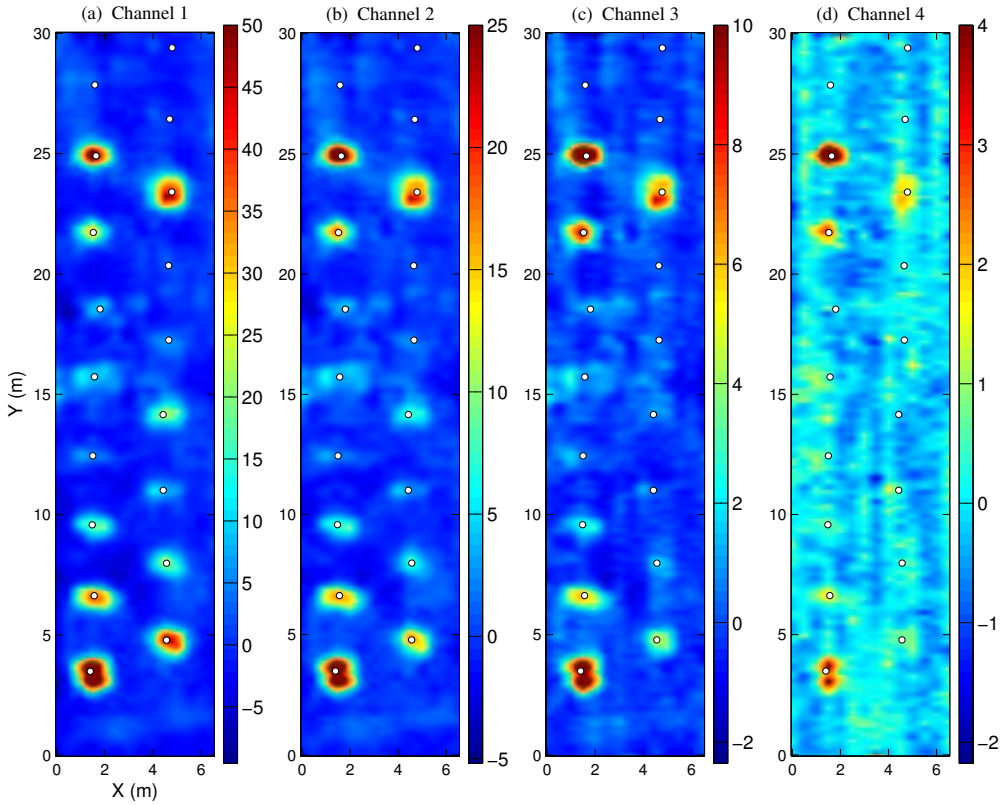

Figure 6.22: Detrended Waimea data 4ms.

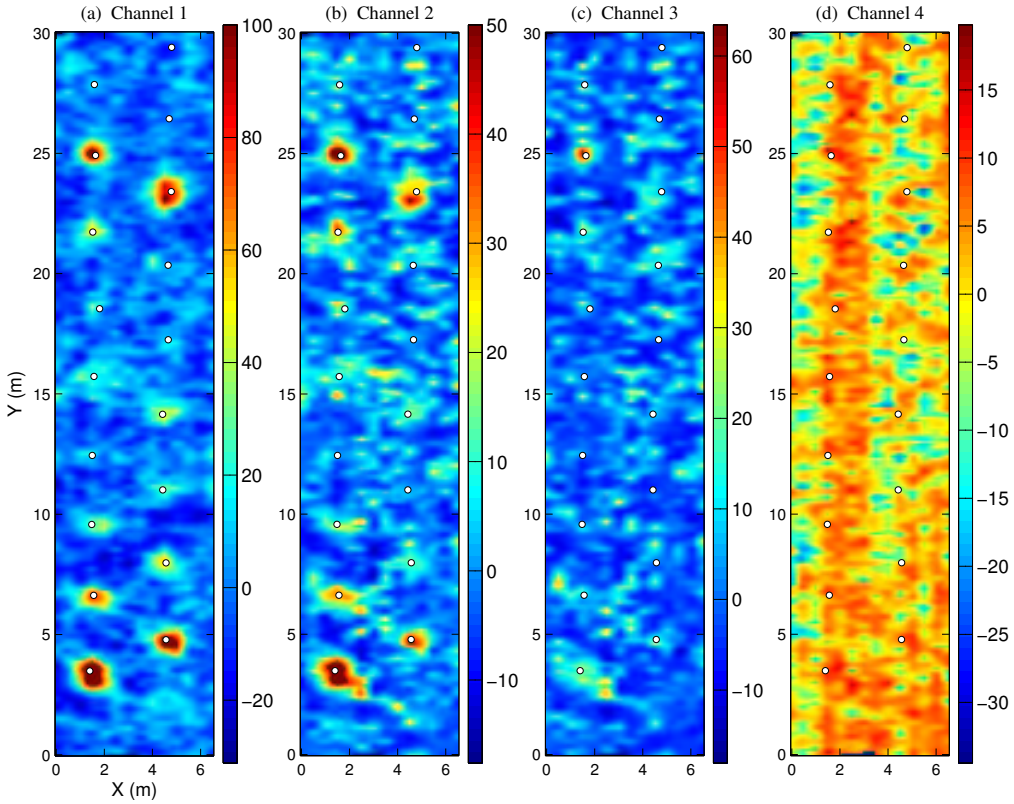

Figure 6.23: Detrended Waimea data 2ms.

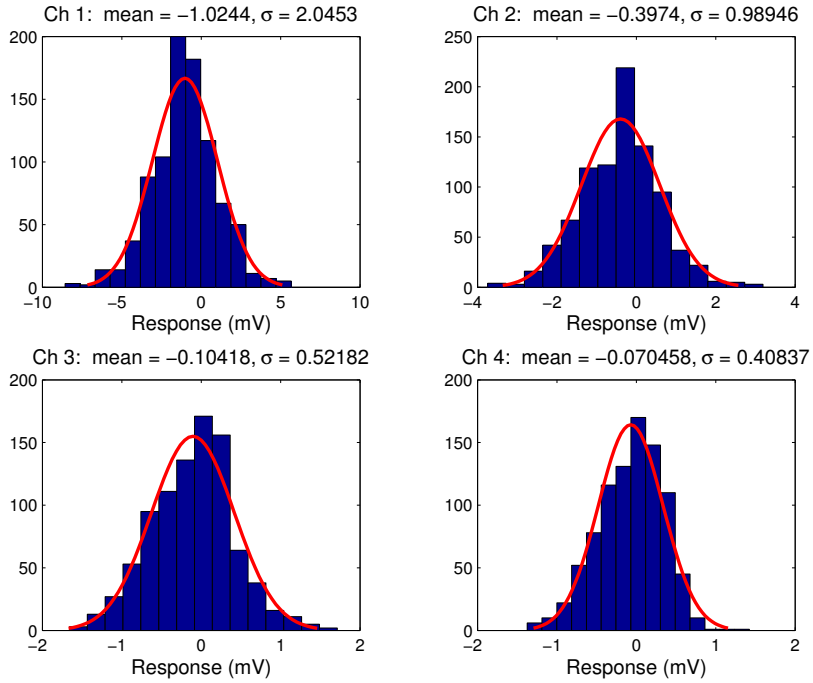

Figure 6.24: Waimea Soil Histogram data 10ms.

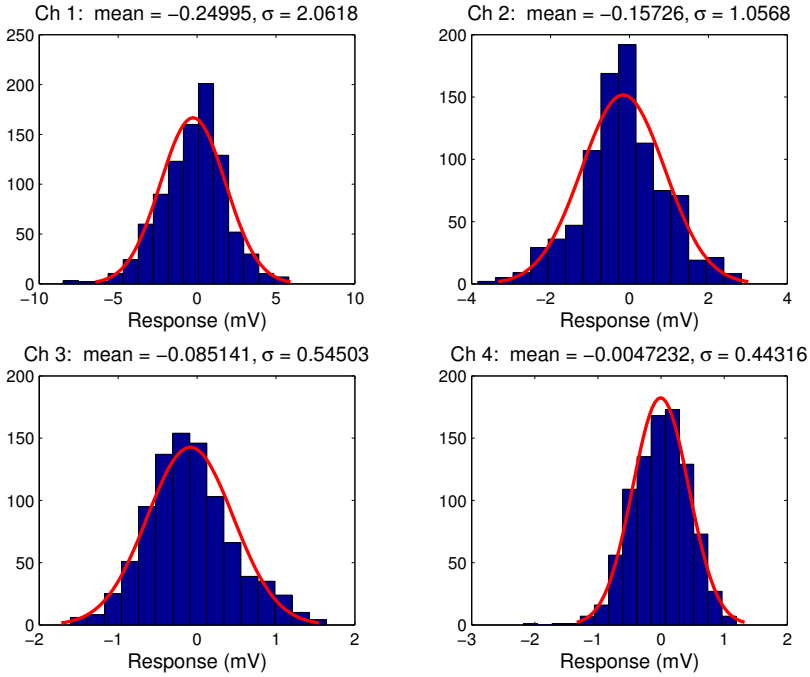

Figure 6.25: Waimea Soil Histogram data 10ms.

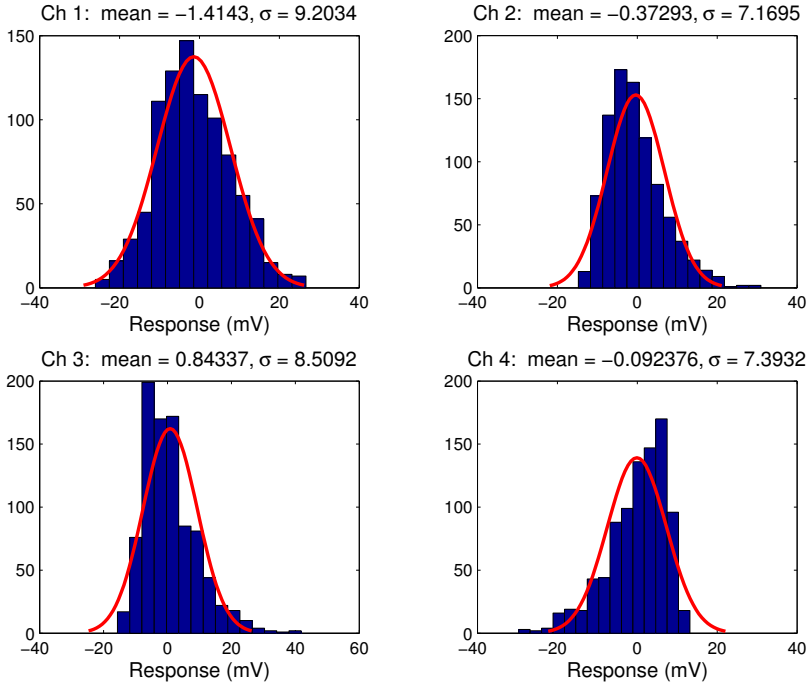

Figure 6.26: Waimea Soil Histogram data 10ms.

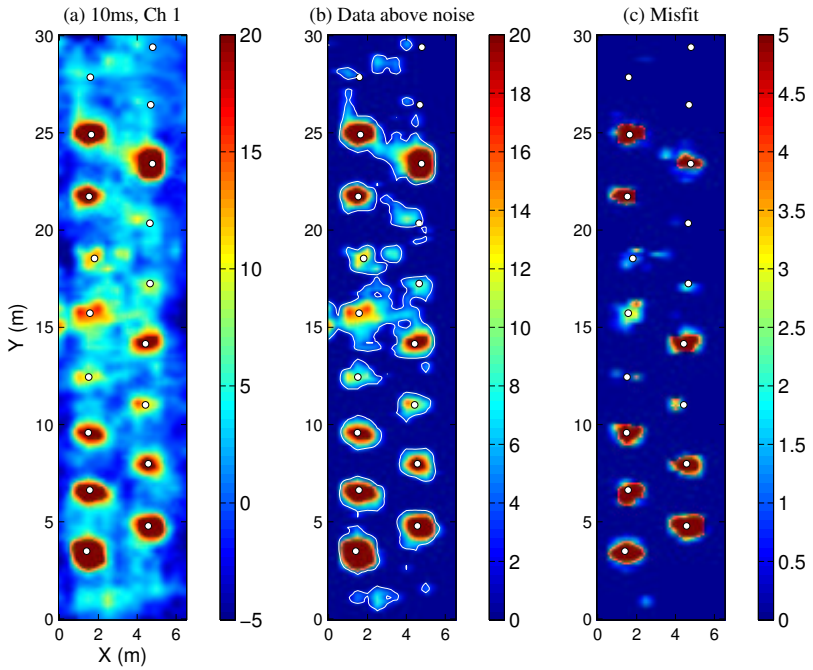

Figure 6.27: (a) Raw 10ms chip data for the first time channel. (b) Data greater than twice the standard deviation of the background noise. (c) The soil misfit calculated for the data above the background noise.

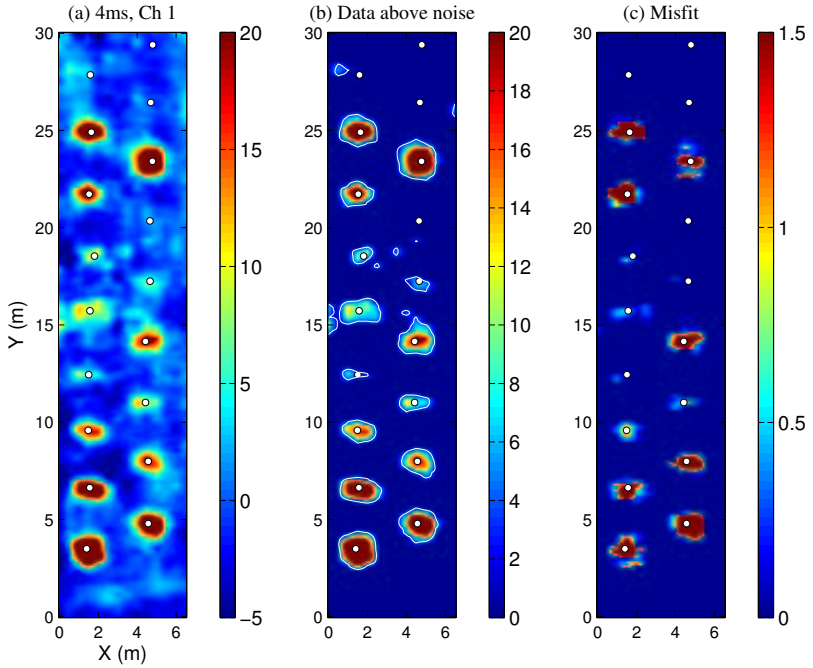

Figure 6.28: (b) Raw 4ms chip data for the first time channel. (b) Data greater than twice the standard deviation of the background noise. (c) The soil misfit calculated for the data above the background noise.

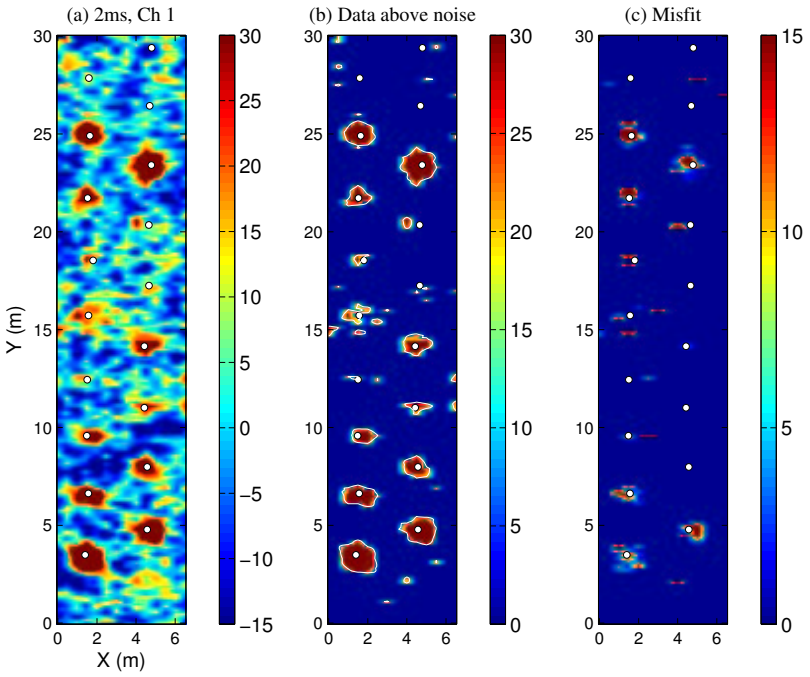

Figure 6.29: (a) Raw 2ms chip data for the first time channel. (b) Data greater than twice the standard deviation of the background noise. (c) The soil misfit calculated for the data above the background noise.

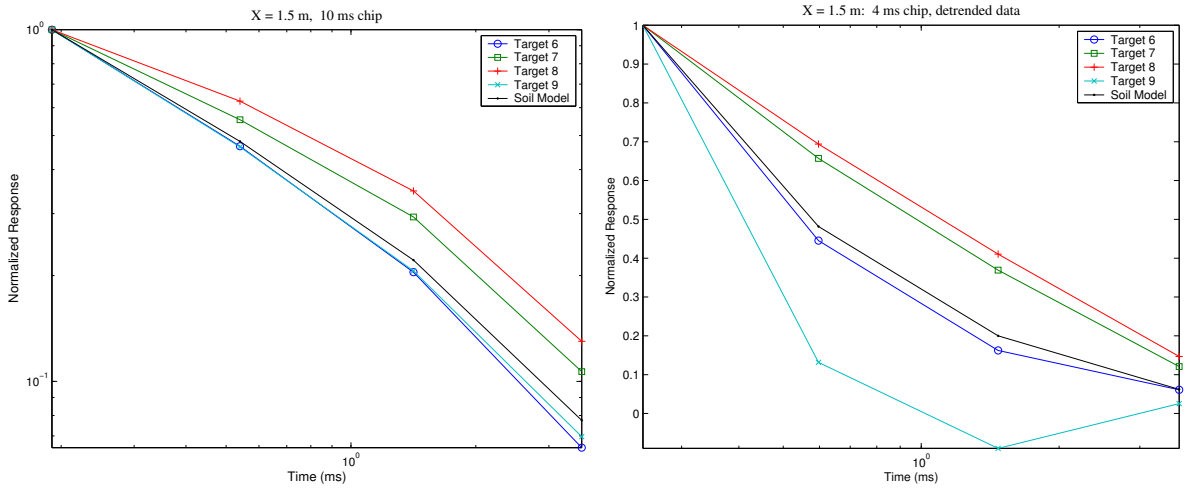

(a) Soil decay for the 10ms chip

(b) Soil decay for the 4ms chip

Figure 6.30: Decay comparisons.

6.4 Conclusion

In this chapter, we presented analysis of multi-waveform TEM data. Modelling was used to determine how a measured decay curve is altered by changing the length of the transmitter on-time. As expected, we saw that the response of targets with time constants less than transmitter on-times are less sensitive to the length of the on-time than targets with larger time constants. We showed that the time constants of typical UXO targets would need to be large to have a differential effect when measuring data from different waveforms. The lack of a differential effect was evident when analysing the field data from Kaho'olawe and the Waimea GPO on the Waikaloa Maneuver Area. When soil model fitting was applied to the data, the inability of the soil model to fit the observed data proved to be a good indicator of the presence of metal. However, we saw instances where the target response was close to the background response. In such a case, false negatives may occur when using the soil misfit as a means of detection.

Chapter 7

Discussion and conclusions

This study was motivated by the significant problems caused by VRM soils during the munitions response on Kaho'olawe Island. These soils caused almost 30% of the anomalies that were excavated as potential UXO. In field-trials the soil appeared to defeat whatever advanced technologies were brought to bear. Our concept was that the VRM soil problem could only be attacked by clever use of differential measurements. That is, measurements that excite a different response in the soil compared to metallic items. We considered four types of differential measurement:

1. Receiver height: Intended to exploit the different fall-off of the soil response compared to that of a compact metallic object;

2. Transmitter field direction: The horizontal field of a vertical dipole transmitter is null-coupled to a soil with laterally homogeneous soil properties. Thus the soil should exhibit a weak to non-existent horizontal field, in contrast to a compact metallic object;

3. Transmitter loop size: Original concept used to motivate this study, but subsequently we discovered that the soil and metallic responses scale in the same way with loop-size; and

4. Transmitter waveform: Intended to exploit different responses in metal targets compared to soil through varying the charge-up time.

The first two differential measurements listed above assume that the soil can be approximated by a homogeneous half-space. At the site we visited on Kaho'olawe Island, there were significant variations in the concentration of magnetic materials over very short length scales. In addition, micro-topography caused large amplitude, short wavelength anomalies in the EMI data, due both to changing sensor-ground geometry and variations in sensor orientation. Thus, the soil response would not be well modeled by a half-space and we infer that the first two differential measurements listed above would have met with little success.

We postulate that micro-topography could have been the cause of a large number of the 30% of anomalies excavated on Kaho'olawe that were attributed to geology.

We chose to concentrate on differential measurements based on variations in transmitter waveform. The main reason for this was that the TEM response of a soil is dominated by the VRM (and generally not the soil conductivity) and that the form of the TEM decay from VRM material is independent of its spatial distribution. Thus, while the amplitude will change with micro-topography, coil orientation and lateral distribution of VRM, the form of the TEM decay is invariant. This makes any technique based on this phenomenon attractive from a practical point of view.

Early on in the report, we considered soil compensation methods that involved estimating the soil response from a single transmitter waveform. These types of methods can work quite well, but there is

always the possibility that a UXO will fit the soil model, and hence not be flagged for excavation. We presented such an example from Kaho'olawe involving a 5" HE round. This provided strong incentive to develop a differential measurement methodology.

On Kaho'olawe Island and at the Waikoloa Manoeuver Area, we conducted field studies to evaluate the effectiveness of differential measurements based on varying transmitter charge times. EM-61MKII measurements with three different transmitter on-times of 10ms, 4ms and 2ms were collected. Our analysis showed that for typical UXO targets, differential measurements based on these varying charge times were no more effective at suppressing the soil response than soil compensation methods based on a single charge time. The reason for this is that the time-constants of most UXO are long compared to the latest time-channel measured by the EM-61. This means that both soil and metallic objects exhibit similar differential responses. If the time constants of UXO were significantly smaller than the latest time channel, these differential measurements would have excited a different response compared to the soil (Figure 6.1 illustrates the point).

The differential technique based on varying the charge time would only work for typical UXO if the measurement range extended past the object's characteristic time-constant. A 5cm diameter steel sphere, as a point of comparison, has a time constant of 40ms. This would represent a UXO like-object of the small to medium range. Larger UXO would have even larger time constants (the particular time constant excited depends on the UXO orientation). 40ms represents a long time after pulse-shutoff; for example, the EM-61 measures out to around 3.5ms, while the EM-63 extends that range to 25ms. Thus existing commercial sensors stop measuring a long-time before the differential effect would likely be observed. In addition, even if the sensors did measure that far in time, the signal-to-noise ratio would be quite small. Thus it appears that differential measurements based on variable charge time are unlikely to improve UXO detection performance in magnetic soils.

While the differential measurements trialed in this SEED did not result in an appreciable improvement in soil compensation techniques, the study did considerably improve the UXO community's understanding of magnetic soils. Prior to this study, some preliminary work on the importance of the frequency dependance of susceptibility (i.e. VRM) on the soil response had been conducted (Pasion et al., 2002a). During this study we obtained a good understanding of the physical mechanisms that control the effect of soil on a metal detector. In particular, we now have the ability to predict the soil response from an arbitrary transmitter waveform. These predictions depend on our assumed model of magnetic viscosity, i.e. that it is caused by magnetic domains with a log-uniform distribution of time-constants. Several studies (such as SERDP-1414) are currently ongoing that involve the development of instrumentation to measure the susceptibility at multiple frequencies. This will confirm the assumption that soils can be modelled with a log-uniform distribution.

We feel that there are two promising avenues to pursue as extensions to the work presented here.

1. Make detection decisions based on the anomaly amplitude (as in surveys in non-magnetic soil) and then conduct a physics based inversion. The spatial characteristics of the soil response will likely not fit a dipolar model very well. In addition, the form of the decay of the soil anomaly will be invariant to the position of the EM-sensor. In contrast, the decay characteristics of a metallic object (except a sphere) will vary with the location of the sensor, as the transverse and axial modes of the target are stimulated to varying degrees;

2. As we discussed in Chapter 3 a differential measurement of great promise would involve varying the direction of the primary field (and/or measuring different components of the secondary field). The motivation for this method is similar to the principal of the preceding method; i.e. the form of the soil response will be invariant to the direction of the primary field (in direct contrast to metallic objects). Several instruments with these characteristics are currently under development and could potentially perform quite well in hostile soil environments, if the data are processed in an intelligent manner.

Bibliography

Billings, S., Pasion, L., Oldenburg, D. and Foley, J.: 2003, The influence of magnetic viscosity on electromagnetic sensors, *Proceedings of EUDEM-SCOT2, International Conference on Requirements and Technologies for the Detection, Removal and Neutralization of Landmines and UXO*.

Buselli, G.: 1982, The effect of near surface superparamagnetic material on electromagnetic measurements, *Geophysics* **47**, 1315–1324.

Candy, B.: 1996, Pulse induction time domain metal detector, United States Patent Office. Num. 5576624.

Cargile, D., Bennett, H., Goodson, R., DeMoss, T. and Cespedes, E.: 2004a, Advanced UXO Detection/Discrimination Technology Demonstration - Kaho'olawe, Hawaii, *Technical report*, U.S. Army Research and Development Center, Vicksburg, MS. ERDC/EL TR-04-1.

Cargile, D., Bennett, H. H., Goodson, R. A., DeMoss, T. A. and Cespedes, E. R.: 2004b, Advanced UXO detection/discrimination technology demonstration, Kahoolawe, Hawaii, *Technical Report ERDC/EL TR-04-1*, U.S. Army Engineer Research and Development Center.

Cespedes, E. R., Cargile, D., Bennett, H., Berry, T., Goodson, R., Dihn, H., Steward, S. and Robitaille, G. E.: 2001, Demonstration of advanced UXO detection and discrimination technologies at Kaho'olawe, Hawaii, *Proceedings of Partners in Environmental Technology Techinical Symposium and Workshop, Washington, D.C.*

Colani, C. and Aitken, M. J.: 1996, Utilization of magnetic viscosity effects in soils for archaeological prospection, *Geophysics* **212**, 1446–1447.

Dabas, M., Jolivet, A. and Tabbagh, A.: 1992, Magnetic susceptibility and viscosity of soils in a weak time varying field, *Geophys. J. Int.* **108**, 101–109.

Fannin, P. C. and Charles, S. W.: 1995, On the influence of distribution functions on the after-effect function of ferrofluids, *Journal of Physics D* **28**, 239–242.

Kaufman, A. A.: 1994, *Geophysical Field Theory and Method*, Academic Press.

Nabighian, M. N.: 1979, Quasi-static transient response of a conducting half-space - An approximate representation, *Geophysics* **44**(10), 1700–1705.

Néel, L.: 1949, Théorie du trainage magnétique des ferromagnétiques en grains fins avec application aux terres cuites, *Ann. Geophys.* **5**, 99–136.

Newman, G. A., Hohmann, G. W. and Anderson, W. L.: 1986, Transient electromagnetic response of a three-dimensional body in a layered earth, *Geophysics* **51**(8), 1608–1627.

Parsons Engineering, U. I.: 1998, Cleanup Plan: UXO Clearance Project, Kaho'olawe Island Reserve, Hawaii, *Technical report*, Parsons Engineering, UXB International. Prepared for Naval Facillities Engineering Command Pacific Division.

Pasion, L., Billings, S. and Oldenburg, D.: 2002a, Evalating the Effects of Magnetic Susceptibility in UXO Discrimination Problems, *Proceedings from SAGEEP 02*.

Pasion, L. R., Billings, S. D. and Oldenburg, D. W.: 2002b, Evaluating the effects of magnetic soils on TEM measurements for UXO detection, *Proc. 2002 UXO Forum*, New Orleans, LA.

Pasion, L. R. and Oldenburg, D. W.: 2001, Locating and Characterizing Unexploded Ordnance Using Time Domain Electromagnetic Induction, *Technical report*, U.S. Army Research and Development Center, Vicksburg, MS. ERDC/GSL TR-01-10.

Pasion, L., Walker, S., Oldenburg, D., Billings, S. and Foley, J.: 2005, Evaluating the effectiveness of varying transmitter waveforms for UXO detection in magnetic soil environments, *Proceedings from SAGEEP 05*.

Putnam, J.: 2001, Kaho'olawe program management and technology, *Proceedings of the UXO/Countermine Forum*.

Stearns, H. T.: 1940, Geology of ground water resources on the islands of Lanai and Kaho'olawe, Hawaii, bulletin 6, *Technical report*, Department of the Interior, Washington, D. C.

Walker, S., Pasion, L., Billings, S., Oldenburg, D., Li, Y. and Foley, J.: 2005, Examples of the effect of magnetic soil environments on time domain electromagnetic data, *Proceedings from SAGEEP 05*.

Ward, S. H. and Hohmann, G. W.: 1987, Electromagnetic theory for geophysical applications, *in* M. N. Nabighian (ed.), *Electromagnetic Methods in Applied Geophysics: Volume 1 Theory*, The Society of Exploration Geophysicists.

Ware, G. H.: 2001, EM-63 decay curve analysis for ordnance discrimination, *Proceedings of Partners in Environmental Technology Techinical Symposium and Workshop, Washington, D.C.*